JULIUS-MAXIMILIANS-UNIVERSITÄT
WÜRZBURG

MASTERARBEIT

Development of an Electrochemical Testing Setup to Characterize RuO_2(110) Thin Films

Autor:
Christopher REISER

Betreuer:
Dr. Vedran JOVIC

eingereicht am

Lehrstuhl für Experimentelle Physik IV

der

Fakultät für Physik und Astronomie

April 2022

1. Gutachter: Dr. Simon MOSER

2. Gutachter: Prof. Dr. Matthias BODE

Abstract

The long-term goal of this project is to provide a causal link between the oxygen evolution reaction (OER) mechanism and the underlying physical phenomena rooted in the electronic structure of RuO_2(110). At first, RuO_2 is described in the context as highly-active industrial catalyst for various chemical reactions (section 1.1). As RuO_2 is moreover a benchmark catalyst for electrochemical water splitting and the production of hydrogen, the theoretical foundation of the oxygen evolution reaction (OER) is presented (section 1.2). After the required fundamental electrochemical concepts are discussed (chapter 2), a custom electrochemical cell is developed and its functionality is tested and characterized (chapter 3). The investigated samples originate from a successful prior pulsed laser deposition (PLD) growth program of oriented RuO_2(110) thin films on TiO_2(110) substrates. These samples are categorized into morphological groups by scanning electron microscopy (SEM) (section 4.1). A reliable reference value for the specific double-layer capacitance (DLC) of RuO_2(110) in 1 M H_2SO_4 electrolyte is determined to be $(34.6 \pm 0.9)\,\mu F\,cm^{-2}$ by electrochemical impedance spectroscopy (EIS), cyclic voltammetry (CV) and SEM – the specific capacitance of a near atomically-flat reference sample allows for the normalization of the measured current per electrochemically active surface area (ECSA) (section 4.3). A model for the main observed surface protonation reactions is proposed (subsection 4.5.9) utilizing a novel technique based on CV developed in this thesis (subsection 4.5.7). A reversible, time- and potential-dependent loss of OER activity is discovered, investigated and modeled (section 5.1). The findings are utilized to perform a Tafel analysis of the OER activity (subsection 5.4.2). In particular, a standardized electrochemical characterization protocol is developed, which allows for batch screening of various samples in combination with an automatized data evaluation script (section 5.2). It is applied to 12 available thin film samples and yields specific trends, which can be further correlated to the prior morphology determined by SEM (section 5.4). Finally, possible improvements to the protocol are discussed (section 5.5) and future pathways of this project are outlined (chapter 6). The goal of establishing a link to surface science is approached by the derivation of an atomic-site specific model of the potential-dependent surface terminations of RuO_2(110) (subsection 4.5.9).

Zusammenfassung

Langfristig ist das Ziel dieses Projekts einen kausalen Zusammenhang zwischen dem Mechanismus der Sauerstoffevolutionsreaktion (OER) und den zugrundeliegenden physikalischen Phänomenen, welche in der elektronischen Struktur der Oberfläche von RuO_2(110) verankert sind, zu schaffen. Zu Beginn wird RuO_2 im Kontext eines hochaktiven industriellen Katalysators für vielfältige chemische Reaktionen beschrieben (section 1.1). Da RuO_2 überdies noch ein mustergütiger Katalysator für die elektrochemische Wasserspaltung und Wasserstoffproduktion ist, werden die theoretischen Grundlagen der Sauerstoffevolutionsreaktion (OER) dargestellt (section 1.2). Nachdem die benötigten grundlegenden elektrochemischen Konzepte beschrieben wurden (chapter 2), wird ein speziell angefertigte elektrochemische Messzelle entwickelt und ihre Funktionalität geprüft und charakterisiert (chapter 3). Die untersuchten Proben stammen von einem vorherigen erfolgreichen, auf gepulster Laserdeposition (PLD) basierenden, Wachstumsprogramm von orientierten RuO_2(110) Dünnschichten auf TiO_2(110) Substraten. Diese Proben werden nach ihrer Morphologie gruppiert mithilfe von Rasterelektronenmikroskopie (SEM) (section 4.1). Ein verlässlicher Referenzwert für die spezifische Doppelschichtkapazität von RuO_2(110) in 1 M H_2SO_4 Elektrolyten wird bestimmt zu $(34.6 \pm 0.9)\,\mu F\,cm^{-2}$ durch elektrochemische Impedanzspektroskopie (EIS) und zyklische Voltammetrie (CV) und SEM – die spezifische Kapazität einer annähernd atomar flachen Referenzprobe erlaubt die Normalisierung des gemessenen Stroms auf die elektrochemisch aktive Fläche (ECSA) (section 4.3). Ein Modell für die wichtigsten beobachteten Oberflächenprotonierungsreaktionen wird vorgeschlagen (subsection 4.5.9) unter Benutzung einer neuartigen, auf zyklischer Voltammetrie (CV) basierenden Technik, welche in dieser Arbeit entwickelt wurde (subsection 4.5.7). Ein umkehrbarer, zeit- und potentialabhängiger Verlust der Sauerstoffevolutionsreaktionsaktivität wird entdeckt, untersucht und mathematisch beschrieben (section 5.1). Die Entdeckung wird genutzt, um eine Tafel-Analyse der Sauerstoffevolutionsreaktionsaktivität durchzuführen (subsection 5.4.2). Konkret wird ein standardisiertes elektrochemisches Charakterisierungsprotokoll entwickelt, welches eine Serien-Untersuchung verschiedener Proben mit einem dazugehörigen automatisierten Auswertungsskript ermöglicht (section 5.2). Es wird auf die 12 zur Verfügung stehenden Dünnschichtproben angewendet und zeigt deutliche Trends auf, welche sich wiederum zu der vorherigen, mittels Rasterelektronenmikroskopie (SEM) bestimmten, Morphologie korrelieren lassen (section 5.4). Letztlich werden mögliche Verbesserungen (section 5.5) des Protokolls diskutiert und zukünftige Richtungen des Projekts beschrieben (chapter 6). Eine Annäherung an das Ziel eine Verbindung zur Oberflächenphysik herzustellen, wird erreicht durch die Herleitung eines auf den atomaren Adsorptionsplatz spezifischen Modells der potenzialabhängigen Oberflächenterminationen von RuO_2(110) (subsection 4.5.9).

Contents

1 Ruthenium Oxide: Rising Fundamental Interest in an Industrial Catalyst

This chapter first motivates the industrial relevance of RuO_2-based catalysts and what their direct impact of the current research could be. The focus will then shift toward single crystalline model systems and how they are utilized to demonstrate a possible interrelation of electronic structure and catalytic surface reactions. In the second half, the framework of transition state theory (TST) is introduced. It connects the oxygen evolution reaction (OER) – a half reaction of electrocatalytic water splitting – to microscopic surface properties of RuO_2(110).

1.1 Role of RuO_2 in catalysis and physics

Ruthenium oxides have long been known for their superior catalytic properties.[1] Examples from the field of heterogeneous catalysis, in particular, include CO, NH_3 and HCl gas phase oxidation. The latter - also known as the Deacon process - offers a possibility to recycle the tremendous amounts of HCl produced by the chemical industry. Although this process has been known for more than 100 years, it is still less efficient than its electrolysis counterpart.[2] It now appears that RuO_2 coated rutile TiO_2 – the material of interest in this thesis – could initiate a tipping point, since it shows unprecedented gas phase HCl oxidation efficiency.[3]

Currently, the most important industrial application of ruthenium oxide is unequivocally the chlor-alkali electrolysis process. It generates chlorine and hydrogen gas as well as aqueous sodium hydroxide from brine.[2] The anode material of the chlor-alkali process is commonly referred to as a *Dimensionally Stable Anode*, which consists of a $Ru_{0.3}Ti_{0.7}O_2$ coated Ti metal plate or mesh.[4] To put this into perspective: In 2021, the ruthenium demand of the electrochemical industry has been 4.3 t, thus amounting to a considerable 13 % of the total annual need.[5]

This, by far, not exhaustive list of applications in catalysis and electrocatalysis already illustrates that ruthenium oxide is a jack-of-all-trades. With a focus on fulfilling the worlds future needs for sustainable energy production and storage, the water-splitting capability of RuO_2 regains importance. It centers on a promising technology possibly living on the edge of large scale application: The proton exchange membrane (PEM) electrolyzer is currently experiencing increased research and development attention with several running demonstration systems currently in operation. It represents one approach to utilize electrochemical water splitting for green hydrogen production for future sustainable energy storage applications.[6] Furthermore some PEM-electrolyzers offer the possibility to reverse the process and regain energy from ambient

air oxygen and hydrogen in terms of a fuel-cell operation mode.[7]

The overall water splitting reaction can be separated into the oxygen evolution reaction (OER) happening at the positively biased anode and the hydrogen evolution reaction (HER) at the negatively biased cathode as follows:

$$\text{HER (cathode)}: \quad 2\,H^+_{(aq)} + 2\,e^- \longrightarrow H_{2(g)} \tag{1}$$

$$\text{OER (anode)}: \quad 2\,H_2O_{(l)} \longrightarrow O_{2(g)} + 4\,H^+_{(aq)} + 4\,e^-. \tag{2}$$

In Eq. 1 hydrogen $H^+_{(aq)}$ is the oxidized species, which is reduced to yield $H_{2(g)}$. In the case of a PEM-electrolyzer, the two gas evolving compartments are separated by a gas tight membrane that offers proton conductivity, hence the name. This operating principle is depicted in Fig. 1a). In contrast to alkaline electrolyzers, PEM-electrolyzers rely on an acidic environment.[6] The electrochemical standard potential of water splitting is $E^\circ = 1.23\,V_{SHE}$[8]. The standard potential is reported versus the standardized reference potential of the standard hydrogen electrode (SHE), which is defined at $E^\circ = 0\,V_{SHE}$ (subsection 2.2.1). One can think of the water-splitting standard potential as the minimum theoretical electrical energy needed to split a water molecule. More precisely, this corresponds to leveling the Gibbs free energies of reactant and products of the overall reaction: $2\,H_2O_{(l)} \longrightarrow O_{2(g)} + 2\,H_{2(g)}$. Furthermore, it is assumed that a thermodynamic heat reservoir compensates for the endothermic nature of the water-splitting reaction.

In reality, one needs a surface to catalyze the complicated OER – there are four rection steps each including the transfer of a proton and an electron – as well as the more facile to catalyze HER.[9] The catalytic surface provides adsorption sites that aid to overcome the energy barriers of chemical bond formation and rupture. Active OER-catalysts that are stable under acidic conditions are RuO_2 and IrO_2, whereas the latter one tends to be more corrosion resistant, but, less active.[10] The HER is usually catalyzed by modified Pt cathodes.[6] The HER and OER half reaction of the overall water-splitting process illustrate the opportunity to directly impact the overall efficiency of the PEM electrolyzer by either optimizing the catalytic activity and utility of the anode or cathode (Fig. 1a)). As the more facile and less energy intense HER is readily catalyzed by Pt-based materials, the natural choice is to focus on the RuO_2-anode. The goal is to make use of fundamental insights about the OER to eventually track down key material properties which have to be tuned to reach even higher activity and stability.

The use of RuO_2-based materials for chlor-alkali electrolysis and PEM electrolyzers demonstrates their competitive performance in the chlorine evolution reaction (CER) and the OER, respectively. In addition, RuO_2 catalyzes the HER (better than other metal oxides, but not as well as the benchmark HER catalyst Pt[11,1]), the oxygen reduction reaction (ORR)[12–14] and the chlorine reduction reaction (CRR)[15]. Last, hydrous ruthenium oxides are used to build supercapacitors due to their ability to store pseudocapacitive charge in form of adsorbed (subsection 2.4.2) or bulk incorporated hydrogen atoms (section 4.4).[16,17]

To achieve the goal of understanding the fundamentals of the OER and eventually improve the catalytic performance of an OER-catalyst single crystalline model system are required. Single crystalline model systems, which offer controlled surface properties are required the more fundamental the research efforts get, especially on the theory side. Recent studies compared the electrocatalytic properties of different RuO_2 single crystal faces. At first glance, they show similar properties, nevertheless, there are certain

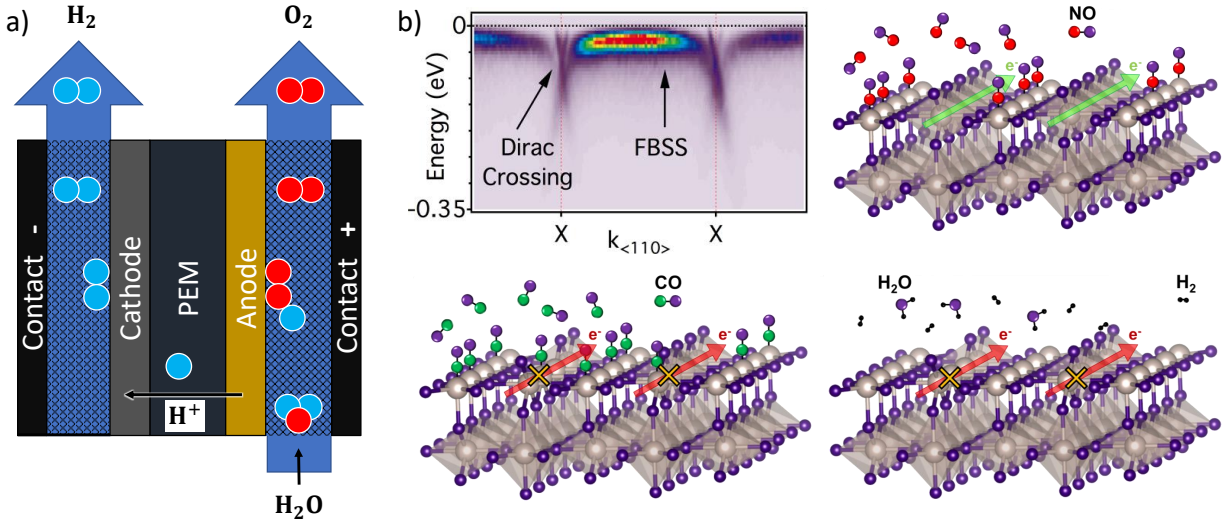

Fig. 1: a) Working principle of a proton exchange membrane (PEM) electrolyzer: water is split into hydrogen and oxygen using electrical energy. The anode and cathode consist of catalytically active material, which provides adsorption sites. The PEM conducts protons and is impermeable against gas and water. The voltage is usually applied at the outsides and the reaction takes place within porous structures (black grid). b) Angle-resolved photoelectron spectroscopy (ARPES) band map (*top left*) of a RuO_2(110) surface, which exhibits a flat band surface state (FBSS) that is anchored between two Dirac crossings. RuO_2(110) surface under NO atmosphere (*top right*): the FBSS disperses along the bridging ruthenium (Ru_{br}) chains. *Bottom:* RuO_2(110) surface under CO and H_2 atmosphere: no FBSS develops due to the removal or replacement of bridging oxygen atoms (O_{br}). (graphics from Jovic *et al.*[18,19])

trends regarding activity and stability, as well as in their adsorption properties.[20–26] As we have various RuO_2(110) thin film samples from the prior growth optimization study of Kessler[27] readily available, the following discussion will predominantly focus on the (110) surface. This is the thermodynamically most stable surface termination of RuO_2, therefore, it is a reasonable choice to approximate the properties of various polycrystalline forms of the material.

Besides its catalytic performance, RuO_2 also offers exciting properties from a solid-state physics perspective. The electronic structure of RuO_2 – a Dirac semimetal – shows a complex network of Dirac nodal lines (DNLs).[18] These DNLs give rise to a flat-band surface state (FBSS), which disperses along ⟨001⟩ oriented chains of bridging ruthenium (Ru_{br}) $4d_{z^2}$ orbitals and is stabilized by bridging oxygen (O_{br}) p_z. Within a RuO_2(110) unit cell, there is a second type of site: on top oxygen (O_{ot}) adsorbed to onefold coordinatively unsaturated 1f-cus-Ru sites (Ru_{cus}) of the stoichiometric surface. Gases with known adsorption and catalytic behavior such as NO, CO and H_2 can be utilized to manipulate the surface while observing the FBSS by angle-resolved photoelectron spectroscopy (ARPES), which is shown in Fig. 1b). It has been observed, that the FBSS collapses, if the O_{br}-chains are disturbed, meaning the oxygen is either removed or replaced by, e.g. by CO, as illustrated in Fig. 1b). This shows that the surface electronic structure is affected by typical catalytic reactions. Thus, it is alluring to search for possible correlations between electronic structure by ARPES and actual catalytic performance by electrocatalysis.[19]

As a result of its special electronic structure, antiferromagnetic ordering is proposed, and possible hints of its existence have been discovered experimentally.[28–30] Beyond producing a non-zero anomalous Hall signature, magnetic ordering could be relevant

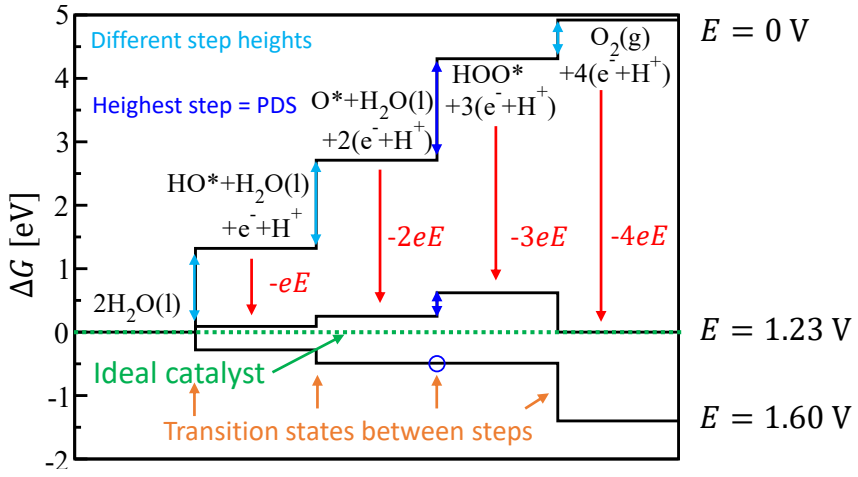

Fig. 2: Predicted free energies of the oxygen evolution reaction (OER) intermediates adapted from Rossmeisl *et al.*[32]. Four proton coupled electron transfers (PCET) are catalyzed by active surface sites (O*).

for the emerging field of spintro-catalysis. At the bottom of this field lies the intuition that converting nonmagnetic water to magnetic triplet oxygen requires a spin transfer mechanism, possibly mediated by the surface electronic structure. It has been proposed by density functional theory (DFT) calculations that the RuO_2(110) surface is able to supply the required spin.[31] To get to the bottom of the – potentially spin related – OER mechanism is the long-term goal of this project.

1.2 The oxygen evolution reaction: A link to surface science?

The water splitting standard potential $E^\circ = 1.23\,V_{RHE}$[8] would not suffice to actually split water. All voltage which has to be applied on top of that to actually drive the reaction is considered as overpotential η. There are several contributions which add up to the total overpotential: heat loss, ohmic drop over the electrolyte, depletion of reactant concentration, evolution of gas bubbles and intrinsic catalytic activity.[6] Except the latter, all other contributions are essentially self-explanatory and related to the extrinsic experimental conditions. In consequence, we will focus on understanding the intrinsic catalytic mechanism in more detail.

The overpotential of the overall process consists of the sum of overpotentials at the hydrogen evolving cathode and the oxygen evolving anode. The latter one will be discussed in further detail as it is where RuO_2 comes into play. Fig. 2 shows a free energy diagram of the four consecutive OER steps: starting with two water molecules and generating gaseous oxygen in the end. Each step consists of a proton-coupled electron transfer (PCET). O* represents an oxygen atom adsorbed to an active Ru-cus site - this is the already mentioned on top oxygen O_{ot}.

Considering the free energy staircase Fig. 2 and applying a bias of $E = 0\,V_{SHE}$, it is apparent that each step has a different activation barrier corresponding to its step height. The fundamental concept of electrochemistry is the capability to tune the free energy of all reaction steps that include electron transfer by applying an electric potential. Applying a bias of $E = 1.23\,V_{SHE}$, all steps are shifted by the difference in Gibbs

free energy $\Delta G = -neE$ thus leveling the initial and final state – n is the number of already transferred electrons. Yet, not all steps are energetically favorable – i.e. 'downstairs' – and the reaction is still blocked. At the equilibrium potential ($E = 1.23\,\mathrm{V_{SHE}}$), the forwards and backwards rate from initial to final state cancel out each other. Only an ideal catalyst (Fig. 2, green), which exhibits the same energetic height in each step (

If we further increase the potential, at a certain point even the formerly highest step becomes downwards. This step is called the potential determining step (PDS). At this stage, the whole reaction is thermodynamically favorable. The PDS offers one possibility to define the intrinsic catalytic overpotential as: the bias required to make all steps point downwards, which causes the forward rate of the reaction to exceed the backwards rate. Unfortunately this value only suffices for theoretical comparisons, but can not be determined experimentally. In an experiment, the potential-dependent reaction rate can be measured in terms of an electric current that is caused by every transferred electron contributing to the reaction. This current is already established before the PDS has been leveled. This leads to the next step on the way towards a description of the OER mechanism: The transition states, which are located in between the reaction intermediates as indicated in orange in Fig. 2.

Up to this point, all reaction intermediates are discussed in terms of stable surfaces, whose energies can be calculated by DFT.[32] As depicted in Fig. 3a), a certain activation energy $G^{\#}$ is required to bridge every step. This leads to transition state theory (TST) and the Butler-Volmer equation, relating properties of the transition state to the experimentally observed current. Fig. 3a) shows a simple model of the one-electron redox process:

$$\mathrm{Red} \overset{k_{\rightleftharpoons}}{\rightleftharpoons} \mathrm{Ox} + \mathrm{e}^-, \tag{3}$$

$$\mathrm{R} \overset{k_{\rightleftharpoons}}{\rightleftharpoons} \mathrm{O} + \mathrm{e}^-, \tag{4}$$

which dynamic chemical equilibrium occurs in both directions.

The chemical rate constants in forward and backward direction $k_{\rightleftharpoons}$ can be expressed by the Eyring equation:[33]

$$k_{\rightharpoonup} \propto \exp\left[-\frac{1}{k_\mathrm{B}T}(G^{\#} - \alpha e\eta)\right] \quad \text{(Eyring)} \tag{5}$$

$$k_{\leftharpoondown} \propto \exp\left[-\frac{1}{k_\mathrm{B}T}(G^{\#} + (1-\alpha)e\eta)\right]. \tag{6}$$

Here k_B is Boltzmann's constant, e the electron charge and T the temperature. The overpotential $\eta = E - E^\circ$ represents the voltage E related to the electrode standard or reversible potential E°. $G^{\#}$ is the standard Gibbs free energy of activation at the reversible potential, when reactant and product energy levels are equal. The Eyring equation matches the intuition that the reaction rate is exponentially suppressed with transition energy. Remembering that applying an overpotential η shifts the energy levels by $\Delta G = -ne\eta$, one can explain the terms added and subtracted in Eq. 5 and Eq. 6. In Eq. 5, the transition state energy is lowered by a certain fraction α of the charge that has already been transferred on the way from R to O. This can be interpreted in the following way: The reaction starts from R with zero transferred electrons and reaches

its final state O, where one electron is transferred – a certain fraction ($0 < \alpha < 1$) of the overall charge is transferred at the peak of the transition state. Intuitively, a fractional charge represents a partly displaced electronic orbital between the initial and final state of an electrochemical process. Likewise in Eq. 6, the activation energy is amplified by (1-α).[33]

The final steps to the experimental current density $j(\eta)$ consist in scaling the rate constants accordingly and adding the forward and backward current. This results in the generalized Butler-Volmer equation[34]:

$$
\begin{aligned}
j(\eta) &= j_0 \left\{ \underbrace{\exp\left[\frac{\beta_{\mathrm{RDS}} e\eta}{k_\mathrm{B}T}\right]}_{k_{\rightharpoonup}} - \underbrace{\exp\left[\frac{-(z-\beta_{\mathrm{RDS}})e\eta}{k_\mathrm{B}T}\right]}_{k_{\leftharpoondown}} \right\}, \quad \text{(Butler-Volmer)} \\
j_0 &= \frac{k_\mathrm{B}Tze\Gamma}{h} \exp\left[\frac{-G^{\#}_{\mathrm{RDS}}}{k_\mathrm{B}T}\right], \\
\beta_{\mathrm{RDS}} &= \gamma + \alpha_{\mathrm{RDS}},
\end{aligned}
\tag{7}
$$

where the transition state exponential is now contained within the exchange current density j_0. Γ is the number of active catalytic sites per area with a reactant ion present nearby, z is the number of electrons transferred in the overall reaction. Furthermore, the electron transfer coefficient $\beta_{\mathrm{RDS}} = \gamma + \alpha_{\mathrm{RDS}}$ generalizes the (one-step) derivation to a multi-step process like OER: employing γ to count all electrons transferred before the rate-determining step (RDS).

Fig. 3b) shows a two-step process with three stable surfaces and two transition states #1 and #2 (purple and blue). More precisely A is the starting surface, B is a reaction intermediate and C is the starting surface with the desired product, e.g., oxygen gas. The following discussion can also be generalized to a starting and final surface with three reaction intermediates as it would be in the case for OER. The following discussion is based on the work of Exner *et al.*[34]. Assuming the desired reaction proceeds from left to right, at zero overpotential the reaction would be in chemical equilibrium and not be favorable yet. However, at or above a certain overpotential, the reaction will proceed and the second step (Fig. 3b), blue) will become rate-determining. This is the case as long as the second transition state #2 is higher than #1. In this situation, A is in a pre-equilibrium with B while the last step represents the bottleneck of the whole reaction by having the slowest rate constant. Thus only the properties of the RDS are reflected in the OER current.

As the contribution of the backwards reaction gets exponentially less important with more positive overpotential in the forward regime, Eq. 7 simplifies to a single exponential:

$$
j(\eta) = j_0^{\mathrm{RDS}} \exp\left[\frac{\beta_{\mathrm{RDS}} e\eta}{k_\mathrm{B}T}\right]. \quad \text{(Tafel)} \tag{8}
$$

In the current case, i.e., if step #2 is rate-determining, the electron transfer coefficient β would account for the charge already transferred ($\gamma = 1$, from A to B in Fig. 3b)) and the partially transferred charge $\alpha_{\#2}$ at the peak of the transition state ($\beta_{\mathrm{RDS}} = \gamma + \alpha_{\mathrm{RDS}} =$

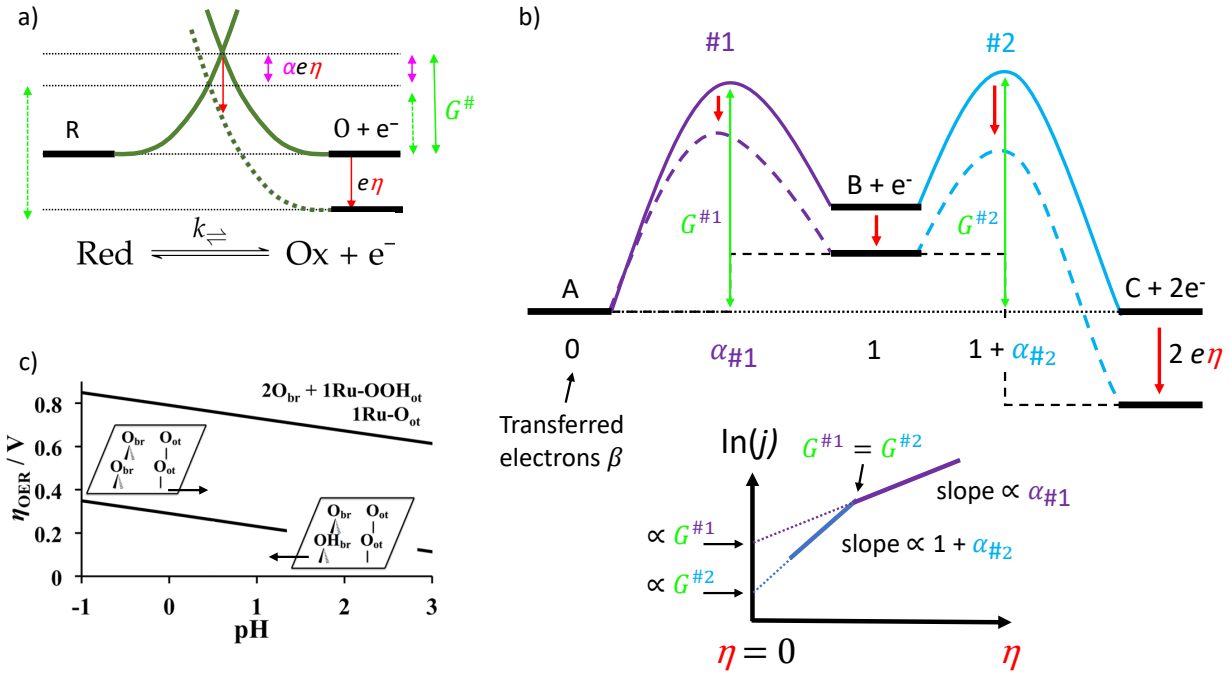

Fig. 3: a) Sketch of the free energy diagram of the one electron reaction R ⇌ O + e⁻. The transition state free energy $G^{\#}$ depends on the applied overpotential η. b) Sketch of the free energy diagram of a two-electron reaction, which proceeds over transition state B. The number of transferred electrons is shown underneath, including the fractional electron transfer coefficients α of the transition states #. c) Surface Pourbaix diagram of RuO_2(110) from Exner *et al.*[34]. The overpotential is measured versus the OER standard potential at pH 0.3.

$1 + \alpha_{\#2}$). There is one exception to this counting rule: If the RDS is a purely chemical one, thus no charge transfer with the catalytic surface, α_{RDS} is always zero. An example would be a dissociative water adsorption at the two active sites $*$ of the RuO_2(110) surface: $2* + H_2O \rightleftharpoons *OH + *H$ – no charge is required to balance this reaction.[34] The lower potential region of the overpotential-current characteristic (see Fig. 3b)) is determined by Eq. 8.

Further increasing the overpotential leads to the situation illustrated by dashed lines within the energy diagram in Fig. 3b). Note that transition state #1 has now the highest free energy and becomes rate-determining. As Eq. 8 always depends on the current RDS, j_0 changes as well as β ($\beta_{RDS} = \gamma + \alpha_{RDS} = 0 + \alpha_{\#1}$). This explains the transition within the higher overpotential region (purple) in Fig. 3b). The linear regimes are also known as Tafel regions, Eq. 8 is likewise called Tafel equation. As depicted in Fig. 3b), plotting the logarithmic current versus the overpotential allows for the extraction of the transition state free energy $G^{\#}$ from the intercept at zero overpotential $\eta = 0$, which yields the exchange current density j_0 according to Eq. 7 and Eq. 8. The slope contains β_{RDS}.

It is worth noting that in a multi-step situation there is the possibility of shadowed steps. One could imagine a situation with a third transition state with lower free energy than #2 at zero overpotential situated to the right of it. This step would never become rate-determining, which is synonymous to *visible* within the given context.

A further complication, which is proposed to occur at the RuO_2(110) surface[34], is a change in the starting surface under varying starting conditions – this will be explained

hereafter. This occasion will further be utilized to introduce the reader to a related concept: the Pourbaix diagram. Fig. 3c) shows an example of such a diagram in terms of thermodynamically stable (DFT-predicted[34]) surface configurations of $RuO_2(110)$ depending on the applied potential and the pH value of the reaction medium. In the present case increasing the overpotential at fixed pH leads to a phase transition: the configuration with 0.5 protons per bridging oxygen (O_{br}) transforms to the fully oxygenated unit cell. In the simplified model of Fig. 3b) this would correspond to increasing the overpotential until the reaction intermediate (middle) overtakes the starting surface energetically – this is not sketched. This situation implicates that the former reaction intermediate takes the role of the stable starting surface, which, in fact, it is henceforth. Thus one catalytic cycle will start and end at this surface, therefore changing the way transferred electrons β_{RDS} have to be counted. In the given example, the rate-determining transition state #1 remains, but is not the first electron transfer (counting from A) anymore. Counting from B it becomes the second electron transfer. Consequently, yet another linear Tafel region would arise within the potential range where this applies. In general, reaction intermediates can show up in surface Pourbaix diagrams, but it is not excluded that other adsorbates, which do not necessarily take part in the catalytic cycle, are energetically more favorable.[34]

At this point, it is noticeable that in spite of the – misleading – insinuation of the potential-determining step (PDS), (Fig. 2) an OER current will establish before every single reaction steps becomes downstairs – meaning that some reaction intermediates still have higher free energy than the initial state. The reasoning behind this is that the PDS concept only includes stable (steady-state) surface configuration energies and draws conclusion about reaction rates based on this. In contrast, transition state theory (TST) focuses on the actual chemical reaction kinetics, whose are controlled by the higher energy (than stable reaction intermediate surfaces) transition states. TST basically completes the picture by introducing transition states into the simple staircase picture from Fig. 2. The concepts of TST underlie the interrelation of microscopic surface processes and macroscopic quantities that are observable by electrochemical methods. In a nutshell, the logarithmic slope of a current-potential characteristic (Tafel slope) permits a direct consistency check of a proposed OER pathway within the framework of TST by counting transferred electrons between the starting surface and contemplable transition state. In addition, the TST offers to reconstruct the whole free energy surface of the reaction by combining information from theory and experiment as demonstrated in the work of Exner *et al.*[34]. The transition state free energies are determined experimentally while the stable surface reconstructions , i.e., reaction intermediates can be determined by density functional theory (DFT). Another connection between microscopic and macroscopic quantities comes from surface Pourbaix diagrams at lower potentials where OER is not feasible yet. When a phase transition occurs, it is correlated to electron transfer and consequently generates a measurable current. This will become the second main concept of the present work.

Finally a connection to the chapter's motivation part (section 1.1) can be established. The OER mechanism with its different adsorbed reaction intermediates illustrates which properties a good catalyst has to offer. First of all it needs an active site just as the 1f-cus Ru which moderately binds – in this case – O, OH and OOH (Fig. 2) and is still able to release the final product O_2. Exactly this fine balance between easy adsorption and not too demanding desorption energies of the cus-sites – not those where O_{br} adsorb

– causes the RuO_2(110) surface to be such a benchmark catalyst.[1] To this end, it is emphasized that a single crystalline model system is required to investigate the presented concepts. Therefore, in the scope of these considerations, RuO_2(110) thin films will be characterized and classified throughout this thesis.

2 Fundamental Aspects of Electrochemistry

After briefly introducing the way of thinking in terms of electrochemical standard potentials and electrode reactions based on a simple lemon battery, the standard three electrode setup is exemplified by cyclic voltammetry (CV) at platinum (Pt). The theoretical basis, which is needed to also quantitatively understand the cyclic voltammogram of Pt and all experimentally related concepts, is discussed afterwards.

2.1 The basic setup

2.1.1 The lemon battery: A typical two-electrode experiment

One of the simplest conceivable electrochemical experiments is the well-known lemon battery. It can be easily built by sticking a copper and a zinc electrode into a lemon as depicted in Fig. 4a). The citric acid establishes electrolytic contact, specifically ionic conductivity. Because of the different locations of Cu and Zn within the galvanic series, a voltage between the two half-cells is expected. Its approximate value can be determined by subtracting the tabulated standard potentials[35] E° of the half reactions:

$$\text{Copper electrode:} \quad \mathrm{Cu^{2+}_{(aq)}} + 2\,\mathrm{e^-} \longrightarrow \mathrm{Cu_{(s)}}, \qquad E^\circ_{\mathrm{Cu}} = 0.34\,\mathrm{V} \tag{9}$$

$$2\,\mathrm{H^+_{(aq)}} + 2\,\mathrm{e^-} \longrightarrow \mathrm{H_{2(g)}}, \qquad E^\circ_{\mathrm{H_2}} = 0\,\mathrm{V} \tag{10}$$

$$\text{Zinc electrode:} \quad \mathrm{Zn^{2+}_{(aq)}} + 2\,\mathrm{e^-} \longrightarrow \mathrm{Zn_{(s)}}, \qquad E^\circ_{\mathrm{Zn}} = -0.76\,\mathrm{V} \tag{11}$$

$$\text{Lemon battery:} \quad \mathrm{Zn_{(s)}} + 2\,\mathrm{H^+_{(aq)}} \longrightarrow \mathrm{Zn^{2+}_{(aq)}} + \mathrm{H_{2(g)}}, \quad E^\circ_{\mathrm{H_2}} - E^\circ_{\mathrm{Zn}} = 0.76\,\mathrm{V}. \tag{12}$$

Eq. 9 and Eq. 10 actually reveal two possible reactions at the copper electrode: Cu^{2+} being reduced to Cu or the evolution of hydrogen – which we already know as HER.

These two reactions point towards a common misconception, which can be triggered in case, e.g., a general chemistry textbook uses a lemon battery to motivate the Daniell element (Cu-Zn-battery).[36] The Daniell element corresponds to Eq. 9, i.e., copper ion deposition. In the case of a Lemon, there are no copper ions present in the electrolyte, but rather aqueous protons from the citric acid. Besides the HER, the Zn electrode is dissolved into the electrolyte.[36]

At this point, it is important to note that electrochemical standard potentials are, by definition, reduction potentials. The arrow directions in case of Eq. 9-Eq. 11 are chosen accordingly, which means that the arrow points towards the reduced species of the reaction. This is important to enable an unambiguous definition of the sign of the related standard potentials. Consequently, the negative sign relative to the HER in the last case indicates that Zn will spontaneously be oxidized (dissolved), rather than

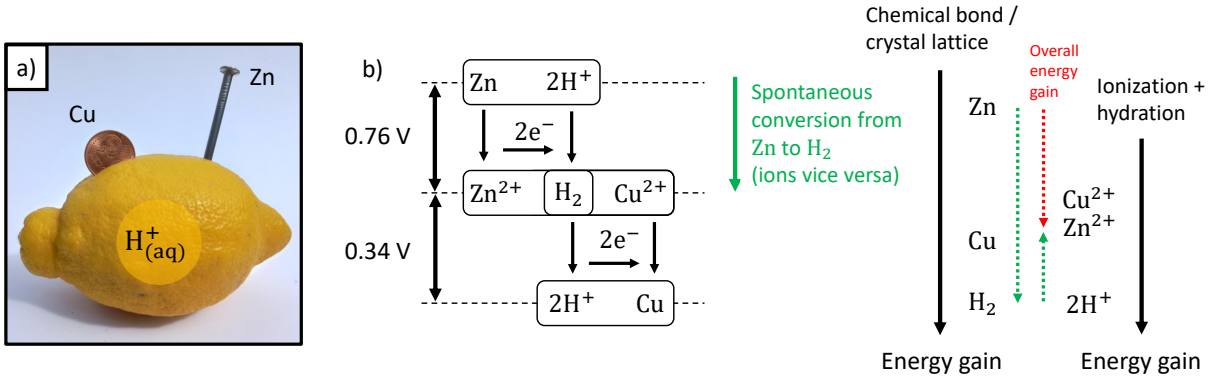

Fig. 4: a) A lemon battery is built by sticking a copper coin and a zinc plated nail into a lemon, which acts as acidic electrolyte by providing aqueous protons (H^+_{aq}). b) The electrode standard potentials are determined by the absolute energy gain of an arbitrary redox couple versus the H^+/H_2-couple. In the case of Zn^{2+}/Zn, overall, the system gains energy as the hydrogen bond formation is favored over the lattice cohesive energy of Zn. At the same time, this (more than) compensates the combined ionization and hydration energy that is lost during the step from H^+ to Zn^{2+}. The sketched (free) energy values are not to scale but illustrate the approximate relative relationships. Data taken from Schmidt-Rohr[37].

reduced, when connected to a hydrogen half-cell. Furthermore, standard potentials are only valid at defined standard conditions.

The galvanic series motivates the emerging potential difference. This empirically found motivation is simple, but not satisfactory in explaining the actual driving mechanism. Nevertheless, there is an intuition that offers a bit more than a simple 'energetically more favorable'. The standard potentials from the galvanic series are correlated to the lattice cohesive energy of bulk metals, as well as to their ionization energies in water (including the hydration energy).[37] This concept of checking the energy gain or loss of the overall system by comparing lattice cohesive (or bond formation) energy and ionization and hydration energies is illustrated in Fig. 4b) (including the H^+/H_2-couple as reference).

The lemon battery reveals an intrinsic problem of two-electrode measurements: In contrast to probing reactions of either the copper or the zinc electrode individually, the overall cell voltage comprises contributions of both metals. Consequently, a third electrode with a stable and well defined standard potential, known as reference electrode (RE), has to be introduced. Although in this specific case one electrode reaction appears to be at the defined zero voltage point, it should be emphasized that the simplistic assumption of standard conditions does not reflect reality. Furthermore, no complications of externally applying a voltage and measuring a current have been considered yet.

2.1.2 The three-electrode setup illustrated with platinum

Fig. 5a) shows the next simplest electrochemical experiment, which clears the way for quantitative measurements. Two Platinum wires (99.95%) and a RE are dipped into 1 M H_2SO_4 electrolyte. One of these wires is the device under test, also known as the working electrode (WE).

As already mentioned, the RE has a known and stable (over time) potential. The general convention is to report all electrochemical potentials versus the standard hydrogen

electrode (SHE), a conceptual RE which will be explained later (subsection 2.2.1). For now, it is important to realize that there are no absolute electrochemical potentials. Thus, the zero point is defined to be at the hydrogen reduction potential: $E^{\circ}_{H_2} = 0\,V$. To avoid obstructing the governing reaction of a RE, ideally no current should flow through it.[33] A current through the RE would trigger an electrochemical reaction, which would in turn cause the potential to drift. If no current can flow through the RE, then one needs an additional current collector which can make up for electrochemical reactions of the WE. This current collector is called counter electrode (CE). There are several inert materials that can be utilized, which one is the best depends on the specific electrochemical issue. Platinum metal (Pt) is an excellent example CE candidate for a range of electrochemical processes (including the OER) as it is quite inert and corrosion resistant over a considerable potential window. The CE should have a larger surface area than the WE to avoid restrictions of the maximum observable current density at the latter one.[33]

In the following text, two very instructive limiting cases of platinum experiments will be discussed. First, a slow 'steady-state' voltage sweep with a scan rate of $\nu = 1\,mV\,s^{-1}$, starting from low (negative) potentials, is performed. (see Fig. 5b)) Below $0\,V_{SHE}$ the absolute current rises exponentially due to the HER, while it behaves similarly at the other potential limit due to the OER. In both cases, the evolving gases can be observed in form of rising bubbles. This is basically the same situation as for the PEM electrolyzer with its hydrogen evolving Pt cathode. The fact that there is already a considerable current near the hydrogen evolution standard potential ($0\,V_{SHE}$) underlines the efficiency of Pt in catalyzing this reaction, thus keeping the overpotential low. At these relatively slow scan rates, the current on the way to more positive – anodic – potentials is negligible compared to the water splitting reactions. Therefore the intermediate potential range is mostly flat.

As the OER standard potential of $E^{\circ} = 1.23\,V_{SHE}$ is surpassed, as expected, there is no direct oxygen related current yet. Above the activation barrier, when a sufficient overpotential is applied, the current rises. However, the required overpotential is way higher than that of a ruthenium oxide electrode.[40] This emphasizes that, in principle, most electrode materials are able to anodically split water, but some perform better than others. Hence RuO_2 would be favored over Pt as anode OER-catalyst. In the case of Pt, the lack of OER-activity is partly caused by the build-up of poorly conducting oxide layers within the relevant potential region.[41,42] Their voltammetric response will be discussed subsequently.

Fig. 5c) shows a cyclic voltammetry (CV) experiment performed at 600 times faster scan rate ($\nu = 600\,mV\,s^{-1}$) than the linear sweep just shown. In this fast scan rate limit the surface redox transitions are enhanced. Intuitively, if a certain charge is attributed to a potential-dependent surface redox process, this charge has to be transferred in less time at higher potential scan rates – the current is enhanced. The potential range is chosen to be within the limits of the gas evolving reactions. A cyclic voltammogram is created by alternate linear sweeps from lower to higher potentials and vice versa. If the occurring electrochemical processes do not change over time, a stable response is expected after a few initial cycles. The curve depicted here already reached that state.

A single cyclic voltammogram contains a lot of information, as the textbook example Pt demonstrates. Starting at $0.3\,V_{SHE}$ a mostly constant charging current establishes until about $0.8\,V_{SHE}$. This is known as the double-layer region, to which a whole section is dedicated, but for now it can be thought of as charge which reorganizes in front of

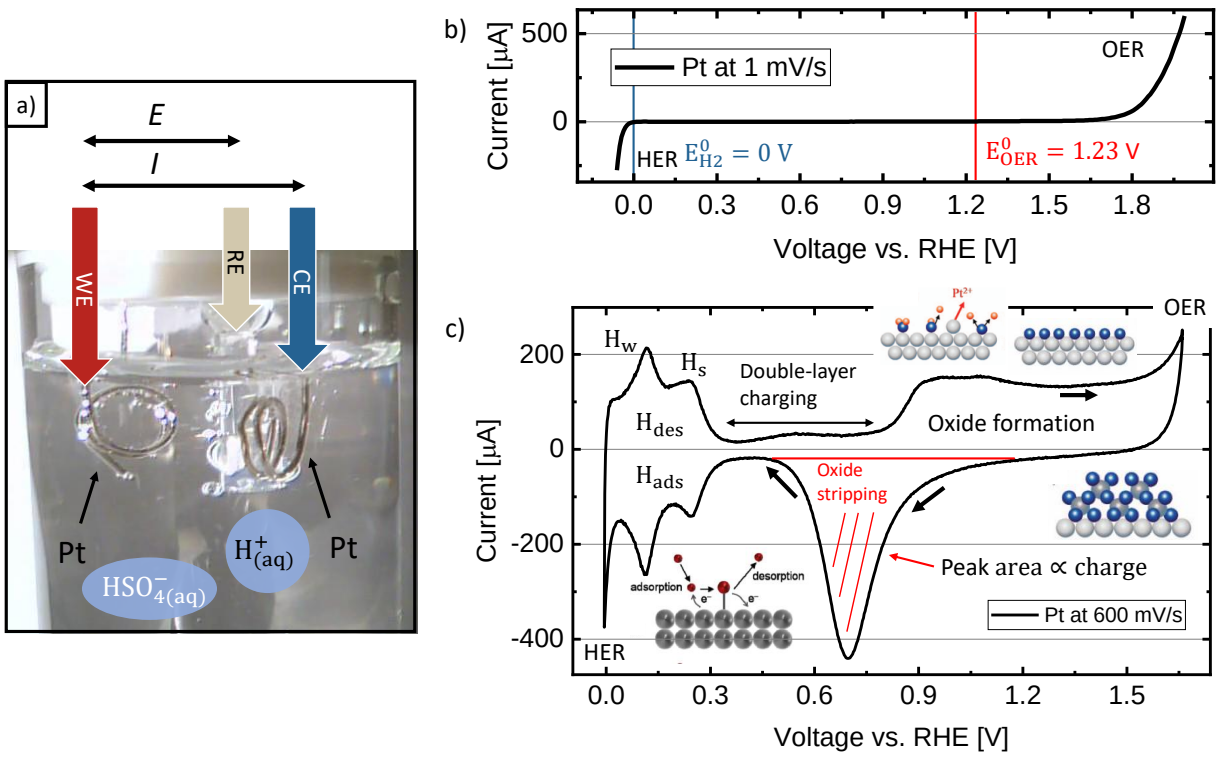

Fig. 5: a) The simplest three electrode setup: Platinum (Pt) wires act as counter (CE) and working electrode (WE). They are immersed into 1 M H_2SO_4 electrolyte together with a reference electrode (RE). A controlled current is applied between CE and WE while the voltage is measured between RE and WE. b) A slow linear sweep voltammogram of Pt starting from low potentials, which is recorded at a scan rate of $1\,mV\,s^{-1}$ in 1 M H_2SO_4 electrolyte. c) A fast cyclic voltammogram of Pt, which is recorded at a scan rate of $600\,mV\,s^{-1}$ in N_2-saturated 1 M H_2SO_4 electrolyte. All typical potential dependent surface reactions are visible: hydrogen (H_{upd}) and oxygen (O_{upd}) underpotential deposition as well as desorption (H_{des}, O_{des}). Furthermore, the weak (H_w) and strong (H_s) hydrogen adsorption peak pairs are indicated. Illustrations of the Pt surface reactions are taken from: Sugawara *et al.*[38] and Wongbua-ngam *et al.*[39].

the metal surface. It behaves just like a capacitor, where the charging current is proportional to the potential scan rate ν. The subsequent rise of the current can be attributed to the build-up of the Pt-oxide layer, which has already been referred to in the context of hindering the OER.[38] Pt-oxides can reach from adsorbed oxygen, over a monolayer oxide, up to multiple layers. Furthermore, anodic dissolution of platinum metal becomes favorable, even though the oxides serve as a protective layer up to a certain degree.[38]

Reversing the potential just before the OER onset results in an oxide reduction peak with a maximum at around $0.7\,V_{SHE}$. The charge attributed to this feature is correlated to the time the electrode has spent at elevated potentials.[43] A negative sign current is reasonable for a reduction process as electrons are supplied by the electrode. Because the PtO_x oxide layer, as soon as it built up, behaves rather resistant towards reduction, this process does not readily take place at the same speed by reversing the potential, but has its maximum located at lower potentials.[44] After the oxide reduction finished, just the underlying double-layer charging current remains.

Below $0.3\,V_{SHE}$ two pairs of peaks, which are symmetric with respect to the zero current abscissa, show up. These are known as hydrogen underpotential deposition (UPD) peaks, because they appear at potentials positive to the actual hydrogen reduction (to gas). As the name suggests, the peaks are related to hydrogen adsorption onto the Pt surface:[44]

$$H^+ + e^- \rightleftharpoons H_{ads}. \tag{13}$$

This process is very fast relative to the potential scan rate. It can be readily reversed by reversing the potential, thus, it is also known as a reversible process. The symmetry (relative to the zero current axis) of the peak pairs is a characteristic feature of this type of electrochemical reaction. It is intuitive, that this process is less complex than the oxide layer buildup, as protons are readily available under acidic conditions and it only involves a single electron transfer. In case of polycrystalline Pt, two pairs of hydrogen adsorption peaks appear: strong adsorption at higher potentials (H_s) and weak adsorption at lower ones (H_w). This is related to two different types of surface adsorption sites. Hydrogen obviously needs less extra electrical energy to adsorb at sites of stronger adsorption, therefore it needs less reductive – equivalent to higher potentials – conditions compared to the weakly adsorbing sites.[45] Reversing the potential before HER sets in, reverses the process and the corresponding desorption features appear. The charge related to a certain peak can also be utilized to estimate the electrode's surface area by assuming one monolayer of adsorbed hydrogen with a single electron transfer for each site.[45,46]

The preceding discussion illustrates how sensitive CV is towards surface reactions and how it can provide a plethora of exciting insights about the WE within a few seconds. On top of that, more detailed studies of Pt single crystals were even able to correlate CV features to surface step densities and, moreover, certain types of steps stemming from different surface orientations.[45]

2.1.3 Selection of the electrolyte

The first decision which has to be taken is whether to work under acidic or alkaline conditions. As the OER mechanism differs under alkaline conditions[6,12] due to the

presence of OH^--ions and because of RuO_2's specialty to perform well under the acidic conditions of a PEM-electrolyzer[6], acidic conditions are of interest in this thesis.

Two electrolytes can be ruled out directly. Hydrochloric acid (HCl) contains chloride anions, which make a side reaction next to the desired OER possible: Namely the chloride oxidation to chlorine gas (CER), already mentioned related to the chlor-alkali electrolysis in the first chapter.[15,47] Phosphoric acid H_3PO_4 shows problems which arise from the presence of phosphate anions. CV features of RuO_2 appear damped in phosphoric acid electrolyte[48] or phosphate salt[49] containing solutions. Both studies conclude that phosphate adsorbs to the surface and obstructs sites participating in surface reactions.

Judging from the literature, perchloric acid ($HClO_4$) and sulphuric acid (H_2SO_4) fulfill the requirement of providing aqueous protons ($H^+_{(aq)}$), while their anions do not affect the surface reactions.[21,49–52] Therefore, sulphuric acid is chosen in this thesis.

As mentioned above, the main job of the electrolyte is to provide $H^+_{(aq)}$ and consequently protonic conductivity via the Grotthuss mechanism. A simple picture of this mechanism can be made up of protons jumping along chains of H_2O, forming $H_3O^+_{(aq)}$ on their way – this explains why protons diffuse more rapidly than other aqueous anions or cations. Even though it does not change the consequences of this mechanism, it should be mentioned that the hydronium ion does not reflect reality and more complex structural models of aqueous protons have been verified by now.[53]

Next to offering conductivity the presence of protons raises the question of the electrolytes pH. The pH depends on the (molar) concentration of aqueous protons $[H^+]$ as follows:

$$\mathrm{pH} = -\log([\mathrm{H}^+]), \tag{14}$$

where the molar concentration (indicated by square brackets) $[H^+]$ is measured in units of $1\,\mathrm{mol\,dm^{-3}}$.

H_2SO_4 is a diprotic acid, meaning it can release two protons consecutively depending on the solution pH. Which ionic species is mostly present depends on the acid dissociation constant pK_a of either the H_2SO_4/HSO_4^- or the the HSO_4^-/SO_4^{2-}-couple. In the case of sulphuric acid the first couple is commonly recognized as strong acid, while the second one as weak acid. The actual pH-pK_a relationship to anionic species concentrations can be estimated for a monoprotic weak acid by the Henderson-Hasselbalch equation:

$$10^{(\mathrm{pH}-\mathrm{p}K_\mathrm{a})} = \frac{[\mathrm{A}^-]}{[\mathrm{AH}]} \tag{15}$$

with AH being the protonated version of the anion A^-. Intuitively, this tells that 2 pH above the pK_a, 99% of the AH/A^--couple is dissociated to A^-, and, 2 pH below, just 1% is in the deprotonated state. The pH of the mainly used 1 molar sulphuric acid solution ($1\,\mathrm{M}\ H_2SO_4$) – this implies a concentration of 1 mole H_2SO_4 per liter of solution – can be estimated[54] to $\mathrm{pH} \approx 0.1$. From this, the actual concentration of sulphuric acid's ionic species could be extracted from a pH-concentration-plot called Bjerrum plot or Hägg-diagram. In the present case, a simple estimation will be possible and suffice.

As the acid dissociation constant of the first deprotonation is $pK_{a1} = -3$, it can be concluded from Eq. 15 that mostly HSO_4^- is present. This is because the electrolyte's pH

(pH $\approx$ 0.1) lies more than 2 pH above the pK_{a1}-value of -3. Furthermore, it is nearly 2 pH below the second dissociation constant of p$K_{a2} = 2$, meaning that SO_4^{2-} is not formed yet. This indicates that every sulphuric acid molecule contributes approximately one proton to the solution. This provides a successful consistency check as a pH of zero indicates a proton concentration of $1\,\mathrm{mol\,dm^{-3}}$ – just the same as the molecular acid concentration.[55]

2.1.4 Control loop of the potentiostat

Current-voltage characteristics of platinum have already been presented, while tacitly avoiding the discussion of how they were actually measured with a three-electrode setup. The operating principle of a potentiostat is illustrated in Fig. 6a) by a simplified equivalent circuit. A potentiostat is able to adjust the WE potential by controlling the current through CE and WE.

To recap, the RE measures the potential drop at the WE but is not able to carry current, while current is provided by the CE. The control amplifier is a cartoon of the digital control loop of a real potentiostat. Within this control system, the process variable is the voltage drop between RE and WE, which is compared to an externally specified setpoint-voltage E_i. Connecting both voltages to the inverting and non-inverting inputs of the control amplifier results in a current output proportional to their difference. Hence, the controlled variable is the current passing through the cell between CE and WE. As the WE-voltage is determined by the occurring electrochemical, i.e. current inducing, reactions, it can actually be regulated by this current, and the control loop closes. To finally obtain a current-voltage characteristic, the current is measured by the shunt resistance R_m and plotted versus the setpoint, which corresponds to WE-voltage.[35]

2.2 Reference electrodes and the Nernst equation

2.2.1 Electrochemical equilibrium and the Nernst equation

The subsequent brief introduction to the (electro-)chemical equilibrium follows the standard reference of Compton *et al.*[35]. Chemical equilibria are usually described by three thermodynamic state variables, namely: temperature T, pressure p and particle number n. The thermodynamic potential which depends explicitly on these variables is the Gibbs free energy $G(T, p, n)$. A thermodynamic potential is constructed in such a way that it becomes minimal, when the system of interest including its environment reaches maximum entropy under given constraints. This is a consequence of the second law of thermodynamics. Consequently, the Gibbs free energy is able to predict concentrations of chemical reagents under equilibrium conditions, but contains no kinetic information. To find out what drives a reaction, changes of the Gibbs potential ΔG have to be considered

$$\Delta G = -S\Delta T + V\Delta p + \mu\Delta n \tag{16}$$

with entropy S, volume V and the chemical potential μ. Starting from an out of equilibrium state – like directly after mixing two reactive compounds – a chemical reaction will occur until $\Delta G = 0$.

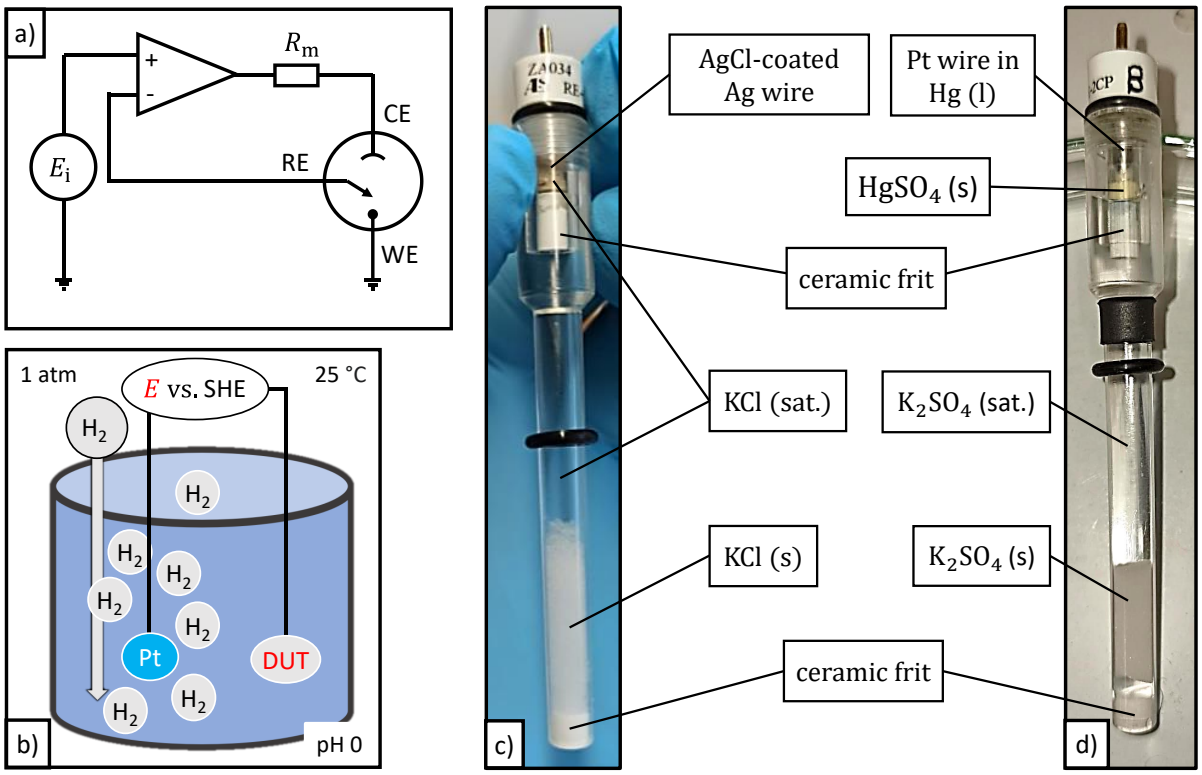

Fig. 6: a) A simplified equivalent circuit of a potentiostat connected to an electrochemical cell. The current is measured via shunt resistor R_m and controlled by an operational amplifier. The set point voltage is externally supplied by voltage E_i. b) Sketch of a standard hydrogen electrode (SHE): All electrochemical potentials that are measured versus this standard setup are by definition recorded against $E = 0\,V_{SHE}$. Pictures of the used commercial reference electrodes (RE) are shown in c) (Ag/AgCl) and d) ($Hg/HgSO_4$).

Now this concept will be further elaborated using the electrochemically important example of the Standard Hydrogen Electrode (SHE), from which we will eventually derive the Nernst equation: All electrochemical potentials are measured against a defined reference reaction: the reduction of hydrogen

$$2\,\mathrm{H}^{+}_{(\mathrm{aq})} + 2\,\mathrm{e}^{-} \longrightarrow \mathrm{H}_{2(\mathrm{g})}, \quad E^{\circ}_{\mathrm{H}_2} = 0\,\mathrm{V} \tag{17}$$

under standard conditions. Standard conditions are defined by a pressure of 1 bar, temperature of 25°C and an (aqueous proton) concentration of 1 mol dm^{-3}. An experimental realization can be achieved by a platinum wire immersed in a hydrogen gas saturated and bubbled electrolyte of pH = 0 as depicted in Fig. 6b).[56] All electrochemical potentials measured against this half-cell would by definition be versus SHE ($\mathrm{V_{SHE}}$).

Now back to answering the question of how electrochemical reactions are related to voltages. Under fixed temperature and pressure conditions, the change of Gibbs free energy, which determines the electrochemical equilibrium, is given by the chemical potential μ_x of a reacting species

$$\mu_\mathrm{x} = \left(\frac{\partial G}{\partial n_\mathrm{x}}\right)_{T,p} \tag{18}$$

with n_x being the concentration of the species x. Including also electrical energy, the electrochemical potential

$$\bar{\mu}_\mathrm{x} = \mu_\mathrm{x} + z_\mathrm{x} F\phi \tag{19}$$

is defined with ϕ being the applied potential, z the charge of the species and $F = N_\mathrm{A} e$ the Faraday constant. The Faraday constant is the charge of one mole of electrons as the Gibbs energies are also given per mole.

From Eq. 18 combined with the equilibrium condition, it follows that the hydrogen oxidation will proceed until the sum of all electrochemical potentials of reactants and products are equal at constant temperature and pressure. Applying this to Eq. 17 leads to

$$2\bar{\mu}_{\mathrm{H}^+} + 2\bar{\mu}_{\mathrm{e}^-} = \bar{\mu}_{\mathrm{H}_2}, \tag{20}$$

further inserting Eq. 19

$$2(\mu_{\mathrm{H}^+} + F\phi_\mathrm{s}) + 2(\mu_{\mathrm{e}^-} - F\phi_\mathrm{m}) = \mu_{\mathrm{H}_2}, \tag{21}$$

where ϕ_s and ϕ_m represent the potential of the solution and the metal, respectively. As hydrogen gas carries no charge, it is not affected by the electrical potential. A general expression for conditions that differ to the standard conditions is required.

The standard chemical potentials μ^0 are related to the ones corrected for non-standard conditions in the following way:

$$\mu_{H^+} = \mu^0_{H^+} + RT \ln\left(\frac{c(H^+)}{[]^0}\right), \tag{22}$$

$$\mu_{H_2} = \mu^0_{H_2} + RT \ln\left(\frac{p_{H_2}}{p^0}\right), \tag{23}$$

where $[]^0 = 1\,\mathrm{mol\,dm^{-3}}$ and $p^0 = 1\,\mathrm{bar}$ and indicate that the quantities are measured relative to standard concentration and pressure respectively. The stated corrections to the standard chemical potentials can be derived from statistical mechanics[57], e.g., for Eq. 22: The starting point is the partition function of an ideal gas (or ideal solution), taking the logarithm yields the Helmholtz free energy (connected to the Gibbs free energy by Legendre transformation), after the Stirling approximation for a large ensemble has been applied, the chemical potential can be derived by taking the derivative of the Gibbs free energy according to Eq. 18.

As we will need it frequently, the common chemistry convention of measuring concentrations relative to the standard concentration and indicating molar concentration with square brackets $[H^+] \equiv \frac{c(H^+)}{[]^0}$ will be used throughout this thesis. For consistency the pressure relative to standard concentrations is defined as $\tilde{p}_{H_2} \equiv \frac{p_{H_2}}{p^0}$.

Combining all of the latter equations Eq. 21-Eq. 23 leads to the desired expression of the voltage drop between metal and solution

$$\phi_m - \phi_s = \frac{\Delta\mu^0}{F} + \frac{RT}{F} \ln\left(\frac{[H^+]}{\tilde{p}^{1/2}_{H_2}}\right), \tag{24}$$

where $\Delta\mu^0$ is the difference of standard chemical potentials corrected by pressure, temperature and the proton concentration, i.e., pH. R is the universal gas constant. Both the Faraday as well as the universal gas constant are connected to k_B and e by Avogadro's constant N_A: $\frac{k_B \cancel{N_A}}{e \cancel{N_A}} = \frac{R}{F}$. The final step in deriving the common form of the Nernst equation consists of identifying the standard chemical potential change with the standard electrode potential E° of the specific reaction:

$$E_{H_2} = E^\circ_{H_2} + \frac{RT}{F} \ln\left(\frac{[H^+]}{\tilde{p}^{1/2}_{H_2}}\right), \tag{25}$$

or in the generalized version with the chemical equilibrium constant K:

$$E = E^\circ - \frac{RT}{nF} \ln(K), \quad K = \frac{[\mathrm{Red}]}{[\mathrm{Ox}]}. \quad \text{(Nernst)} \tag{26}$$

n is the number of transferred electrons of a process: Ox + ne^- $\rightleftharpoons$ Red. By means of Eq. 26, the electrode potential of every electrochemical reaction can be determined away from standard conditions, assuming chemical equilibrium.

Eq. 29 allows for the introduction of the reference system, which will be used from now on. The reversible hydrogen electrode (RHE) is defined by Eq. 29 at standard pressure. Consequently, this reference is pH-dependent as it accounts for the shift expected with changing of proton concentration. Keeping in mind the goal of investigating the OER, it represents a useful concept as the actual water-splitting electrode potential experiences the same pH-dependent shift. Accordingly, the OER-overpotential can be defined as:

$$\eta(E_{\mathrm{RHE}}^{\mathrm{measured}}) = E_{\mathrm{RHE}}^{\mathrm{measured}} - E_{\mathrm{OER}}^{\circ} = \left(E_{\mathrm{SHE}}^{\mathrm{measured}} + \frac{\ln(10)\, RT}{F} \mathrm{pH} \right) - E_{\mathrm{OER}}^{\circ} \tag{27}$$

$$\approx \left(E_{\mathrm{SHE}}^{\mathrm{measured}} + 59\,\mathrm{mV} \cdot \mathrm{pH} \right) - 1.23\,\mathrm{V} \tag{28}$$

where the latter equation is evaluated at 25 °C and the labels indicate relative to which reference system the measured potentials E are reported. Here we used:

$$E_{\mathrm{H_2}} - E_{\mathrm{H_2}}^{\circ} = -\frac{RT}{F} \ln(10) \log \left(\frac{1}{[\mathrm{H^+}]} \right). \tag{29}$$

This expression is ready to insert the definition of the pH. Note that a potential of an electrode measured relative to the reference system increases when the RE potential drops.

2.2.2 Reversible hydrogen electrode versus practical references

The simplified sketch of a SHE in Fig. 6b) already suggests that this is not the most feasible realization of a RE. Hence, in most experiments, more compact solutions are chosen. Two of them, which have been used during this work, are shown in Fig. 6c) and d).

Fig. 6c) shows a commercial silver/silver-chloride electrode (AgCl). It offers a known and stable potential, which is determined by the following chemical reaction:

$$\mathrm{AgCl_{(s)}} + \mathrm{e^-} \rightleftharpoons \mathrm{Ag_{(s)}} + \mathrm{Cl^-_{(aq)}}. \tag{30}$$

On the timescales of an electrochemical experiment this reaction reaches its equilibrium conditions almost instantly. Using the Nernst equation the potential versus the SHE can be evaluated to:

$$E_{\mathrm{AgCl}} = E_{\mathrm{AgCl}}^{\circ} - \frac{RT}{F} \ln([\mathrm{Cl^-}]). \tag{31}$$

In general the Nernst equation only applies for solution (or gas phase) species.[35] Eq. 31 stresses the importance of the chloride ion concentration within the reference system to maintain a stable potential. Furthermore, the solubility of AgCl is extremely low on the relevant timescales, otherwise the potential would change when the metal-salt dissolves.

This reaction is realized as illustrated in Fig. 6c). On top of the electrode, there is an inner compartment that holds a AgCl-coated Ag wire surrounded by saturated KCl solution. Choosing a saturated solution ensures the concentration remains stable under

constant temperature conditions. As this RE is immersed into 1 M H_2SO_4 (a relatively aggressive environment in this context), the inner reference element is inserted into a second compartment, which is separated by a ceramic frit. The frit is a microporous glass that allows for ionic conduction, yet it prevents direct simultaneous mixing of the solutions within each compartment. In the lower compartment, solid KCl crystals are present within the saturated KCl solution to keep it saturated at all times. This compartment is made of polymethylpentene (PMP) and connected to the measuring electrolyte via a second frit. A usual alternative to PMP is a borosilicate glass body; both materials offer remarkable corrosion resistance. A full separation from the electrolyte can not be achieved, thus, the outer solution will become acidic and the salt will dissolve after extended use. As a result, the outer solution has to be exchanged by fresh solution once the nominal potential of the electrode begins to deviate (as calibrated against the master reference electrode, discussed below).

The manufacturer provides a value of $E_{\mathrm{AgCl}} = 198\,\mathrm{mV_{SHE}}$ at a temperature of 25 °C. The actual laboratory temperature has been around 23 °C. The experimental linear temperature coefficient is about $-1\,\frac{\mathrm{mV}}{^\circ\mathrm{C}}$ in the saturated case.[58] This is more than expected by Eq. 31, because the temperature-dependent concentration change of a saturated solution is not included besides other real-experiment influences. All measurements in this thesis are reported versus RHE by using the following conversion (at pH = 0.1):

$$E_{\mathrm{RHE}}^{\mathrm{measured}} = E_{\mathrm{AgCl}}^{\mathrm{measured}} + \left(E_{\mathrm{AgCl}}^{\circ} + (-2\,^\circ\mathrm{C})(-1\,\frac{\mathrm{mV}}{^\circ\mathrm{C}}) \right) + \frac{\ln(10)\,RT}{F}\mathrm{pH} + \Delta_{\mathrm{AgCl}}^{\mathrm{master}} \quad (32)$$

$$\approx E_{\mathrm{AgCl}}^{\mathrm{measured}} + 205.9\,\mathrm{mV} + \Delta_{\mathrm{AgCl}}^{\mathrm{master}} \quad (33)$$

$E_{\mathrm{AgCl}}^{\mathrm{measured}}$ is a potential measured against the RE, while $E_{\mathrm{AgCl}}^{\circ}$ is the standard potential of the governing reaction – the value provided by the manufacturer is used here. During the measurements, one electrode of the same type has been kept within its clean storage solution of the filling electrolyte: saturated KCl solution. It can be assumed that this electrode keeps its potential over an extended time period. Before and after every use of another electrode, the offset Δ is determined by measuring the voltage versus the master reference. Δ usually stayed within $\pm 1\,\mathrm{mV}$ during an experiment. Having discussed these influences on the electrode potential, a realistic systematic error of $\pm 3\,\mathrm{mV}$ can be realized – allowing for maximum Δ and 2 °C of laboratory temperature variation.

After becoming aware of the fact that leaking chloride ions interfere with the measurements, another RE, which does not rely on the chloride ion, has been used. This is the mercury/mercurous sulfate electrode ($HgSO_4$) depicted in Fig. 6d). The chloride ion makes the chlorine evolution reaction (CER) possible. We know from section 1.1 that RuO_2 is used on the industrial scale to electrochemically produce chlorine. The $HgSO_4$ RE is built in the same way as its AgCl counterpart, except for the governing equation being:

$$\mathrm{HgSO_{4(s)}} + 2\,\mathrm{e^-} \rightleftharpoons \mathrm{Hg_{(l)}} + \mathrm{SO_4^{2-}}. \quad (34)$$

As visible in Fig. 6d), the electrochemical process is realized through liquid mercury that is in contact with (yellowish) $HgSO_4$. Hg is contacted by a Pt wire and the saturated salt solution is potassium sulphate (K_2SO_4) in this case.[59]

Rather than trying to estimate the RE's potential versus RHE, it is more important

to guarantee the comparability to the AgCl reference system. To straighten this out, all measurements of this work are comparable among themselves as they are calibrated by means of a master reference. Comparability to literature is ensured by the estimation of the master electrode's potential given in Eq. 33.

Comparability to the AgCl master reference scale is established by measuring the voltage drop δ of a fresh $HgSO_4$ electrode – ensured by checking against the $HgSO_4$ master reference – versus a fresh AgCl electrode within the actual electrolyte (1 M H_2SO_4). It is subjected to similar systematic errors as the AgCl reference system, so the uncertainty of the actual voltage measurement is negligible. As a result, the scale is calibrated by:

$$E_{\mathrm{RHE}}^{\mathrm{measured}} = E_{\mathrm{HgSO_4}}^{\mathrm{measured}} + E_{\mathrm{AgCl}}^{T,\mathrm{pH}} + \delta + \Delta_{\mathrm{HgSO_4}}^{\mathrm{master}} \tag{35}$$

$$= E_{\mathrm{HgSO_4}}^{\mathrm{measured}} + 205.9\,\mathrm{mV} + 495\,\mathrm{mV} + \Delta_{\mathrm{H_2SO_4}}^{\mathrm{master}}. \tag{36}$$

The last type of RE, which has been in application to reduce the chloride ion contamination, is the gel-electrode. It is built after the AgCl-principle with the specialty that the salt solution is solidified to a gel of e.g. agar. This gel still offers ionic conductivity, but decreases the ion mobility, thus lowering the chloride ion leak rate.

2.2.3 Liquid junction potentials

A junction between two liquids of different concentrations results in an additional ohmic drop, which disturbs the measurement. Ions diffuse from higher to lower concentration at rates proportional to their transference number. This results in a potential difference if anions and cations have different transference numbers. Imagining a liquid junction, e.g., a glass frit, between HCl and pure water, the H^+ would diffuse faster through the junction than the Cl^--ions. Already a voltage emerges between the protons, which leave the chloride behind. As this process is partly counteracted by the attraction of the ions among themselves, a steady-state potential will establish. Nevertheless, this steady state would require the concentration of the second compartment to stay constant, which obviously will not be the case for long.[33]

Reducing the liquid junction potential (LJP) induced by the RE can be achieved by choosing salts with ions of similar transference numbers, hence less charge separation will occur.[59] Potassium chloride (KCl), which is used in the AgCl electrode, is a typical example as K^+ and Cl^- fulfill the requirement of similar transference numbers. Furthermore high concentrations are chosen to make the outwards flux as dominant as possible compared to the inwards flux, which consists of H^+ and HSO_4^- in the present case.[35]

The latter discussion illustrates an intrinsic problem with salt bridges. A salt bridge consists of an ionic solution, typically a salt solution, which is contained within two liquid junctions and used to establish ionic conductivity between two liquids without mixing them. These are used in the present work to allow for the use of standard AgCl-type electrodes while addressing the problem of chloride ion leakage. Placing the RE into an additional fritted compartment filled with saturated K_2SO_4 reduces the chloride leakage into the electrolyte considerably. Unfortunately, using this setup, which is shown in Fig. 7a), results in a LJP of about 30 mV. A measurement in 1 M H_2SO_4 versus a non-salt bridge RE (see Fig. 7b)) shows that the potential drops about 20 mV over three days. After an approximate linear behavior in the beginning, a drop occurs at an unpredictable time. Therefore, measurements utilizing a salt bridge are can work, but

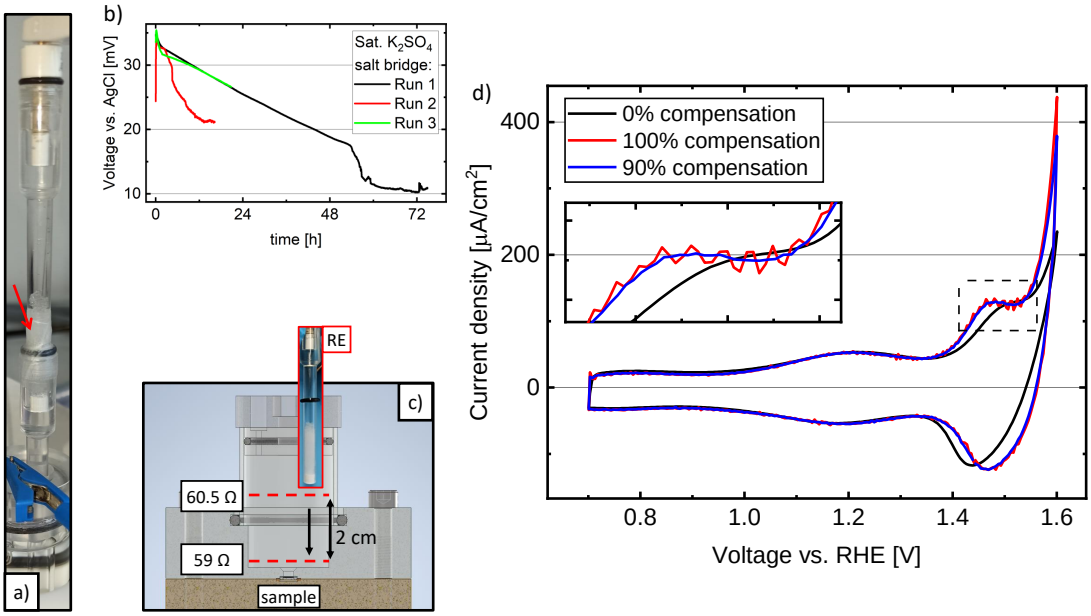

Fig. 7: a) Double junction reference electrode (RE) utilizing a K_2SO_4 (sat.) salt bridge. b) Potential drop of salt bridge RE (as shown in a)) for three consecutive measurements (fresh salt solution refilled) versus a non-bridged AgCl electrode in 1 M H_2SO_4. c) Estimation of the electrolyte's resistance contribution by measuring the total series resistance by electrochemical impedance spectroscopy (EIS) at the top and bottom of the cell. The electrolyte is well conductive. d) Cyclic voltammetry (CV) of RuO_2(110) in 1 M H_2SO_4 at 400 mV s^{-1} scan rate. By adding a series resistor the total resistance is increased to $R_s = (1398 \pm 1)\,\Omega$ to enhance the effect of the compensation setting.

have to be equipped with an appropriate systematic error for quantitative comparisons of absolute potentials. E.g., the peak width and area from a transition within a cyclic voltammogram are basically not affected as the drop is much slower than the timescale of a typical CV experiment (minutes). Care has to be taken with the absolute position of a peak. However, alternative RE like the $HgSO_4$ or the AgCl-gel electrode do not exhibit this problem.

2.2.4 Ohmic drop and its correction

In contrast to LJPs, there are two further types of ohmic drop which can be controlled in a rather simple manner. Fig. 7c) shows the an illustrative sketch of the electrochemical cell's series resistance component, while decreasing the WE-RE-distance from the highest to the lowest position directly next to the WE. The resistance merely drops from $(60.5 \pm 0.1)\,\Omega$ to $(59.0 \pm 0.1)\,\Omega$. Hence, there is a contribution from the electrolyte, even though it is a minor one. This is in line with the expected high conductivity of the 1 M H_2SO_4 compared to more diluted electrolytes. The main contribution has to stem from sample properties and the electric contact to the sample.

These ohmic resistances will cause a defined voltage drop proportional to the cell current. Therefore, not all of the applied voltage will actually drop over the WE - electrolyte interface. In principle there are two methods to account for this: The simplest way would be ignoring the problem at first and correcting the apparent voltages afterwards according to $E_{\text{actual}} = E_{\text{applied}} - IR$. This is less of a problem in slow, steady-state measurements, but as soon as scan rates are considered, a fixed rate sweep would result

in a slower actual scan rate the higher the cell current gets. E.g., during the measurement, of a rising current the ohmic drop increases with time while the applied scan rate stays constant.

The stated effect can be observed in Fig. 7d): The black 0%-compensation curve in shows a cyclic voltammogram of a single crystalline RuO_2(110)-surface. To pronounce the effects of ohmic drop – which are more severe at higher resistances and currents – a nominal 1.36 kΩ resistance is connected in series to the WE for this demonstration experiment. An actual measurement revealed an uncompensated series resistance of $R_s = (1398 \pm 1)\,\Omega$, which includes $(60 \pm 1)\,\Omega$ due to sample and electrolyte. Up to about 1.3 V_{RHE}, the expected ohmic shift is below 10 mV, and therefore, barely visible. As soon as the feature around 1.5 V_{RHE} is reached, the current rises and so does the ohmic drop. Actually, the mentioned unwanted scan rate change further promotes this effect, as the peak current of the feature also depends on the scan speed. On the reverse scan the shift direction changes in line with the sign of the current.

There is the possibility to actively correct for ohmic drop by a software feature of the potentiostat during the measurement. This is the compromise used throughout this thesis. The aforementioned software based live compensation operates by a positive feedback loop, which continuously adjusts the applied voltage by the value predicted on the basis of the simultaneously measured current.[60] Attempting to compensate for 100% of the measured series resistance can lead to an overcompensating, and thus, oscillating control loop. This can be either the case if the actual cell resistance decreases during the measurement, or, in regions of quick current variations. Usually the cell's series resistance stays constant or increases, which does not lead to control instabilities. The red 100%-compensation curve in Fig. 7d) shows clear oscillations at the right pair of peaks.

A curve recorded with an heuristically optimized compensation value of 90% is shown in blue in Fig. 7d). For this specific system it appears to be the best value. It can be found by decreasing stepwise from 100% until no more artifacts are present.

2.3 The electrode-electrolyte interface

2.3.1 The electrical double layer

As soon as an electrode faces an electrolyte, it will interact with it. In the following, the three basic concepts describing the interface will be examined. Fig. 8a) guides the reader by illustrating a positively charged electrode surrounded by an aqueous electrolyte. Anions and cations are surrounded by hydration shells. Starting from the left, the simplest concept, which explains how the potential at the electrode drops to its solution value, is the Helmholtz model. There are two planes: The inner Helmholtz plane (IHP) consists of a monolayer of adsorbed water dipoles and the outer Helmholtz plane (OHP) holds the larger anions. It is assumed that the whole voltage drop occurs linearly within this double layer, hence the name. The Helmholtz layer is roughly about 6 Å large, but this strongly depends on the size and charge of the participating ions.[61]

The Gouy-Chapman model adds another component, namely the diffusive layer. This can extend up to 10 nm.[61] The main idea is to incorporate two counteracting forces: Oppositely charged ions attracted by the electrode, and diffusion, which attempts to remix the solution by thermal energy. This situation is described by the well-known

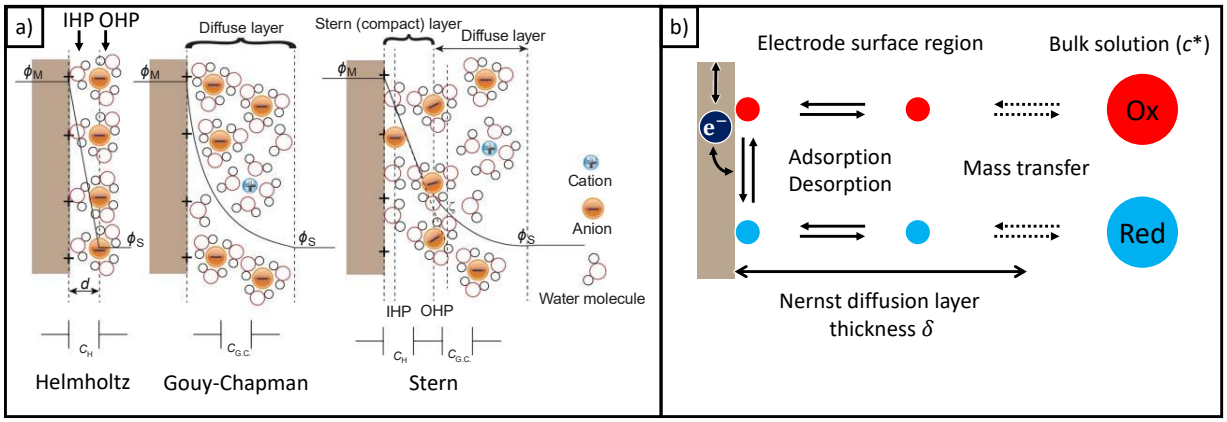

Fig. 8: a) The electrical double layer described by the Helmholtz (*left*), Gouy-Chapman (*mid*) and Stern model (*right*). The latter one sufficiently describes the situation by means of a fixed layer, consisting of the inner (IHP) and outer Helmholtz plane (OHP), and a diffusive (Gouy-Chapman) layer. (graphics from Eliaz *et al.*[61]) b) Illustration of an electrochemical electrode reaction: An oxidized (Ox) or reduced (Red) species (bulk concentration c^*) approaches the electrode surface region by diffusion, mitigation or convection. It adsorbs, exchanges charge with the electrode, and desorbs again. The distance from the electrode surface to the part of the solution that exhibits bulk concentration is known as Nernst diffusion layer thickness δ.

Poisson-Boltzmann equation and an exponential voltage drop like it is the case in a p-n-junction.

Stern then took the final step toward the development of a model that more accurately fits the observations. He realized that both of the former mechanisms are justified and combined the ideas of a fixed Helmholtz double layer and an additional diffusive layer. Both of these layers carry a specific capacitive charge, which can be added up as they behave like a series circuit.[61] Later, we will utilize the double-layer capacitance to determine the electrochemically active surface area (ECSA) of $RuO_2(110)$ (sec : *sec* : $CDLRuO2$).

2.3.2 Chemical reaction kinetics versus mass transport

Taking a closer look at the interface motivates us to discuss the area of tension between chemical reactions in the vicinity of the surface and mass transport within the bulk electrolyte. Fig. 8b) represents a cartoon of an electrochemical electrode reaction: Ox + $e^- \rightleftharpoons$ Red. At first, reactants approach the surface region by diffusion, mitigation or convection. To allow for electron transfer, reactants have to adsorb to the surface. If the reactant molecule does not penetrate the adsorbed water monolayer located in the IHP, it is called outer-sphere reaction. In this situation, the reaction tends to be less influenced by the actual electrode properties. Electrons basically tunnel through the IHP and reduce or oxidize the adsorbed molecule.[62]

This is in contrast to inner-sphere reactions. These depend strongly on the electrode's properties, as they include actual adsorption or bond formation with surface atoms. The adsorption of reaction intermediates during the OER is an important example. As surface adsorption is a typical mechanism included in catalytic processes, inner-sphere reactions are often called electrocatalytic reactions.[62] Usually, after the reaction, the products will desorb and mix with the bulk electrolyte again. Nevertheless,

there is an exception called electrodeposition. In this case the product will build up or crystallize at the electrode.

Next to diffusion, there are two other mechanisms (mitigation and convection) that facilitate mass transport within an electrochemical cell. It is illustrative to consider the Nernst-Planck equation[63], which accounts for all of them:

$$J(x) = \frac{\dot{n}}{A} = -\underbrace{D\frac{\partial c(x)}{\partial x}}_{\text{diffusion}} - \underbrace{\frac{zF}{RT}Dc(x)\frac{\partial \phi(x)}{\partial x}}_{\text{mitigation}} + \underbrace{c(x)u(x)}_{\text{convection}}. \tag{37}$$

Here, D is the diffusion constant, z is the charge of an ion, ϕ is the electric potential, u the fluid velocity and $c(x)$ is the concentration dependent on the distance x to the electrode of area A. In this equation, J is not the electric, but a particle current density, which is indicated by the change of particles per time $\dot{n}$. It becomes clear that the first two terms are driven by concentration and potential gradients respectively, i.e an electric field. Positive gradients transport positive particles towards the electrode, therefore the negative sign. Convection corresponds to a movement of the electrolyte taking the ions along.

In general, diffusion dominates mitigation as the main reactant supplier for electrode reactions. As a result, the experimental tuning parameter is convection if increased mass transport is favored. This can be done by introducing an electrolyte flow towards the electrode. Mitigation can be thought of as the main transport mechanism in the bulk solution, where concentration gradients are small, acting like a wire which connects the electrode surface regions.[33] Mitigation (i.e., actual movement of ions in an electric field) is the only mechanism left in the bulk solution, because diffusion contributes negligibly.

Tuning mass transport experimentally becomes important when reactions such as oxygen reduction are investigated. As soon as the kinetic current at high overpotential is faster than the electrolyte is able to supply oxygen reactant, the reaction will become mass transport limited.[13] In simple terms: the reaction rate is so high that basically every oxygen molecule reaching the electrode surface gets instantly reduced and keeps the electrode waiting until fresh reactant arrives. In such a case, impinging a jet of reactants onto the electrode surface would increase the reactant concentration in the vicinity of the reactive surface.[64] To create a distinction to natural thermal convection, artificially increasing convective transport is named *forced convection*.

2.4 Principles of cyclic voltammetry

2.4.1 Digital staircase sweep and the voltage step

If no analogue ramp generator is used to produce the triangular voltage sweep for cyclic voltammetry, a linear sweep is performed by approximating it with a digital staircase as depicted in Fig. 9a). Every small voltage step causes a typical current response. It consists of a fast and a slow decaying component, as it would also be the case for a comparably large voltage step (see Fig. 9b). 'Fast' refers to an exponential current decay caused by charging the electrical double layer, which behaves like a capacitor.[63]

The slower decay is usually present in the mass transport limited case.[35] It can be described by solving Fick's second law for an infinite planar electrode with the following

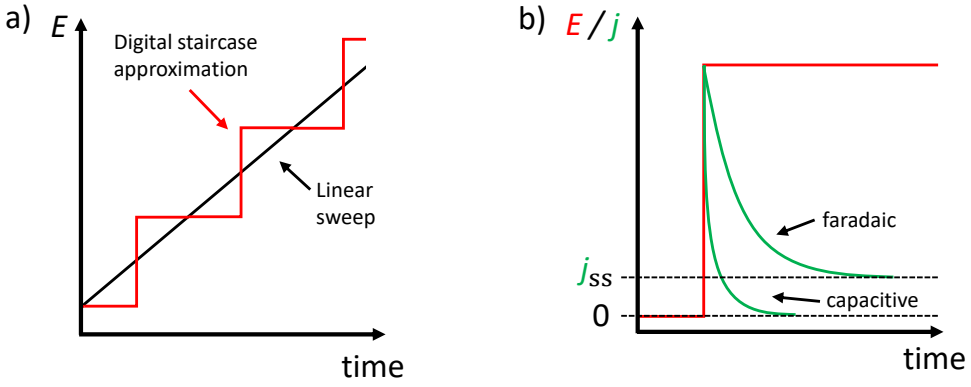

Fig. 9: a) Approximation of a linear sweep by a digital staircase. b) Typical current response to a voltage step of a solution species electrode reaction. Charging of the electrical double layer causes the exponentially decaying capacitive currents. The faradaic current exhibits a polynomial decay according to the Cottrell equation (Eq. 38). Natural convection causes a limiting steady state current density j_{ss}. (Eq. 39)

boundary conditions:[35] At time zero, the concentration equals the the bulk concentration c^* at all distances to the electrode x. In case of a mass transport limited reaction it is reasonable to assume zero concentration at the surface $x = 0$ for $t > 0$. Furthermore, the concentration at infinite distance equals the bulk concentration $\forall t$. This results in the Cottrell equation[65]

$$j(t) = nFc^* \sqrt{\frac{D}{\pi t}}, \tag{38}$$

which describes the time dependent current density after a voltage step. n is the number of charges transferred during the electrode reaction. At time zero, the current diverges as the concentration near the electrode is high, as well as the reaction rate. Over time the reactants will deplete. Therefore, the distance δ between the electrode and the electrolyte still exhibiting bulk concentration, as shown in Fig. 8b), increases. This region in front of the surface is also known as Nernst diffusion layer.[35]

According to the Cottrell equation, the current would be expected to decay to zero after infinite time. This situation can be imagined as extending the Nernst diffusion layer all the way to infinity. Now the spatial concentration profile resembles a line connecting zero concentration at the electrode with a finite bulk value at infinity – so the expected, concentration gradient driven, current will approach zero. Intuitively this is not realistic: Due to natural thermal convection there will always be a finite diffusion layer thickness determined by the experimental conditions. As a result the steady state current can be approximated by Fick's first law[35]:

$$j_{ss} = nFD\frac{c^*}{\delta}. \tag{39}$$

The fraction reflects the linear diffusion gradient (which is the actual limiting case) connecting zero concentration to the bulk concentration c^* at distance δ.

The exponential and polynomial decay behavior of the surface and solution related processes allows for an effective exclusion of the faster charging currents. This is done by sampling the current, after the exponential process has mostly decayed, at the end

of each step. In situations where the experimentalist is solely interested in the solution redox processes, this can be a valuable strategy. Furthermore, this makes sense if fast surface reactions are not of interest, but rather the OER activity, which is (at least expected to be) a process occurring constantly over a prolonged time.

2.4.2 Probing fast surface reactions

As already addressed in subsection 2.1.2, the flat regions of a cyclic voltammogram correspond to charging and discharging of the electrical double layer. In addition, the hydrogen adsorption region (H_{ads}) shows hydrogen adsorption and desorption peaks. The following discussion focuses on the expected peak shape and underlying theory as originally developed by Laviron.[66–68] Hydrogen adsorption at Pt is a textbook example, furthermore, H adsorption at RuO_2(110) will be discussed within the same framework. Surface adsorption processes are basically as fast as the double-layer charging and can be described in terms of an additional capacitive component. This makes sense, because $H^+_{(aq)}$ is readily available near the electrode and can be transferred via adsorbed (in this case not chemically bound) water. Also, just a single electron transfer is needed to create a surface bond hydrogen. In case of the formation of only a single monolayer, mass transport does not play a role either. Capacitive charge generated by a fast chemical – i.e faradaic – process is known as pseudocapacitive charge (concept of a supercapacitor).

A simple, yet effective, starting point is the Langmuir adsorption isotherm. The preceding discussion is based on the textbooks of Compton[35] and Eliaz[61], and on Laviron's[68] original work. An adsorption isotherm relates a bulk solution species concentration, e.g. $[H^+]$, to a relative adsorbent coverage θ. The hydrogen adsorption on Pt will serve as an example:

$$H_3O^+_{(aq)} + e^- + Pt^* \rightleftharpoons Pt{-}H + H_2O. \tag{40}$$

The Langmuir adsorption isotherm of the relative surface coverage θ is[52]

$$\frac{\theta}{1-\theta} = [H^+]\,\tilde{K}, \quad \tilde{K} = \exp\left[\frac{-F}{RT}(E - E^\circ_{\mathrm{ads}})\right]. \tag{41}$$

$\tilde{K}$ is the chemical equilibrium constant of Eq. 40. Note that the concentration is again measured relative to the standard concentration of 1 mol dm^{-3}. There are two important remarks, which have to be considered by writing a Langmuir isotherm this way. First, the chemical equilibrium constant $\tilde{K}$ differs from the usual definition, as it already accounts for the shift of electrochemical potential due to an electrical potential E. Second, the standard potential E°_{ads} additionally accounts for the energy gain or loss due to adsorption, which differs from a reaction that solely includes aqueous species. The goal of this derivation is to get an idea of the general potential dependent peak-shape induced by changes of the potential rather than the pH, therefore the bulk proton concentration will be set to standard conditions, $[H^+] = 1$, for simplicity.

The assumptions of the Langmuir isotherm are: An instant Nernstian equilibrium, which relates the relative coverage concentrations $\frac{\theta}{1-\theta}$ to the potential E (see Eq. 26) by predicting the change of the equilibrium constant for all potentials; A maximum coverage of one monolayer ($\theta = 1$); A perfectly homogeneous surface with all sites

having equal and coverage-independent adsorption free energies; The adsorbed species is much smaller than an active site to exclude lateral interactions.

Utilizing the adsorption isotherm enables the calculation of a potential dependent pseudocapacitance $C(E)$. This is of interest, because the current density at a certain potential can be expressed by

$$j(E) = \frac{\mathrm{d}q(\theta)}{\mathrm{d}t} = q_{\mathrm{ML}} \frac{\mathrm{d}\theta(E)}{\mathrm{d}t} = q_{\mathrm{ML}} \frac{\partial\theta(E)}{\partial E} \frac{\partial E}{\partial t} \tag{42}$$

$$= C(E) \cdot \nu \tag{43}$$

with the charge per unit area q, expressed by the fraction θ of a full monolayer q_{ML}, and the scan rate ν.

Rearranging Eq. 41 allows the evaluation of the capacitance and therefore the current density according to Eq. 43:

$$j(E) = \frac{q_{\mathrm{ML}} F}{RT} \cdot \nu \cdot \frac{\exp\left[\frac{F}{RT}(E - E^{\circ}_{\mathrm{ads}})\right]}{\left\{1 + \exp\left[\frac{F}{RT}(E - E^{\circ}_{\mathrm{ads}}\right]\right\}^2}. \tag{44}$$

This results in the peak shape depicted in Fig. 10 for the non-interacting i.e. Langmurian case. The adsorption peak, also known as surface redox peak, scales linearly with the scan rate. This scaling is obvious, as always the same charge of one monolayer is transferred during the redox transition. With doubled scan rate, double the current is needed to transfer the same charge within half the time. The FWHM of the non-interacting peak equals $3.53\frac{RT}{nF} = \frac{90.6\,\mathrm{mV}}{n}$, with n being the number of transferred electrons of the redox process.[35]

On this basis, Laviron further developed the theory by including a lateral interaction parameter G. Basically one follows the same steps as before, but with a Frumkin-like isotherm[52] as starting point:[61,67]

$$\frac{\theta}{1-\theta} = \exp\left[\frac{-F}{RT}(E - E^{\circ}_{\mathrm{ads}})\right] \exp\left[-gf(\theta)\right], \tag{45}$$

where g acts as interaction parameter, which adapts the adsorption free energy as a linear function $f(\theta)$ of the fractional coverage θ.

In Laviron's case, the isotherm[67] carries a few more factors, but is conceptionally comparable. Lateral interactions are described by

$$G = (\epsilon_{\mathrm{O}} + \epsilon_{\mathrm{R}}) - 2\epsilon_{\mathrm{OR}} \tag{46}$$

with ϵ describing lateral interactions between oxidized and reduced species among themselves, as well as interactions between both species. So the concept is already generalized compared to the simple hydrogen adsorption example discussed at the beginning of the section.

The interaction parameter G and the resulting peak shapes shown in Fig. 10 can be interpreted intuitively. They have been calculated numerically after Laviron's model[67], as there is no analytical solution in the interacting case. The interaction parameter compares the attraction among the same species to the attraction between different species.

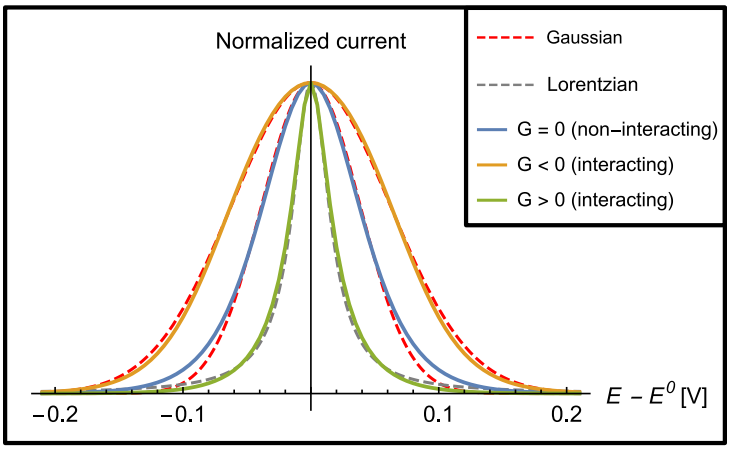

Fig. 10: Comparison of the non-interacting Langmuir surface redox reaction peak shapes to the interacting (Frumkin) case. A Lorentzian approximates the (numerically calculated) peak shape well for interaction parameters $G > 0$. A Gaussian approximates the other ($G < 0$) case.

Assume $G > 0$, both species tend to be separated. $a > 0$ corresponds to an attraction, and therefore, the separated case ($\epsilon_O + \epsilon_R$) outweighs the mixed phase $2\epsilon_{OR}$ energetically. The FWHM sharpens according to the following linear approximation[69] of the numerically calculated relation:

$$\mathrm{FWHM} = \frac{90.53\,\mathrm{mV} - 55.51\,\mathrm{mV}\ \mu\theta_{\mathrm{tot}}G}{n}. \tag{47}$$

θ_{tot} is the maximum fractional coverage and μ the number of water molecules replaced by one surface bound molecule. The approximation holds well for $\mu\theta_{\mathrm{tot}}G < 1$. The transition region between O and R, i.e. the peak, is narrowed to minimize the potential range of the mixed phase. Respectively the peak broadens to maximize the mixed phase of oxidized and reduced species in the $G < 0$ case.

This reveals the importance of the FWHM of a surface redox feature. To facilitate an automatic peak fitting procedure for the interacting case, analytical approximations to Laviron's model are considered. Fig. 10 shows numerical solutions to the discussed cases and approximations by Gaussians and Lorentzians with matching FWHM. As the aim is to compare the peak shapes, all curves are normalized, otherwise they would sharpen and broaden with constant area. It appears that a Lorentzian fits reasonably well in the repulsive $G > 0$ case, and a Gaussian covers the attractive $G \leq 0$ regime.

Hydrogen adsorption at the RuO_2(110) surface solely shows FWHMs well above 90 mV ($G < 0$), hence, assuming a one-electron ($n = 1$) process, a Gaussian can be used to extract width, height and position of all observed peaks.

At this point, it is appropriate to note that lateral interactions are not the only conceivable mechanism which influences the peak shape.[69] Nevertheless, the usual starting point of proposed corrections is always the non-interacting Langmuir surface redox peak.

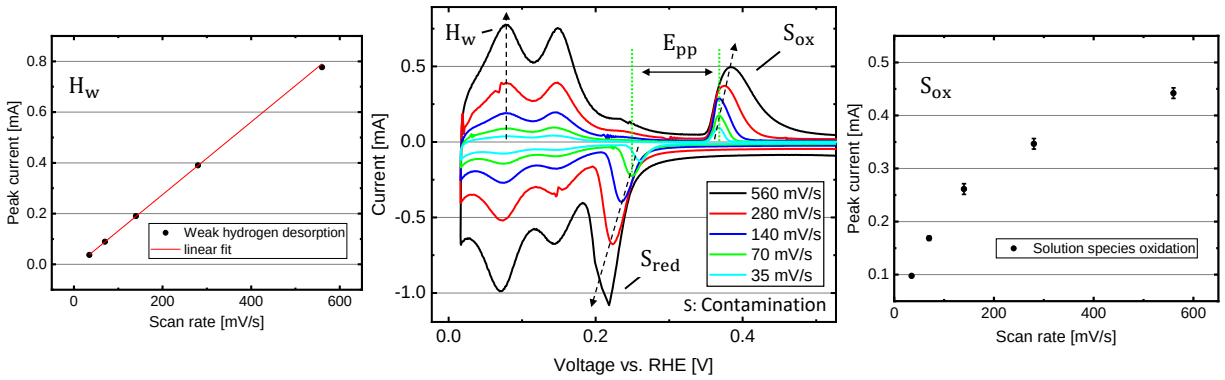

Fig. 11: Cyclic voltammograms at different scan rates of a Pt wire in 1 M H_2SO_4. The hydrogen adsorption peaks are visible as well as a peak pair caused by a contamination ($S_{ox/red}$). *left:* Scan rate dependence of the peak current of the weak hydrogen desorption feature (H_w). It scales linear as predicted by Eq. 43. *right:* Scan rate dependence of the peak current of the solution species oxidation feature (S_{ox}). It scales approximately with the square root of the scan rate.

2.4.3 Surface versus solution redox processes

Fig. 11 shows a CV experiment of a platinum surface at different scan rates in sulphuric acid. Two types of peak pairs can be easily distinguished due to their peak-to-peak separation and scan rate dependence. The scan rates range from $35\,\mathrm{mV\,s^{-1}}$ to $560\,\mathrm{mV\,s^{-1}}$ and are doubled in every intermediate step.

The amplitude of the hydrogen adsorption region ($H_{ads/des}$) on the left scales linearly with the scan rate ($I_p \propto \nu$) according to the presented theory of a surface redox peak (Eq. 44). Positive and negative peaks have the same peak potential for all scan speeds, as the reaction proceeds instantly compared to the voltage scan rate.

The right process ($S_{ox/red}$) differs in all mentioned aspects. The right pair's peak potentials are clearly separated by E_{pp} as shown in Fig. 11. Starting at slow scan rates the peak amplitudes are higher than the ones of the surface redox peak. With increasing scan rate, the surface redox peak is able to overtake, therefore the peak current to scan rate dependence is expected to have an exponent x less than one. ($I_p \propto \nu^x$) Furthermore, the peak-to-peak separation increases with scan rate.

The latter behavior is expected for solution, or outer-shell, redox processes, where no species are adsorbed within the IHP. At first, this results in a rising current caused by an activation-controlled, i.e. Butler-Volmer regime, process. As the process proceeds, the surface concentration depletes until a mass-transport limited regime is reached. After the peak, a current which decays according to the Cottrell equation (see Eq. 38) can be observed. For an ideal solution species process the peak current scales with the square-root of the scan rate ($I_p \propto \sqrt{\nu}$).[35]

Feature S in Fig. 11 is possibly caused by a contamination of the electrolyte with a metal ion. This resembles a mixed solution and adsorbed phase process, which bears further complexity. Even though, qualitatively, it shows some typical solution phase properties, there are clear indicators that this is not exactly true. The peak to peak separation exceeds the expected 57 mV for a pure solution phase process[35] in its reversible limit, i.e., small scan rate compared to the chemical rate constant. Above a certain scan rate, the peak separation is expected to increase with $\ln(\nu)$[35]; that is actually the case. Therefore, it could only be a highly irreversible (slow chemical rate constant) process as

this would cause a large enough peak separation and still explain the increasing decaying diffusional tails at higher scan rates.[70]

Furthermore, nucleation processes can influence an adsorption process if clusters are formed. As a result, after surpassing the energy barrier to form nucleation sites at platinum, the reaction could drastically speed up by adsorption to nucleation clusters instead of platinum sites. A large peak to peak separation would also be reasonable here.[71] For completeness a surface confined redox reaction similar to the hydrogen adsorption is also able to reach a irreversible (large peak separation) limit.[72,73] However, such a process does not explain the decaying tails.

Following the electrodeposition interpretation, the left reduction peak would correspond to metal ion deposition, while the oxidation feature on the right would indicate stripping of the adsorbate. Nevertheless, it has to be taken into account that the symmetry is atypical for a stripping feature. We will see this when discussion the stripping of silver ions at RuO_2 (Fig. 19c)) in the next chapter.

2.5 Electrochemical impedance spectroscopy

Next to direct current (DC), pulsed, or sweeped measurements, the second important concept are alternating current (AC) voltage measurements. Sine waves of small amplitude are applied to observe the frequency dependent response.

2.5.1 Impedance measurements

The complex impedance is defined as:

$$Z = \frac{U(t)}{I(t)} = \frac{|U|\ \mathrm{e}^{i(\omega t+\phi_U)}}{|I|\ \mathrm{e}^{i(\omega t+\phi_I)}} = \frac{|U|}{|I|}\,\mathrm{e}^{i(\phi_U-\phi_I)}. \tag{48}$$

Electrochemical impedance spectroscopy (EIS) excites the system with a sinusoidal waveform of different frequencies $f = {}^{\omega}/_{(2\pi)}$, which in turn will respond with a frequency dependent phase ϕ shift and current amplitude:

$$Z(\omega) = \big|Z(\omega)\big|\ \mathrm{e}^{i\phi(\omega)}. \tag{49}$$

The complex impedance is commonly represented by a Nyquist plot, which is a trace in the complex plane showing all frequency responses at once. Usually, the imaginary axis is inverted, when describing electrochemical systems, because inductive, i.e., positive imaginary, components are rare.[74]

To gain information by EIS, an equivalent circuit model has to be conceived and fitted to the frequency dependent impedance response of the electrochemical cell. This is done by the complex non-linear least squares fitting (CNLS) procedure of the software provided by the manufacturer of the potentiostat. It utilizes a simplex fitting algorithm.

Prerequisites of meaningful impedance data are: linearity, stability and causality. Linearity is ensured by choosing a small enough excitation amplitude to avoid non-linear current responses. Basically, this is the idea of a first-order Taylor approximation around a working point chosen from a CV curve. Caution has to be taken by optimizing the amplitude, as the signal-to-noise ratio becomes an increasing problem the lower the

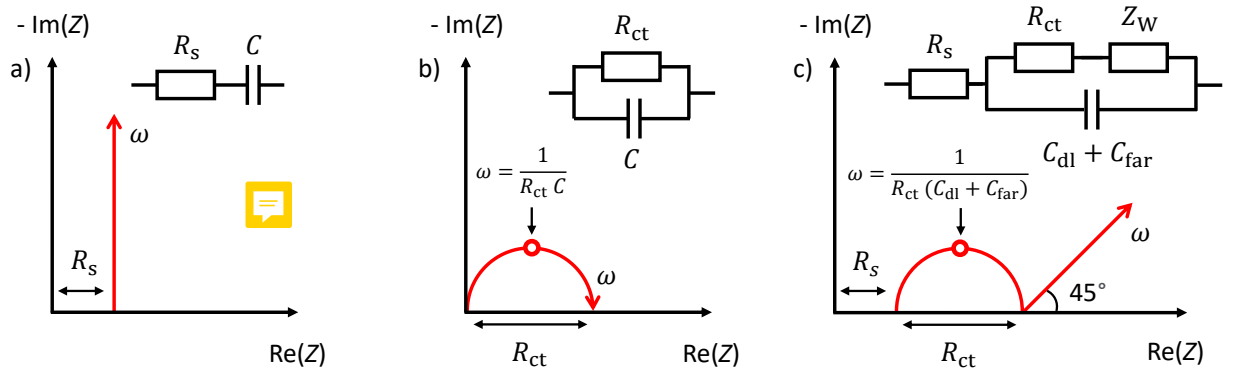

Fig. 12: Nyquist plots of the frequency ω dependent complex impedance Z: RC series, RC parallel and Randles circuit. The Randles circuit approximates an electrochemical cell including diffusional mass transport through the Warburg impedance Z_W.

amplitude is set. Stability demands a time-independent system that does not change during the EIS experiment. Causality requires the Kramers-Kronig relation to hold.[74]

The prerequisites can be checked by actually measuring e.g. the relative non-linear response of a system, superimposed dc-current drifts or performing Kramers-Kronig transformations. These tests were performed to optimize the EIS settings for a certain system.[74]

2.5.2 Randles equivalent circuit model

A common model, which fits 'simple' electrochemical systems, is the Randles equivalent circuit. All components feature an intuition. The full circuit model including its expected Nyquist plot is shown in Fig. 12c). Combined contact and electrolyte resistance are represented by the series resistance R_s. The elements that contribute to it will be discussed in the following chapter (section 3.3).

A parallel circuit is chosen to model processes that occur simultaneously. The charge transfer resistance R_{ct} accounts for kinetic electrode reactions described e.g. by the Butler-Volmer equation (see Eq. 8). For sufficiently small perturbations this results in a linear, i.e. ohmic response. The Warburg impedance Z_W represents semi-infinite linear diffusion and belongs to the group of constant phase elements (CPE). It is defined as:

$$Z_W = \frac{A}{\sqrt{\omega}}\, e^{-i\frac{\pi}{4}}, \quad A \propto \frac{1}{\sqrt{D}}. \tag{50}$$

The corresponding Nyquist plot features a constant phase of 45°. This circuit element is situated in series to R_{ct}, because reactants of electrode reactions have to be supplied by diffusional mass transport first. That is why the prefactor A depends on the diffusion constant D.

Capacitive components are located in parallel. Next to chemical reactions the electrical double layer is continuously charged and discharged (C_{DL}). In addition, pseudocapacitive charge (C_{far}) is stored at the surface as described in subsection 2.4.2. Both capacitances occur parallel and presumably independent of each other. Consequently,

they add up $C_{tot} = C_{DL} + C_{far}$ as they can be thought of as parallel capacitive components.

Fig. 12c) shows the typical Nyquist response of a Randles circuit. In can be explained in three simple steps. The Nyquist plot of a single capacitor is a straight on top of the imaginary axis. The addition of a series resistor shifts the curve to positive real values by R (Fig. 12a)). An RC-parallel circuit resembles a capacitor in the high frequency limit and ends with pure resistive behavior at the low frequency end ((Fig. 12b))), as the capacitor breaks the circuit in the DC limit. As a result of that, a circle with radius R emerges in the Nyquist plot.

Combining all elements in Fig. 12c), results in a circle, shifted by R_s, passing through a maximum at $\omega = \frac{1}{R_{ct}(C_{DL}+C_{far})}$ and touching the real axis at $R_s + R_{ct}$. In the low frequency limit, Warburg diffusion appears as a straight with a constant 45° angle to the real axis. Depending on the DC polarization point of the EIS measurement different components can appear in different markedness.

3 Electrochemical Cell Development: Thin Films for Catalysis

This chapter will focus on a crucial part of this project: designing and optimizing an electrochemical cell that is capable of performing reliable measurements of thin films grown on top of insulating substrates. The beginning will focus on the technical aspects of the tuning process while the posterior part describes the identification and elimination of impurities, namely: dissolved oxygen, chloride ions and silver ions.

3.1 Final electrochemical setup

The final cell is shown in Fig. 13a). Two structurally identical cells were used – one at each channel of the potentiostat – to double the characterization efficiency by means of the developed standard protocol (section 5.2).

A gas washing bottle fulfilled two purposes: Its main purpose is to humidify the nitrogen gas that was constantly supplied to blanket the electrolyte surface. This is important to counteract the electrolyte evaporation caused by dry nitrogen. The importance of generating an inert atmosphere will be demonstrated in the next section. The actual washing capabilities regarding dust removal are another, yet minor, advantage. The gas inlet is controlled by a magnetic proportional valve from Bürkert, which is operated via PC.

The red WE lead is connected to the copper contact, which contacts the sample surface, at the bottom of the cell. The cell body is filled up with electrolyte. The top cap offers four connections. A gas inlet and outlet, which can be sealed by o-rings. The idea of the outlet port is to offer the possibility of complete gas tightness by connecting another gas bubbler to it. Nevertheless, it appeared that the constant nitrogen outflow condition has already been sufficient.

The other two ports are used for the Pt CE and the $HgSO_4$ RE. The CE is held in place by a contact pin and the RE is fixed and sealed by an FPM o-ring. The RE is always inserted nearly to the bottom of the cell in order to decrease the electrolyte resistance. Its position is intentionally chosen off-center to avoid a blocking of the frit by bubbles rising from the centered sample below.

The CE is spooled to keep it within a confined area with a certain distance to the WE. It approximately fulfills the condition of being 'remote', which means that a further increase of the distance to the WE would not result in a significant change (>5 %) of the cell's series resistance anymore.[75] A further goal is to avoid uneven current distribution on the WE, which can be caused by unequal distances between different points at the WE surface and the CE. Choosing symmetric configurations[33] and moving the CE away from the WE counteracts that.

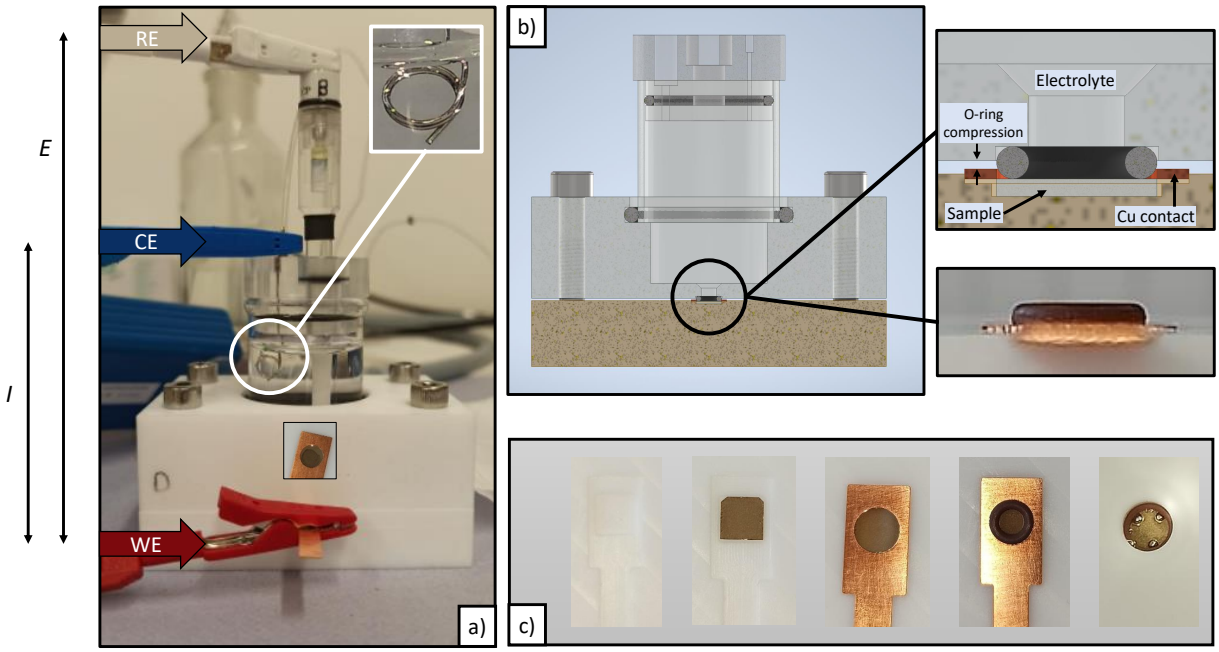

Fig. 13: a) Final setup showing the electrochemical cell used for the experiments. The inset shows the platinum counter electrode (CE). b) Cross-sectional view of the CAD model of the cell. The connection to the sample surface, which is sealed from the electrolyte by an o-ring, is magnified. Underneath, a real picture of the o-ring and the copper contact within the bottom part of the cell is shown. c) Cartoon of the sample mounting process: The sample is placed in its indentation first and the copper contact is put on top. Then, the sealing o-ring is inserted and the cell is ready to be assembled.

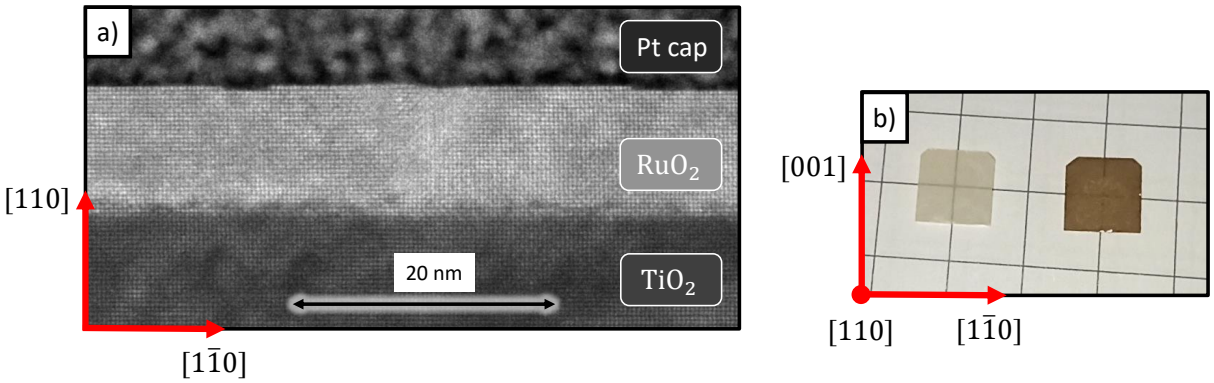

Fig. 14: a) Transmission electron microscopy (TEM) image of a RuO_2(110) thin film grown by pulsed laser deposition (PLD) on a TiO_2(110) substrate. The surface shows monoatomic (1/2 unit cell) steps. Areas of blurry constant (middle of the image) are a common observation and could indicate disturbed growth. Furthermore, clear dislocations were observed by TEM (not shown). b) Picture of the transparent TiO_2 substrate and the RuO_2 thin film, which exhibits metallic shine.

The cross-sectional view of the cell within the CAD model, shown in Fig. 13b), reveals where the gaskets sit and how they work. The cap offers the possibility to add an o-ring around every inserted piece at all of the ports. The o-ring that seals the cap has its own indentation. The connection between glass tube and the PTFE cell body is realized by tightly fitting the glass into an outer sealed recess.

The interface between the cell body, the copper contact and the thin film sample is the key part of the cell. The magnified view of Fig. 13b) offers a closer look at this connection. The sample indentation is designed in a way that the sample sticks out as little as possible. As a result, the copper contact, which is pressed onto the sample by screwing the cell together, has less room to bend around the sample. This would cause the contact to leave the mid area of the surface. Nevertheless, the whole surface of the contact is pressed by the cell body, which keeps that effect small either way. The compression of the o-ring is defined by the distance between the bottom of the cell body and the top of the copper contact where the cell body is pressed onto. Therefore, the o-ring compression can be varied by making the indentation deeper or shallower. Below the magnified view, a real picture of the contact sitting in the bottom part of the cell is shown.

Fig. 13c) illustrates the sample mounting process. After some tuning, the sample indentation reached a size that just allowed the sample to fall in without extra help. The copper contact fits with a smooth clicking sound. Then, the o-ring is placed on top of the sample. As the indentation will help it find its exact position, this also can not be done incorrectly. Finally, the cell body is placed on top and the screws are tightened until a hard stop, which is reached when the PTFE parts touch each other at the short sides, occurs. Looking very closely from the long side, an intended extremely tiny slit is visible in the middle near the sample. This is a confirmation that the contact is actually pressed onto the sample, otherwise, the contact would have enough space to fully disappear in its indentation and the cell would close completely. The last picture shows the sample, sealed by the o-ring, within the assembled cell.

3.2 General considerations: Materials and requirements

At first, the boundary conditions of the anticipated setup will be outlined. Fig. 14a) shows a transmission electron microscopy (TEM) image of a typical good quality RuO_2(110) thin film. The surface exhibits monoatomic (1/2 unit cell) steps and larger atomically flat areas in between. Areas of blurry constant (like in the middle of Fig. 14a)) are a common observation and could indicate disturbed growth. Clear dislocations were also observed by TEM (not shown). Fig. 14b) shows a TiO_2(110) substrate on the left, on top of which the about 10 nm thick film is grown. The RuO_2 sample shown in Fig. 14b), grown by pulsed laser deposition (PLD), is clearly distinguishable by its metallic shine.

This raises the problem of the insulating substrate since the (only $5 \cdot 5\,mm^2$ large) sample has to be electrically contacted from the top while simultaneously allowing the acidic electrolyte to contact its surface. Therefore, the available space has to be used most efficiently. It is stressed that the acid should not contact anything but the sample surface under measurement, as the copper contact would readily corrode. On the other hand, the insulating substrate has advantages on the experimental side. It has been checked that the substrate is electrochemically inert by testing it within the same

setup used for the catalytically active RuO_2(110) samples. Consequently, holes in the film, whether they originate from corrosion during testing or through locally insufficient growth, do not interfere with the measurement.

The copper contact is made of Cu-DHP, as it is tendentially well moldable – in spite of the fact that this may not be too relevant on the length scales of the contact. The cell body is made of poly(tetrafluoroethylene) (PTFE) as it is one of the most chemically resistant polymeric materials under acidic environments. Corrosion of the cell itself could contaminate the experiment. Sometimes poly(ether ether ketone) (PEEK) is preferred as cell material for its better machinability.[76] This advantage is however compensated by slightly less corrosion resistance. All gaskets are made of a fluoroelastomer (FPM) o-rings, which offer the required trade-off between elasticity and corrosion resistance. Furthermore, the cell is composed of a borosilicate glass and a poly(methyl methacrylate) (PMMA) cap. The latter is chosen for its transparency and is not in direct contact with the electrolyte, nonetheless, PMMA is fairly corrosion resistant.

Beyond the pure functionality of this electrochemical cell, practical aspects are also considered. Since the setup is intended to be used for the characterization of a whole growth diagram of samples, it is designed to offer reproducible contact conditions for every sample, while still being as user friendly as possible.

3.3 Optimization of the thin film cell

Before summarizing the most important upgrades of the cell, four illustrative observations from the tuning process will be presented. They consider the compression of the o-ring, the contact's pressure on the sample, what contributes to the cell's series resistance and the influence of gas bubbles. The two key parameters are the compression of the o-ring and the pressure exerted on the sample by the copper contact. One guarantees leak-proof operation and the other one a small contact resistance.

To aid in empirically illustrating the effect of these parameters, a polycrystalline platinum plate (MaTecK, 99.9%) is used as a reference sample within the thin film cell. Fig. 15a) shows two voltammograms of the reference sample in 1 M H_2SO_4 at a scan rate of 100 mV s^{-1}. The red curve was recorded first and corresponds to an o-ring compression of 15% of its 1 mm cord thickness. The voltammogram is clearly asymmetric with additional weight at the top right and bottom left compared to the clean black curve. This indicates side reactions occurring next to the pure Pt chemistry possibly stemming from a leak. Consequently, the electrolyte would be able to corrode the copper contact. Taking a look at the sample and the contact plate after the experiment confirmed this hint. The sample, as well as the copper contact showed clear signs of corrosion as depicted in Fig. 15b).

This problem has been solved by increasing the o-ring compression to 25% by reducing the o-ring indentation by 0.1 mm. The black curve in Fig. 15a) shows the resulting clean Pt signal from the same sample at the same spot. A difference to the reference Pt curve shown in the last chapter in Fig. 5c) can be recognized. This is caused by the different chloride ion concentrations[77] in both cases and will get further attention later in this chapter (subsection 3.5.2).

Additionally, Fig. 15c) shows a CV experiment of copper (99.995 %) in diluted, 0.2 M H_2SO_4, electrolyte. Even at slightly diluted conditions (compared to the standard 1 M H_2SO_4) copper is readily dissolved into the electrolyte under anodic polarization.[78,79]

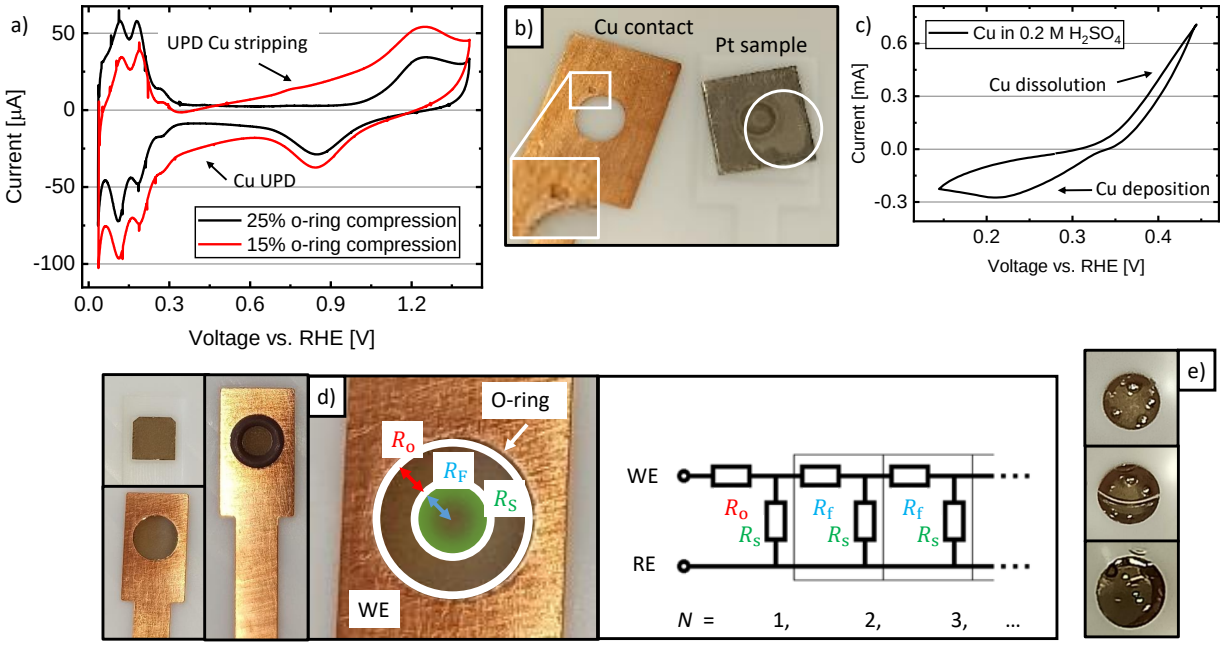

Fig. 15: a) Pt electrode measured at 100 mV s^{-1} in N_2-saturated 1 M H_2SO_4 within two different prototypes of the thin film cell. At nominal 15% o-ring compression the electrolyte is able to leak out and corrode the copper contact. This introduces additional Cu underpotential deposition (UPD) and stripping currents at Pt. The resulting signs of corrosion are depicted in b). c) Cyclic voltammogram of a Cu electrode recorded at 50 mV s^{-1} showing the dissolution and redeposition of copper ions in 0.2 M H_2SO_4. d) One dimensional resistance ladder model that motivates the expected current distribution on the sample (green) and contributions to the cell's series resistance. The working electrode (WE) lead is connected to the copper contact, which contacts the sample from the top. R_o is the pure thin film resistance underneath the o-ring (in some cases including contact resistance to the copper contact). R_F is the thin film resistance to the center and R_S is the total electrolyte resistance. An EIS measurement probes the voltage drop that occurs up to the reference electrode (RE) – even though, the current flows through the counter electrode (CE) (as discussed in subsection 2.1.4). N is the number of resistance ladder parts that is used to approximate the infinite continuum limit. e) A cartoon of a bubble blocking the WE during high anodic polarization over an extended time period.

This is the reaction (Eq. 9) we missed at the lemon battery as there were no dissolved copper ions present – and furthermore, no applied bias. The dissolution process is activation controlled and unlimited reactant is available through the Cu electrode. In contrast, the redeposition of Cu^{2+}(aq) ions shows a typical mass transport limited diffusional tail[78,79] after surpassing the peak current – this is described by the Cottrell equation Eq. 38. This is caused by the diffusion-limited supply of Cu^{2+}(aq) from the bulk solution.

However, this is distinct from the observation at the Pt electrode. The situation differs as the observed current in the CV experiment rather resembles a Cu UPD at Pt.[80] This is likely as they are in direct electrolytic contact through the leak. As a result Cu^{2+}(aq) ions are deposited and stripped below and above about 0.6 V_{RHE}.

Therefore, the first figure of merit, which judges the o-ring compression controlled by its indentation, is clear. The second key parameter – i.e. the copper contact-sample pressure – is judged by the cell's series resistance, which is measured through EIS as previously described (see subsection 2.5.2). It depends on three influences which add up: the electrolyte resistance, the sample conductivity and the desired sample contact

quality. As outlined in section 5.2, the electrolyte resistance has only a minor impact in the order of a few Ohm.

Therefore, the contact quality and the sample conductivity are left. One of the earlier versions of the cell exhibited 14.9 kΩ series resistance. After placing two layers of Kimtech wipes underneath the sample it dropped to 0.9 kΩ. A different sample exhibited 460 Ω with two layers; adding another layer further decreased it to 120 Ω. From this experiment an optimized value of the sample indentation could be estimated. Testing the same sample within the final cell, which is constructed considering the mentioned value, confirmed the success of the optimization by showing $(110 \pm 1)\,\Omega$ series resistance.

The working hypothesis is that the remaining series resistance is caused by the ohmic resistance of the just 10 nm thin film – including a minor electrolyte contribution. The actuality of this educated guess is estimated by measuring the resistance of the mentioned sample simply with two alligator clips. The distance between both clips was roughly similar to the distance of the sample surface covered by the o-ring (i.e., its cord thickness), which separates copper contact and electrolyte. (see Fig. 15d)) The measured $(507 \pm 7)\,\Omega$ are larger than the $(110 \pm 1)\,\Omega$ measured within the cell. Firstly, this indicates that it is reasonable to assume that the sample itself causes the remaining series resistance. Moreover, less resistance within the cell could be explained by more contacted surface area all around the sample by the copper contact – instead of just the area of the clips – on the one hand.

On the other hand, less resistance due to the electrolytic contact can be made plausible with a one dimensional resistance ladder model as shown in Fig. 15d). By adding circuit elements the overall resistance is determined by:

$$R = R_\mathrm{o} + \cfrac{1}{{}^1\!/_{R_\mathrm{s}} + \cfrac{1}{R_\mathrm{f} + \cfrac{1}{\ddots + \cfrac{1}{{}^1\!/_{R_\mathrm{s}}}}}}, \quad \text{with } N \to \infty, \tag{51}$$

where R_o is the resistance below the o-ring, $R_\mathrm{s} = NR_\mathrm{S}$ the scaled solution resistance and $R_\mathrm{f} = R_\mathrm{F}/(N-1)$ the scaled films resistance. N represents the number of horizontal and vertical resistance pairs added, while $N \to \infty$ approaches the desired continuous description. The resistances are rescaled the following way: Dividing the film resistance R_F in two equal length parts results in an equivalent situation if it is replaced by $R_\mathrm{f} = R_\mathrm{F}/2$. If half of the former area is contacted by the solution (in a three dimensional rectangular picture), this results in a doubled resistance $R_\mathrm{s} = 2R_\mathrm{S}$ as the specific resistance stays the same. Evaluating this model with exemplary values of $R_\mathrm{F} = 500\,\Omega$ and $R_\mathrm{S} = 5\,\Omega$ leads to an overall resistance of $R \approx 50\,\Omega$ ($R_\mathrm{o} = 0\,\Omega$). This proves the point that the resistance of a partly electrically contacted sample – e.g. with alligator clips or the cell's copper contact – is expected to be lower, when alternatively connected to a well conducting electrolyte (over a larger area).

As the overall resistance increases with the distance the current travels through the film (from the outside to the inside), it makes intuitive sense that a well conducting electrolyte allows part of the current to 'choose the less resistive path' and already leave

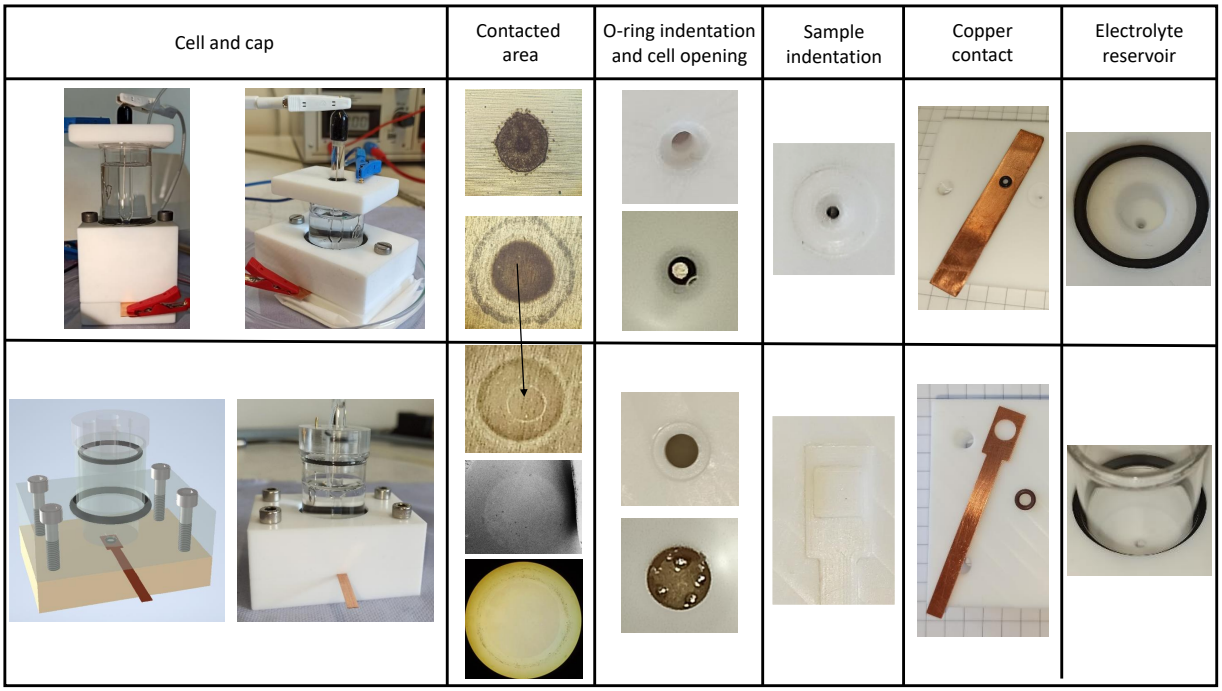

Fig. 16: Different aspects that illustrate the tuning process of the electrochemical cell. The mid row shows characteristic features of the self-built prototypes, while the bottom row shows the final, professionally machined version. The pictures of the contacted area, which becomes visible through signs of corrosion, stem from optical microscopy, photography and secondary electron (Everhart-Thornley detector) scanning electron microscopy. From top to bottom: nickel, twice platinum and twice RuO_2 (different samples). The bottom image stems from an intentionally dissolved sample (at prolonged extreme anodic potentials up to 2.7 V_{RHE}), otherwise, no optical microscopy contrast would be possible.

the film in its outer region near the contact. In addition, it is stressed that the one dimensional resistance ladder does not yet account for the radial symmetry of the contact. This would cause an increase of the radial resistance the smaller the distance to the center gets (as the current distributes on less circumference). Taking both effects into account serves as a foundation to imagine the current distribution on the surface. It is expected to concentrate to the outside of the film as sketched in green in Fig. 15d).

The fourth and last observation, which was relevant for the tuning process, is the behavior of produced oxygen bubbles. Fig. 15e) shows a cartoon of gas bubbles blocking the sample, which results in increasing electrolyte resistance until the circuit breaks. These bubbles accumulate during oxygen evolution studies. With the final setup the depicted complete blocking of the sample can only be reached by applying very high potentials, which are not used during the typical characterization.

3.4 Evolution of the thin film cell

There were two major steps during the cell design process at the beginning and the end. In the beginning, the trial and error process was boosted by self-building the prototypes. This allowed the integration of enhancements straightaway. This strategy had been pursued until the ~~the~~ first operating cell was achieved. Further improvements were reached with the aid of the advanced machining skills of the scientific workshop (physics department, university of Würzburg).

Some characteristic first and second generation cells are compared in Fig. 16 in the top and bottom row respectively. Starting from the left column, it becomes clear that the overall cell concept was already around from the first prototype onwards. Apart from that, the top cap's most important upgrade has been the transparent material, which allows to visibly keep track of evolving bubbles all the way down at the bottom of the cell where the sample is located. Also, on the practicability side, the top cap became more stable by fitting it into the glass tube by means of a FPM gasket. Furthermore, switching from a two to a four screw holding mechanism increased the stability and reproducibility of the cell.

The second column shows the area enclosed by the o-ring. This area becomes visible by signs of corrosion at a nickel (top), platinum (next two rows) and RuO_2 (lowest two) sample. The colored images are optical microscopy images and a photo, the gray scale image stems from the secondary electron signal of a scanning electron microscope (SEM). These pictures show the evolution from rather oval contacted areas, created by the self built cell, to reproducible circular shapes generated by the final cell. Because of the smaller achievable tolerances in the cell built with the workshop machining systems, the o-ring's inner diameter could be extended to the maximum possible amount. A photo of the Pt reference sample in the mid row shows a good comparison as the signs of corrosion from the older cell are still visible in its center. The upper sample shows a clear oval shaped dark region, which reappears as thin bright circle in the lower picture (within the larger corrosion circle from the most recent test).

The next column shows ~~the~~ how the indentation in which the o-ring sits developed between the original and final cell; the image shows a top-down view into the cell. Besides the already mentioned increased size of the hole, the texture and depth of the indentation, more importantly, have now reached their optimum shape. Consequently, the o-ring is compressed symmetrically.

Similar principles apply to the sample indentation, shown in the next column. In addition, an indentation for the copper contact is now also added into the final design. Before the indentation was introduced, the o-ring always had to be positioned manually while looking through the opening of the cell body. The through hole visible in the top picture solely aided the first-time positioning of the indentation.

The comparison of the self-made to the professionally machined copper contact further illustrates the gain in practicability by means of a facile and reproducible contact positioning.

The last column shows the PTFE cell body. Here, the whole diameter of the glass tube~~d~~ becomes usable nearly completely down to the sample. This allows for more room to locate the RE in the vicinity of the sample.

3.5 Excluding sources of contamination

3.5.1 Dissolved oxygen

At the beginning of section 1.1, it was pointed out that RuO_2[14] also catalyzes the oxygen reduction reaction[81,82] (ORR):

$$O_{2(g)} + 4\,H^+_{(aq)} + 4\,e^- \longrightarrow 2\,H_2O_{(l)}. \tag{52}$$

This is the reverse mechanism of the OER and, therefore, it has the same standard potential of $E^\circ = 1.23\,V_{RHE}$[8]. In acidic electrolytes it has similarly sluggish kinetics due to the required four consecutive proton-coupled electron transfers (PCET). An alternatively proposed pathway takes the detour over hydrogen peroxide (H_2O_2) formation.[82]

The ORR plays a minor, yet not completely negligible, role at the RuO_2 surface.[14] Therefore, this chapter aims to demonstrate how background currents induced by dissolved oxygen can be excluded in later measurements. To investigate the amount of dissolved oxygen, Pt is chosen as it is one of the best performing ORR catalysts[83]. This further implicates that procedures that are able to sufficiently reduce background currents for Pt will be more than sufficient for RuO_2. Pt is able to generate remarkably more ORR current than RuO_2.[14]

The typical signature[83,84] of an oxygen reduction related current at polycrystalline Pt (99.95%) in acidic environment is shown in Fig. 17a) (red). This voltammogram, recorded at $70\,mV\,s^{-1}$, is the typical response when measuring in non-pretreated, air saturated electrolyte. Due to the reductive nature of the process a negative current is expected. The rise of the absolute current starts considerably below the standard potential, which is a complementary situation as in the case of the OER – i.e. sluggish kinetics induce an overpotential. The reduction of the oxide layer starts around $1.0\,V_{RHE}$, and is located slightly before the actual ORR onset. That is also the reason why it is also called underpotential oxygen reduction, because the oxide stripping is happening first. The ORR onset potential can be guessed from the positive going sweep, since no superimposed oxide reduction is present there (Fig. 17a), yellow circle). Furthermore, the comparison to the clean voltammogram clearly hints where the oxide reduction is taking place simultaneously. The second maximum in the negative going sweep (after the plateau at $0.8\,V_{RHE}$) is caused by the initially high oxygen (reactant) concentration in the vicinity of the electrode, which results in a high ORR related current. This current then firstly decays according to the Cottrell equation (Eq. 38) until it reaches a steady state (Eq. 39). The typical Pt surface reactions including the double-layer charging occur in parallel.

By flushing the electrolyte with nitrogen most of the dissolved oxygen can be replaced. This is realized by adding a small purge tube directly above the electrolyte surface. It is turned up until the surface clearly bends due to the impinging gas. This results in a clean Pt voltammogram (black). Alternatively, the purge tube can be inserted into the electrolyte and operated in a bubbling mode. As this causes unstable CV experiments, the other method is preferred in the present case.

For the actual RuO_2 experiment, the electrolyte is pre-bubbled for several minutes before it is filled into the cell. To ensure sparse oxygen conditions during the experiment, the electrolyte is continuously blanketed afterwards. The ability of this procedure to yield satisfactory results has been checked against Pt. This experiment is presented

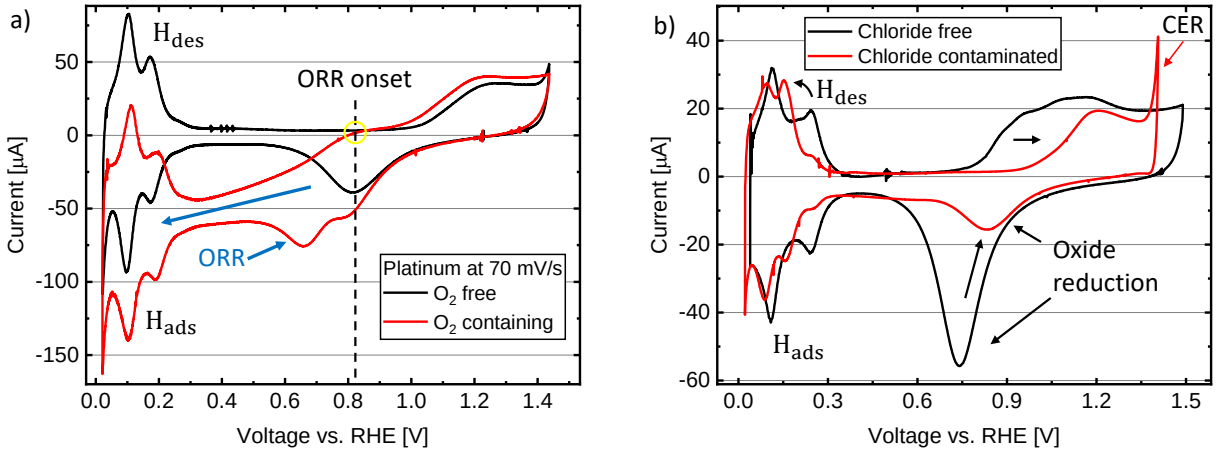

Fig. 17: a) Cyclic voltammogram of platinum in 1 M H_2SO_4 under N_2-saturated (black) and ambient air (red) conditions. The presence of dissolved oxygen from ambient air enables the oxygen reduction reaction (ORR). The onset can be estimated from the anodic (upper part of the) scan as it is superimposed by the oxide reduction in the cathodic sweep. b) Cyclic voltammograms of platinum in N_2-saturated 1 M H_2SO_4. The differences between the chloride-containing and chloride-free conditions are indicated by arrows. The onset of the chlorine evolution reaction (CER) becomes visible if chloride is present. As both measurements were taken at different scan rates (and stem from different experiments) the current of the chloride-free case (200 mV s^{-1}) is scaled by a factor of two to match the expected slower scan-rate (capacitive) response of the chloride-containing case (100 mV s^{-1}).

as black curve in Fig. 17b). The remaining tiny downwards bend around 0.4 V_{RHE} could be due to residual oxygen. It should be noted that the oxygen free conditions can only be sustained until the first experiment that includes (i.e. sufficient positive potential to yield) the anodic evolution of oxygen. In the case of Pt, the ORR current became visible then, in the case of RuO_2 it did not. The Pt CE is usually not driven in the OER regime, because too high negative potentials (i.e. positive potentials at CE) have not been required at the WE.

3.5.2 Chloride ions and chlorine gas

A major problem that occurred during this thesis was contamination of the electrolyte with chloride ions. This section discusses evidence that eventually led to this conclusion while exploring the catalytic reduction of chlorine gas.

To build on the preceding Pt discussion, the experiment, which originally aided as final confirmation of the contamination's origin, is discussed first. The red curve in Fig. 17b) shows Pt measured with a self-built AgCl RE. It is noted here that equivalent measurements using self-built AgCl REs for CV at RuO_2 confirmed that the response is equivalent to that seen from the ALS commercial AgCl electrodes. Therefore, it seems to be an intrinsic problem of the chloride-containing electrode type if no additional modifications are introduced.

Chloride-induced deviations from the typical platinum cyclic voltammogram are well documented in the literature.[77,85–87] The presence of chloride induces a shift of the H adsorption peaks and hinders the formation of the oxide layer beyond 0.8 V_{RHE}. The latter peak is caused by the competitive adsorption of Cl^- ions and surface hydroxide species.[87,88] Furthermore, it was proposed that the rise in the chloride contaminated case occurs at the point of the intrinsic surface hydroxide (PtOH) to surface oxide (PtO)

transition.[87] The second indication is the earlier rise of the CER current compared to the chloride-free reference experiment. This is reasonable, as the OER is expected[41] and observed (Fig. 5b,c)) to set in at higher potentials in the chloride-free case – which consequently exhibits no CER.

A typical cyclic voltammogram of RuO_2(110) at $200\,mV\,s^{-1}$ is shown in Fig. 18a). As these cyclic voltammograms will be discussed extensively later, the focus of this discussion lies solely on the changes caused by the CRR:

$$Cl_{2(g)} + 2\,e^- \longrightarrow 2\,Cl^-_{(aq)}, \quad E^\circ_{Cl_2} = 1.359\,V_{SHE}\,[8]. \tag{53}$$

The three shown voltammograms illustrate the effect of successively increasing the upper potential limit. From black to red ($1.5\,V_{RHE}$) the current starts to rise due to the CER. If just the standard potentials of the OER $E^\circ = 1.23\,V_{SHE}$[8] and CER would be compared, one could expect the OER to occur first. Two things have to be taken into account: the standard potentials are a fair approximation of the potential where the reaction can be roughly expected within a pH = 0.1 solution at room temperature (nearly standard conditions for at least the proton concentration and temperature), but chlorine and chloride are far from fulfilling those conditions; furthermore, the CER is more easily catalyzed by RuO_2[47] than the OER as it is the more facile reaction, which results in an overall more favorable CER when overpotentials are included.

The production of Cl_2 enables its reduction, which becomes visible as additional current around $1.1\,V_{RHE}$ in the negative going sweep below the standard potential. In the blue curve, the upper limit is increased 100 mV further, which triggers reasonable chlorine evolution. Thus, the chlorine concentration near the electrode rises and the reduction peak increases. The area of the reduction peak is proportional to the number of reduced Cl_2 molecules considering the two electron process and the potential scan rate.

The two reduction peaks (C1, C3) of the blue curve have been reported by literature. A case that very closely resembles the present situation was reported by Kuo *et al.*[51]. They investigated high quality MBE-grown RuO_2(110) thin films (also on a TiO_2 substrate) in 0.1 M H_2SO_4 in both clean electrolyte and after addition of 0.1 M KCl. The addition of KCl simulates the leakage of chloride ions from the used AgCl RE, which utilizes saturated KCl as an outer filling solution. The feature around $1.1\,V_{RHE}$ (C1) shows up at a similar potential to the work of Kuo *et al.*[51]. The group of Hepel *et al.*[52] showed their ability to produce nice quality – judging from a cyclic voltammogram – RuO_2(110) surfaces by means of chemical vapor transport (CVT). Basically all of their observations from an extensive study of the CRR within 1 M HCl could be reproduced.[15] The following explanation of the reduction features is in line with the mentioned work.

The C1 feature behaves distinctly from C3 when we consider the anodic and cathodic scan. The reduction at C1 is catalyzed by a certain stable surface present within the potential region of the peak. This causes a rise and fall correlated to the available catalytic sites. It rises simultaneously with the hydrogen adsorption surface redox peak around $1.2\,V_{RHE}$ visible in the clean black voltammogram. It is likely that the hydrogen adsorption competes with the adsorption of the mandatory $O_{ot}Cl_{ads}$ intermediate in this case. A Pourbaix diagram from Sumaria *et al.* would even predict a thermodynamically stable $Ru_{cus}Cl_{ads}$ species within the relevant potential range.[89] Beyond that, this is not in line with prior calculations by Exner *et al.*.[90] In any case, the active surface

can reproducibly be reactivated during the anodic sweep, which is clearly hinted by a consistently returning reduction current within the same range.

This is in stark contrast to C3. After the reduction peak maximum, the current decays in a Cottrell-like fashion while the reactants are depleted. If the scan is reversed, this decay proceeds and is additionally kinetically limited while the applied CRR overpotential decreases. As proposed by Hepel *et al.*[15], the difference to the earlier peak could be related to a reaction mechanism proceeding over $Ru_{cus}O_{ot}$ at C1 and over bare Ru_{cus} at C3. The already mentioned DFT-study of Sumaria *et al.*[89] supports exactly this mechanism. During C1, an oxygen terminated stable surface is expected to undergo a transition to a surface including stable $Ru_{cus}Cl_{ads}$. As a result, the reaction can proceed over the on-top oxygen until it is prohibited as chloride adsorbs at the underlying Ru_{cus} sites, thus replacing the on-top oxygen. They actually expect the next step to be a transition to a surface with bare Ru_{cus}, which should occur around $0.25\,V_{RHE}$. A further study[91], which only includes protons in its calculations, predicts the beginning of the uncovering of Ru_{cus} sites already at $0.4\,V_{RHE}$. This would actually fit to the experimental behavior.

Fig. 18b) shows the key experiment that finally lead to the right conclusion. It stems from the same setup as a). Up to this point, the working hypothesis has included the idea of a pure surface reduction process driven by the analogy to the Pt surface oxide reduction. This could be excluded by the shown experiment, where the potential is held for $\{1, 2, 4, 8, 16, 32, 60\}$ s at $1.35\,V_{RHE}$ in each consecutive cycle. The reduction peak C1, and thus the amount of reduced chlorine decreases with increased holding time. The holding potential is chosen as mainly capacitive double-layer and surface protonation currents are present, while the reduction is not yet dominant. The inset confirms this: when the scan is stopped the charging currents decay nearly instantly; during the holding period a negligible current $<4\,\mu A\,cm^{-2}$ establishes and further decays. Proceeding the scan results in another jump as the charging current sets in again. If C1 would correspond to the reduction of a surface oxide, it should not depend on a holding time at potentials where it is still stable. A process that perfectly fits this behavior is the diffusion of freshly produced chlorine gas from the electrode into the bulk electrolyte. The reduced charge (proportional to C1) is therefore correlated with the diminishing availability of reactant. C3 is not as nicely in line with C1 likely due to current limitations above a certain mass transport limit, which does not play a role at C1 yet. Furthermore, the amount of already reduced species at C1 introduces an additional parameter (besides t_{hold}), which determines the initial conditions for the C3 reduction.

By now, a chloride ion contamination is decisively proven: The peak attributed to the CRR depends on the upper potential limit (Fig. 18c)) and decreases when the freshly produced chlorine gas is allowed to leave the vicinity of the electrode by diffusion (Fig. 18c)).

The missing link is to show that KCl, which is expected to leak from the REs, causes it. Therefore, in Fig. 18c), the influence of adding small amounts of diluted KCl solution is investigated. This is the continuation of the experiment in b). We note here that the experiment was performed after running an extended version of a characterization protocol that included scans up to $1.7\,V_{RHE}$, as discussed in detail later. It is likely that mainly the part of the characterization at higher anodic potentials (up to $1.7\,V_{RHE}$) changed the sample due to a corrosion process. As a result of this, the reduction feature C2 appears. It behaves in an analogous manner to C1. The features, which were already

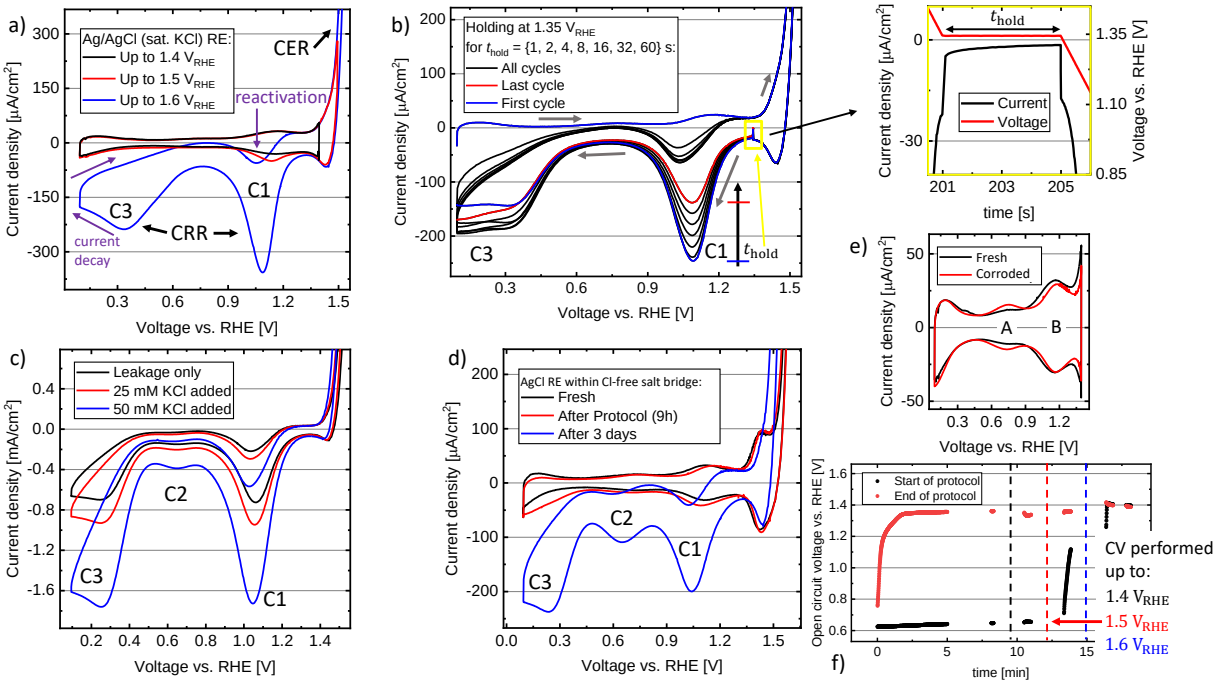

Fig. 18: Cyclic voltammograms of the same RuO_2(110) thin film in 1 M H_2SO_4 recorded at 200 mV s^{-1}. All measurements exhibit the cathodic chlorine reduction features C1 and C3. With increasing sample life time (measurements at high anodic potentials over an extended period of time) the additional reduction feature C2 develops. a) - d) are in chronological order and e) shows a comparison of the initial small range voltammogram and the final state: Peak A increases in comparison to peak B. a) After extending the upper potential limit high enough to trigger the chlorine evolution reaction (CER), chlorine reduction features develop. b) Holding at a rest potential (1.35 V_{RHE}) where mostly double-layer charging – and less faradaic current – occurs, allows the freshly produced chlorine gas to diffuse away from the electrode surface. Therefore, the holding time correlates with the intensity of reduction feature C1. The magnified (yellow) graph shows the current decay during a rest period: An initial large jump is caused by the capacitive discharge of the double layer. The remaining current serves as an estimation of remaining slow faradaic processes. c) Proof that observed features stem from leakage of RE electrolyte solution: C1-C3 increase in line with the addition of diluted KCl solution. d) Preventing the leakage by an additional salt-bridge compartment: It needs three days of constant immersion to reach a contamination nearly comparable to the direct immersion in a). f) Open-circuit voltage (OCV) in between consecutive CV experiments of increasing upper potential limit analogous to a): The OCV is sensitive to the Cl_2/Cl^--couple.

present in b), increased due to the ongoing leakage process. Adding additional KCl salt solution further intensifies exactly the already observed three features (C1, C2 and C3), which proves that these presumably chloride-related features are in fact introduced by KCl from the reference (and not from somewhere else).

Finally, when the situation became clear, the goal was to avoid the contamination. This was reached by adding a further salt bridge compartment, using a gel type or a chloride-free RE as described in subsection 2.2.2 and subsection 2.2.3. The preceding discussion also illustrates an advantage of RuO_2's high sensitivity to chloride ions, as it can be utilized to check for contaminations by a simple CV experiment. This is done in Fig. 18d), where a commercial AgCl electrode (ALS) is connected by a bridge containing a chloride-free salt solution (1 M KNO_3). The black curve shows a clean CV response directly after immersion. This was the first time the surface redox feature just below 1.5 V_{RHE} became visible without the superimposed CER related rise. Higher scan rates were needed to make the feature more dominant, and therefore observable, before. After the initial black voltammogram a typical characterization protocol ran once and took nearly nine hours. A small contamination appears afterwards. Nevertheless, the contamination could be significantly reduced compared to a directly immersed AgCl electrode. The unavoidable shift to higher potentials induced by LJPs, discussed in subsection 2.2.3, is also visible. The scale is deliberately not corrected to visualize this effect.

Another three days of constant immersion and partly continuous cycling between the potential limits result in the blue curve. Here, the amount of leaked chloride is still less compared to direct immersion, however, it becomes comparable. Next to the reduction peaks, the earlier rise of the current caused by the CER becomes visible. If this is the case, kinetic data represent mainly the CER at the beginning and at higher overpotentials a non-trivial competition between both reactions.[92]

In addition, an observation that supports the discussion of the next chapter can be made. Namely, the increase of feature C2 is accompanied with an increase in the amount of transferred charge associated with the smallest surface redox feature (peak A, at 0.8 V_{RHE}). Fig. 18e) shows the comparison of two small range – not influenced by chloride – voltammograms taken at the time of experiment a) (black) and after the leakage experiment d). The ratio of the peak areas, i.e. charges, of A and B clearly changes in a way that feature A becomes more prominent.

Lastly, it is noteworthy that there is another indicator that is sensitive to the Cl_2/Cl^--couple. This is the open-circuit voltage (OCV) of the sample. The OCV is basically determined by a Nernstian equilibrium (Eq. 26) between electroactive species. It is never obvious to determine which reaction is predominantly determining the OCV. However, a distinct trend has been observed for all of the RuO_2 thin films in chloride containing solutions. Fig. 18f) shows the OCV measured between consecutive cyclic voltammograms. Similarly to experiment a) the upper reversing potential is successively increased. The black and red points represent the same series of measurements taken at the beginning and end of a nine hour characterization protocol. It is the same sample as before, however, this time the commercial electrode of experiment d) is used without a double junction. The initial OCV starts to rise after extending the range to 1.5 V_{RHE} and clearly rises after the first set of cyclic voltammograms up to 1.6 V_{RHE} as in the firstly discussed experiment a). This illustrates that solely the presence of chloride is not sufficient to affect the overall OCV. But as soon as chlorine gas is produced the value rises up to about 1.4 V_{RHE}, which is roughly near the standard potential of the Cl_2/Cl^--couple.

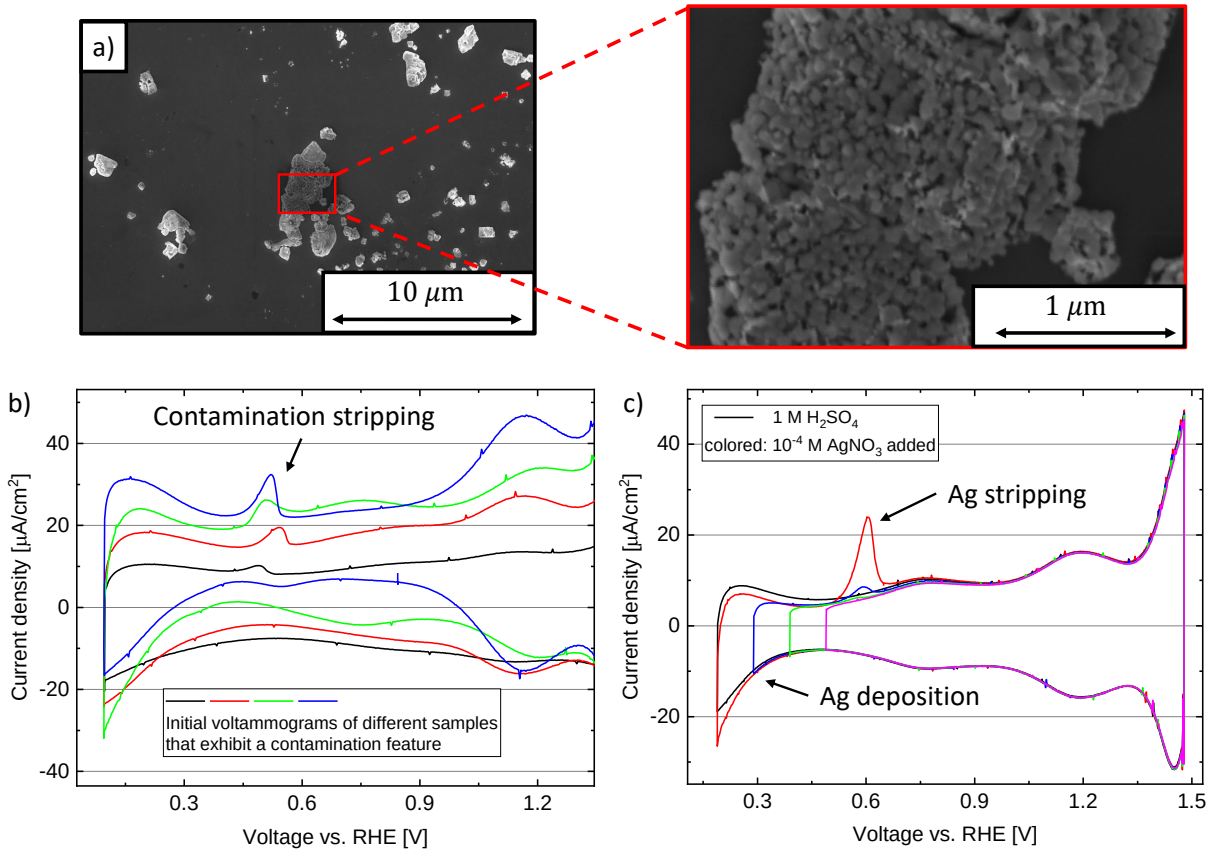

Fig. 19: a) Scanning electron microscopy images of silver grains (confirmed by energy dispersive X-ray spectroscopy) on the RuO_2 thin film within the catalytic area recorded with the in-column, i.e. in-lens (IL), secondary electron detector. b) Four examples of initial RuO_2 voltammograms taken at 200 mV s^{-1} in 1 M H_2SO_4. The curves are stacked by means of a constant offset to increase the visibility of the contamination peak. The samples were directly taken from the storage box (stored after growth) without any pretreatment. Each of the samples shows an additional metal ion stripping feature in the positive going anodic sweep. c) Clean RuO_2 voltammogram (black) and after addition of 10^{-4} M $AgNO_3$ (colored). When the range is extended below the $Ag^+_{(aq)}$ deposition potential, a silver stripping peak develops.

The red points, which are taken at the end of the experiment, show that the OCV quickly finds a higher value than initially due to a certain Cl_2/Cl^- background concentration. The smaller additional rise after increasing the range can be attributed to the changed chlorine/chloride ratio due to the CER and CRR, which have been triggered just before.

3.5.3 Silver ions

The final observation, which calls for an explanation, relates a pair of contamination peaks that showed up in the data of a select number of samples when they were put into the cell for the first time. There are three hints that support a contamination by silver ions.

Firstly, surfaces partly covered with silver conglomerates with sizes ranging from about 100 nm to several microns have been found on two of the samples that showed the additional features. They are easily distinguishable from the darker RuO_2 surface in the SEM micrographs shown in Fig. 19a). They are recorded by a secondary electron (SE)

detector, which is operating in a backscatter-geometry (IL) parallel to the incident electron beam. This geometry includes mainly secondary electrons that directly interacted with the primary beam – or have at least a shorter trajectory within the sample. Therefore, it allows for a higher lateral resolution compared to an Everhart-Thornley (ET) SE detector located out of the beam path. The contrast could be caused by the higher porosity of the particles, which hence increases the intensity by the edge effect. Basically more secondary electrons per projected area are able to leave the surface within their restricted penetration depth compared to a purely flat area. To avoid a possible confusion: the edge effect is usually superimposed with shadowing effects, which tell that surfaces oriented normal to the detector appear the brightest. Shadows are less pronounced in the IL geometry than in the ET operation mode. Furthermore, the contrast could be induced by a different work function or charging property.

Besides the SE detector, SEM offers the capability to detect X-ray fluorescence induced by the incident electron beam via an energy dispersive X-ray (EDX) measurement. Several grains at several spots of the sample were identified as silver by this method. The Ti fluorescence from the TiO_2 substrate was damped in line with the silver signal, likely depending on the grain thickness. One of the investigated areas is shown in Fig. 19a). The darker background serves as silver free reference spectrum. An image with a larger detail view on the right shows silver grains in form of bright conglomerates.

As silver paste was applied to the bottom of the substrates during growth, the presence of a silver contamination is highly probable. In addition, a trace contamination can also be introduced through the AgCl reference electrodes.[93] Hepel *et al.* studied the sub-monolayer silver electrodeposition at RuO_2 single crystal surfaces.[94,95] As their cyclic voltammograms in 0.1 M H_2SO_4 with 0.1 mM Ag^+ closely resembled the deposition and stripping peaks observed in Fig. 19b), the experiment was reproduced in 1 M H_2SO_4 to confirm their findings. This experiment is shown in Fig. 19c). Likewise they published SEM micrographs of their silver deposits, which are similar to the ones just shown.

In Fig. 19c), the positive oxidation current corresponding to the silver stripping peak depends on the lower potential limit of the cyclic voltammogram. We refer to this positive peak as a stripping peak, correspondingly, at lower potentials a negative current deposition peak is expected. Thus, no stripping is expected before the potential has been sufficient to induce a silver electrodeposition. The superimposed deposition currents can be estimated by the comparison to the black reference voltammogram. The deposition is fairly mass transport limited, because the deposited silver ions – in this case stemming from dissolved silver nitrate ($AgNO_3$) – are supplied by the bulk solution. This causes a broad feature. In contrast, stripping of the silver grains produces a fast and sharp stripping peak as all the reactants are readily available at the electrode surface. The current rises exponentially first (Butler-Volmer regime, Eq. 7) and is harshly interrupted when the dissolution is completed. The small observable peak potential (and onset potential) difference between experiment b) and c) is accounted to the different nature of the included silver ions stemming either from silver paste or silver nitrate solution.

Usually, the contamination peak disappeared during the experiment. This is reasonable if we consider the small charges accompanied with the stripping peaks. Additionally, the voltammogram with a similar lower limit as in Fig. 19b) results in a considerably larger deposition and stripping peak (the plot is omitted for clarity purposes). It is likely that the contaminations are below the detection limit, after they have dissolved into the bulk electrolyte. Therefore, after exchanging the electrolyte once, they are basically gone. This sets 0.1 mM Ag^+(aq) as the upper bound of the silver ion contamination, even though it may be orders of magnitude above the real concentration after dissolving the present silver grains.

In addition, as the positive peak was identified as stripping process, it is reasonable to assume that surface processes occurring at higher potentials are not obstructed either way. This is reflected in the higher potential region Fig. 19c), since the black and colored curves overlap.

4 Surface Chemistry of RuO_2(110)

The aim of this chapter is to present all important observations that can be interpreted in terms of potential-dependent surface reconstructions. Unless stated otherwise, the discussed data stems from representative good quality samples. Consequently, the conclusions are claimed to be general statements about the RuO_2(110) surface. A comparative study of all available samples is presented in chapter 5.

4.1 Samples: A whole phase diagram of RuO_2(110) epitaxial thin film growth

All samples that were electrochemically characterized stem from the successful growth optimization program of Kessler[27]. To find the best set of PLD growth parameters, substrate temperatures ranging from 230 °C to 730 °C were investigated at different oxygen partial pressures ($[10^{-2}, 10^{-4}]$ mbar). Therefore, a considerable amount of thin film samples, all exhibiting slightly different RuO_2(110) growth modes and surface morphology, is available. This allows to double check conclusions within a group of similar samples and check for differences to other groups.

Most of the samples have already been characterized by low-energy electron diffraction (LEED), reflection high-energy electron diffraction (RHEED), X-ray photoelectron spectroscopy (XPS) and some of them additionally by X-ray reflectometry (XRR), transmission electron microscopy (TEM), atomic force microscopy (AFM) and scanning tunneling microscopy (STM). As the main figure of merit is expected to be the actual surface morphology and homogeneity for electrocatalysis experiments, this sample characterization is completed by energy-dispersive X-ray spectroscopy (EDX), scanning electron microscopy (SEM) and AFM.

4.1.1 Structural characterization by scanning electron microscopy

Fig. 20 shows high resolution SEM images of all samples at the same magnification. All of these images are representative for the predominantly observed surface structure; always checked at several spots and areas of the sample. All images were recorded prior to any electrochemical experiment and allow for a categorization into four subgroups. All results were cross-checked by AFM (not shown).

Four samples (green) show a flat surface structure at the maximum possible magnification. The first two samples of the row have already been identified as flat by the initial RHEED characterization[27] – i.e. islands tend to merge. The third sample in the row had originally been categorized to exhibit islands[27], but, at least within the observable lateral resolution, it appeared flat. The last sample exhibits small cracks but is still mostly flat.

The next (blue) category shows clear three-dimensional structure, which induces considerable roughness. All of the blue category samples were grown at least 100 K above the identified ideal substrate temperature. This is also true for the yellow category. The first sample in the blue category shows an intermediate behavior between flat and irregular structures, and is indicated by a slightly different shade of blue. This transition proceeds over to the next sample in the blue row, which shows flat regions at different height levels. The last two samples exhibit a rough, grainy morphology with pillar-like features. The pointy clusters from the green category seem to be (partly) replaced by smaller crystals.

The yellow category turns out to be perfectly consistent with the prior RHEED observations from Kessler[27]. All yellow samples are grown above the ideal temperature and pressure – they share the same oxygen partial pressure (10^{-2} mbar), which has been identified to considerably slow down the growth process.[27] The yellow films show hints of the substrate's terraces. The TiO_2(110) substrates were observed to exhibit a terrace width of about 100 nm by AFM shown in the master's thesis of Kessler[27]. In the SEM picture three full terraces exhibit about the size of the depicted 300 nm scale bar. Visible terraces are not necessarily a sign of too thin or bad quality films, even though in this case such an interpretation would be consistent with the prior RHEED characterization.[27] Large completely uncovered regions were also identified by SEM on the last two samples in the yellow row.

Two samples of preliminary growth studies, grown far from the ideal parameter space, were also available. They exhibit a large amount of holes and trenches and belong to the red category of perforated films. The actual presence of Ru (and O) on the substrate was confirmed via EDX (not shown). Their broad featureless voltammograms, shown in Fig. 20 next to the red samples, already hint that CV is sensitive to the surface quality.

4.1.2 Investigation of typical surface defects by X-ray fluorescence spectroscopy and electron backscattering

The first type of surface defect, which is present at several spots at different samples, is shown in Fig. 21a). It also represents the perfect occasion to briefly explain the different detection modes of SEM that are utilized to investigate the film's surfaces throughout this thesis. The image shows a Ca-containing crystal recorded with three different imaging detectors. Starting from the left, secondary electrons are collected by an Everhart-Thornley (ET) detector. The combined shadowing and edge effect becomes visible around the protruding crystal. Predominantly the increased number of escaping electrons per projected area highlights the edges that are oriented near parallel to the primary electron beam – they appear brighter. Superimposed, some shadows are visible. Utilizing the analogy of the electron beam being the observer (here: located over the sample at normal incidence), and the detector's position representing the illumination source, the shadows can be easily identified with the additional knowledge that the ET detector is located at the top direction of the image. This analogy is based on the fact that electrons escaping toward the detector are more efficiently collected by the collection bias (brighter contrast) as electrons escaping in the opposite direction – they are shadowed by ridges of the sample.

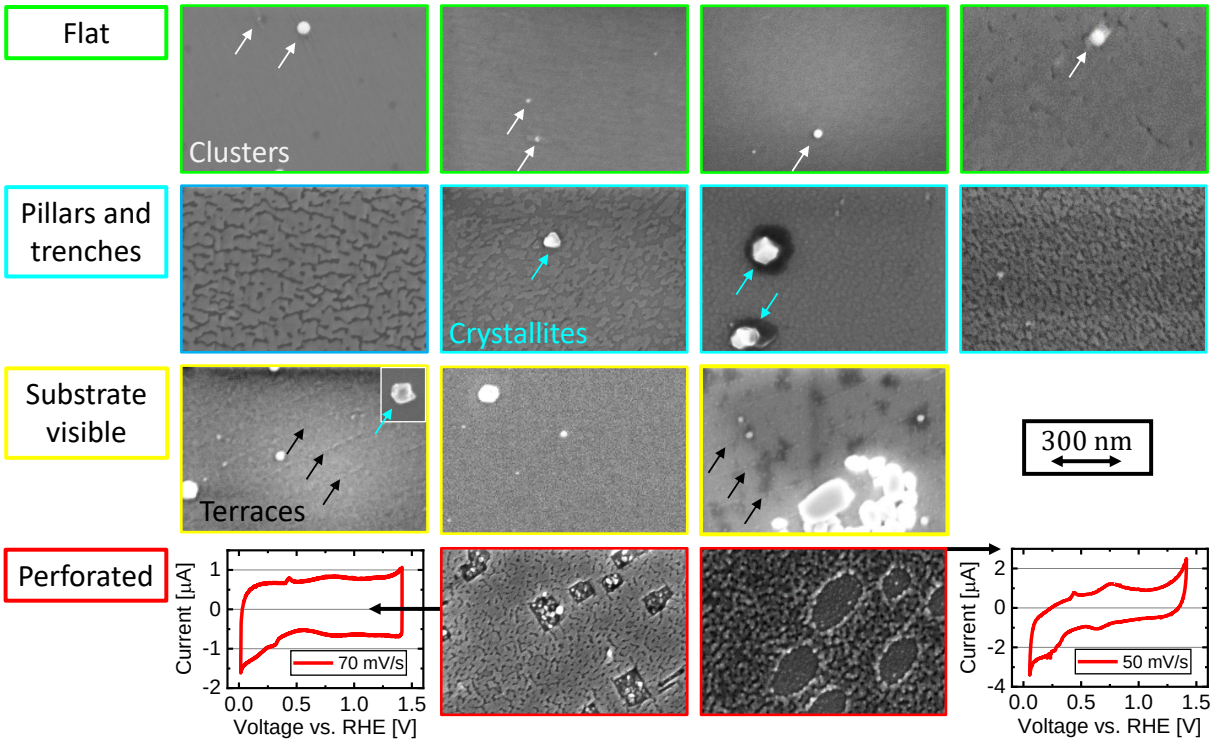

Fig. 20: Results of the morphological characterization by scanning electron microscopy (SEM): All images are recorded with the in-lens (IL) detector and show the same magnification according to the scale bar. Four groups can be identified: flat samples with pointy clusters (green), samples exhibiting rough structures and crystallites (light blue), presumably extra thin samples with faint signs of substrate terraces or delaminated areas (yellow) and perforated films (red) with respective cyclic voltammograms next to them. The leftest light blue sample represents a transition between rough and flat surfaces, which is indicated by a slightly different shade of blue. The middle yellow samples shows no clear signs of terraces but larger delaminated areas in lower magnifications.

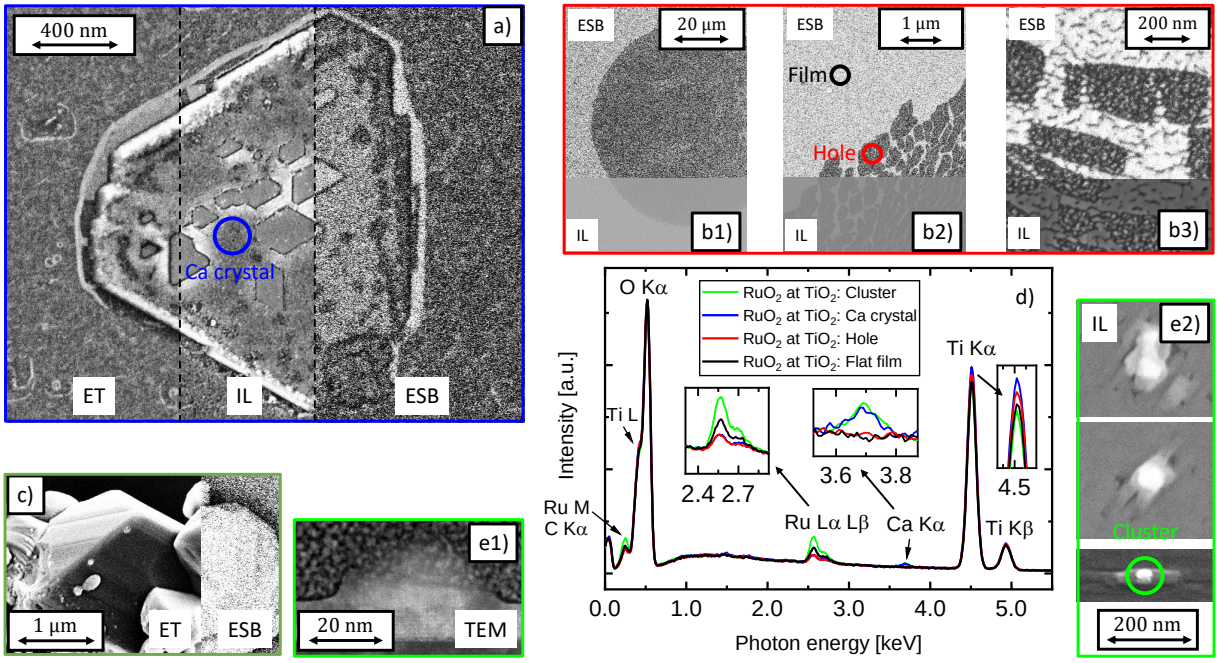

Fig. 21: Scanning electron microscopy (SEM) images recorded with the Everhart-Thornley (ET), in-lens (IL) and energy-selective backscattered (ESB) - detectors. The elemental contrast of the ESB detector is confirmed by local X-ray fluorescence spectroscopy (taken at colored circles in SEM images) – spectra shown in d). Different types of typical surface defects at the $RuO_2(110)$ surface: a) Ca-containing crystals, which induce circular disturbed growth, shown in b), around them. b) Holes in the flat film. c) Larger Ru-containing crystal. e1) Cross-sectional transmission electron microscopy (TEM) image and SEM image, e2), of a smaller Ru-containing cluster.

The middle part of Fig. 21a) shows the corresponding IL detector signal. This detector eliminates the shadows as it is positioned in normal position to the sample, which is analogous to illumination from the top. A clear example is observable at the upper edge of the crystal. Furthermore, due to the special positioning of the detector, mainly electrons that have directly interacted with the incident beam are collected. This results in an increased lateral resolution as the average path electrons travel through the sample (especially in lateral direction) is shortened, thus, the interaction volume decreases. The image becomes sharper.

The right part of of the Fig. 21a) shows the energy-selective backscattered (ESB) detector. This detector is located behind a negatively biased filter grid, which sits behind the IL detector. The electrons that arrive at the IL detector are the lower energy half of the overall released electrons collected within the lens system. Mostly backscattered primary electrons are collected. These electrons interact with the sample via Rutherford scattering (orbiting the positive nuclei) and carry information about the local atomic mass. As the scattering cross section is proportional to the atomic number, this detector's contrast is correlated to the atomic composition. It reveals that some RuO_2 (heavier) is deposited on top of the crystal while the blank TiO_2 (lighter) substrate is visible around it. All of the IL images at the bottom of Fig. 21b) are backed up by compositional contrast (ESB) at the top. The common observation (at several samples) was that every area containing several of those crystals is surrounded by an even larger region of disturbed growth as shown in Fig. 21b1), dark area.

The last detection mode, already utilized to identify the silver contamination, shown

in Fig. 19a), is X-ray fluorescence spectroscopy (EDX). Representative spectra, recorded locally at certain defects (highlighted with colored circles), are shown in Fig. 21d). As the interaction volume of the SEM is larger than the 10 nm thickness of the sample's RuO_2 layer, and X-ray photons escape from deep below this layer, the main fluorescence signal originates from the TiO_2 substrate. The Ca Kα transition (blue) reveals the calcium content of the crystal. This signal has already been found at bare substrates prior to the growth.

The EDX spectra in Fig. 21d) are normalized to the background caused by Bremsstrahlung and recorded at 10 kV electron acceleration voltage (EHT). The low energy shoulder of the large O Kα peak is likely associated with the Ti L signal as it scales in line with the Ti Kα intensity. The probable Ru M signal is identified by the same thought. Likely it is superimposed by C Kα, which is expected at approximately 40 eV higher energy.

At the edge of the areas of disturbed growth (Fig. 21b2)), a transition from a flat to a perforated films is visible. What is hinted by the elemental contrast of the ESB detector is confirmed by the EDX spectra. When moving from the closed film (black) to a hole (red), the decrease of the Ru signal is accompanied by an increasing Ti signal. That there is at least some Ru present even within the (rectangular) holes, is visible in the high magnification image in Fig. 21b3).

The most frequent feature, which is also visible in the EDX spectrum (and indicated in green), is a small pointy ruthenium – likely ruthenium oxide – cluster (Fig. 21e1) and e2)). Fig. 21e1) shows a cross-sectional TEM and e2) three IL images. These clusters exhibit the largest Ru intensity of the presented spectra. Usually they are surrounded by rectangular plateaus as they are probably deposited first and induce additional growth in the surrounding area thereafter. It is important to note that they randomly appear all over the film and always show similar EDX behavior. The discussed (green) spectrum also shows additional Ca signal, as it was taken in a disturbed growth region. This was the only available spectrum of a cluster at this specific sample; it was chosen to enable the comparison of all spectra. In the general case the Ru-clusters show no Ca signal.

In some samples, RuO_2 crystals with clearly identifiable faces grew. One of the larger examples is shown in the ET image in Fig. 21c). The shadow effect produces a clear three-dimensional impression while the ESB signal shows the similarity to the surrounding film (EDX shows a dominant Ru signal). Smaller versions of these crystals are visible in two of the blue and yellow category SEM images in Fig. 20.

This sets the stage for all of the following discussions and directly allows to utilize the SEM detection modes to determine the area contacted by the electrolyte in the next section. (section 4.3).

4.2 Potential dependent impedance spectroscopy

Before focusing on a variety of CV experiments, three representative examples of impedance spectroscopy at RuO_2 will be evaluated. EIS served as a crucial complementary tool that supported every CV measurement. It provides the capacitance C, the combined solution-sample resistance R_s and the charge-transfer resistance R_{ct}. In subsection 2.5.2 the Warburg impedance that models the diffusion limit of charge-transfer reactions has been discussed. This has never been observed in the present case of RuO_2-thin films, and is therefore omitted in the equivalent circuit model depicted in Fig. 22a).

Now, the statement that different circuit elements are more pronounced at different potentials from the theoretical section will be filled with life. The following impedance spectra were recorded in a frequency range from 200 kHz to 10 Hz with a sinusoidal excitation amplitude of 15 mV. A constant voltage is superimposed to this AC signal. Usually, each spectrum is recorded after a 10 s pre-polarization period to allow the system to approach a steady state. This condition is fulfilled except under OER conditions. The three representative polarization points that will be investigated are marked by stars in the cyclic voltammogram in Fig. 22d1). It represents a map that helps to orient where in the potential range which electrochemical reaction can be expected.

The black star in Fig. 22d1) marks the flat double-layer region where nothing but the capacitive charging of the Stern layer is expected. The respective Nyquist plot (Fig. 22a), black) basically resembles a RC-series circuit: a vertical line shifted by R on the real axis. A CNLS fit (as discussed in subsection 2.5.1) yields the capacitance and R_s presented in the table next to the plots. About 80 kΩ parallel resistance indicate that approximately no parallel processes occur.

There is the option to fit the impedance with a constant phase element (CPE) instead of an ideal capacitor that is often preferred in the context of electrochemical cells.[96,97] The non-ideality is represented by an additional CPE parameter γ which changes the ideal $-\pi/2$ phase to lower (absolute) values.

$$Z_{CPE} = \frac{1}{(i\omega)^{\gamma} Y} \tag{54}$$

$$Z_C = \frac{1}{i\omega C} \tag{55}$$

As a result, the vertical line becomes sloped. In fact, introducing this additional parameter provides a better fit. However, to aid the comparability of different samples and measurements, as well as the robustness of the fit, the ideal capacitor is chosen. This is further justified as fitting a CPE usually yields near ideal (in this case: $\gamma = 0.97 \approx 1$) CPE parameters, which proves the ideal capacitor as a sufficient approximation.

The next polarization point (Fig. 22a), red) is on top of surface redox peak B (red star in Fig. 22d1)). As expected, the capacitance increases in line with this feature as alternatingly adsorbed and desorbed hydrogen contributes charge per potential according to Eq. 43.

Up to this point, no indication of a parallel resistor has shown up. At the highest potential (blue star in Fig. 22d1)), considerable OER currents set in and the typical impedance circle of an RC parallel circuit shows up (Fig. 22a), blue) – this is caused by the decrease of the parallel charge-transfer resistor R_{ct} shown in the equivalent circuit in Fig. 22a). The charge-transfer resistance dropped by an order of magnitude, thus, the surface gets DC conductive due to the electrochemical reaction.

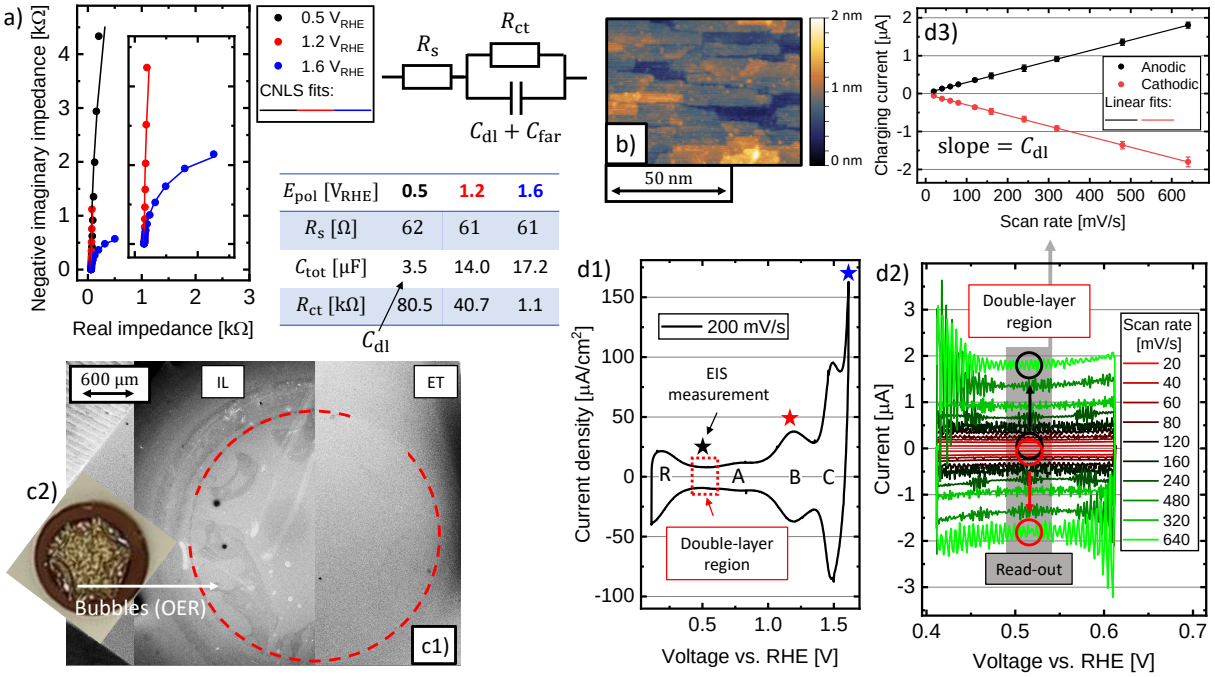

Fig. 22: a) Complex impedance (Nyquist) plot of a RuO_2(110) thin film at different polarization potentials depicted in black, red and blue. The respective polarization potentials are indicated by stars within the cyclic voltammogram in d1). A frequency range of [200k, 10] Hz is probed. Complex non-linear least squares (CNLS) fits are performed according to the shown equivalent circuit and the results are summarized in a table (fit uncertainty below the given precision). b) Representative scanning tunneling microscopy (STM) image[27] of a film grown at the same temperature as one of the samples, which utilized to determine the specific double layer capacitance. c1) Determination of the area contacted by the electrolyte by scanning electron microscopy (SEM). c2) Signatures of bubbles adsorbed to the sample within the cell (after the determination of the specific capacitance) can be recognized in the in-lens (IL) image. d1) Cyclic voltammogram of one of the utilized samples: The double-layer region is indicated red, the redox features A, B, C and R are labeled as well as the potentials of the EIS measurements in a). d2) Cyclic voltammetry in the double layer region: The rectangular shape indicates approximate capacitive behavior. At higher scan rates the potentiostatic control cycle gets prone to oscillations. The charging currents are read out in the gray area by averaging the included points. d3) Fitting of the scan rate dependent charging currents that yield the double-layer capacitance (DLC). The error bar indicate the (oscillatory) noise seen in d2).

4.3 Establishment of a reliable reference value for the specific capacitance

If a sample is not atomically flat, its real surface area deviates from its geometric (i.e. surface projected) area. In the electrocatalysis community, the real surface area is commonly called the electrochemically active surface area (ECSA). A widespread method to determine the ECSA is the derivation utilizing the double-layer capacitance (DLC) C_{DL} of the sample. This allows an evaluation by simply dividing by the capacitance per unit area:

$$\mathrm{ECSA} = \frac{C_{DL}}{C_s}, \tag{56}$$

where C_s is the specific capacitance of the sample. The aim of this section is to determine a reliable reference value of the specific capacitance (C_s) utilizing the near atomically-flat model samples investigated throughout this thesis.

This technique has been used since several decades to estimate the ECSA of metal oxides by now.[98] As in most cases the actual specific capacitance of the investigated material is not known, it thus became common practice to assume the existence of a more or less general value, which is then cited from 'popular' literature.[99,100] This is done, even though, it is not novel to point out that this value strongly depends on the sample properties and participating electrolyte.[98–100] When judging the activity of various catalysts by the current density they deliver, all efforts are condemned to fail if the assumed real surface area does not reflect reality.

Before intensifying this discussion, it makes sense to precisely state what contributes to the DLC and what this means for an interpretation. The DLC consists of the added up contributions of the fixed inner and outer Helmholtz planes as well as of the diffusive Gouy-Chapman layer as described in section 2.3. It is intuitive that the adsorbed water monolayer mostly depends on the sample's surface properties, while the diffusive layer is governed by the electrolyte's properties. The outer Helmholtz plane consists of adsorbed ions, therefore, it is an intermediate situation. While describing properties of aqueous electrolytes it is needless to mention that non-aqueous ones are not considered.

This leads back to the original discussion. It illustrated that a generalized value for several electrolytes (including different concentrations) can not exist. Nevertheless, the same material within the same electrolyte of the same concentration can be compared well. In addition, we have shown that the DLC method offers reasons that could prove it more valuable than atomic force microscopy (AFM) within the given context.

The diffusive part of the double layer has a size within the range of a typical AFM tip (around 10 nm), however, in the general picture the contribution to the total charge is higher the closer you are to the material's surface. As the Helmholtz planes are as thin as a water molecule and an ion monolayer in the order of some Angstroms, they become sensitive to even smaller pits in the surface that contribute to the overall roughness. Furthermore, the electrolyte reaches overhangs and deep pores. As a result, within the context of a most accurate value to normalize a measured electrocatalytic activity current, it seems to be the perfect method as the relevant medium of the process itself – the electrolyte – can be utilized to supply the information with how much of the sample's surface it actually interacts.

Currently the best guess value of the specific capacitance, which is used in several[99] studies[101,102], amounts to $C_s = (35 \pm 14)\,\mu F\,cm^{-2}$. It has been published by McCrory *et al.*[103] in a report that attempts to develop a standard protocol for the evaluation of activity and stability in OER catalysis. The whole preceding discussion is reflected in their method to determine this value: a few (ten) reported literature values of different metals within different concentrations of sulphuric acid electrolytes were averaged. While this might suffice as a rough estimation, the standard deviation of their sample (about $28\,\mu F\,cm^{-2}$) is nearly as large as the value itself.

In consequence, the establishment of reliable reference values of typically investigated materials (as e.g., RuO_2) would offer large benefits regarding the comparison of different materials' intrinsic activities. This requires experimental values of fairly atomically-flat surfaces like the ones used in this thesis. By now, the only value that has been specifically reported for the $RuO_2(110)$ surface amounts to $C_s = 14\,\mu F\,cm^{-2}$.[104] It was measured by EIS in 1 mM KF salt solution, on crystals that were grown by chemical vapor transport (CVT).

In the following, the determination of the specific capacitance that has been used to normalize the current densities within this thesis will be presented. It is noteworthy that, regardless of the actual accuracy of this value, all investigated samples of this study stay intrinsically comparable among themselves. This is because the capacitances are determined for the same material within the same electrolyte; and, all currents are normalized by the same specific capacitance value. Solely the comparability to the general literature depends on this value.

From the subset of measurements that is free of artifacts due to initial contaminations (subsection 3.5.3) or chloride (subsection 3.5.3), two samples could be identified as sufficiently flat (green category in Fig. 20) to provide a reliable reference value. This is judged by SEM, which is in line with AFM. A representative STM image from a sample grown at the same growth temperature as one of the two utilized samples is shown in Fig. 22b). So one of the samples has been grown at optimal temperature – as indicated by the growth program of Kessler[27] – and the other one at 100 K too low temperatures. As this definition of optimal parameters includes more considerations than the pure flatness of the sample, this does not disqualify the lower temperature sample as possible specific capacitance reference sample.

The most important parameter is the actual contacted surface area. The samples are assumed to be a sufficient approximation of a perfectly flat surface. SEM proved as a valuable tool to identify and measure the area contacted by the electrolyte. Fig. 22c1) shows two overlaid secondary electron images (IL and ET). The area enclosed by the red circles is identified as the electrolytically contacted area. The precision is estimated by aligning a reasonable minimal and a maximal diameter circle. The samples were measured in different, but equivalently built cells. However, the SEM reveals that each produces its own radius. This is further confirmed visibly by the comparison of pictures of the samples within each of the cells as one is exemplary shown in Fig. 22c2). The adsorbed bubbles stem from oxygen evolution studies while the specific capacitance is determined before any bubbles were present as these would shadow the surface area. Nevertheless, here they aid the clear identification of the contacted area as they indicate the inner margin of the o-ring. The IL detector shows another dark region, due to surface changes induced by the sealing o-ring, which could be distracting. Nevertheless, a fine dark line matches exactly with the circular shape also observed by the ET signal.

So, both samples are normalized by their according reference image. The diameters of the contacted circles are: $d_1 = (2.93 \pm 0.04)$ mm and $d_2 = (3.18 \pm 0.03)$ mm.

Now we need to determine the capacitance relating to this area. We already identified the double-layer region of a polycrystalline platinum electrode. It is localized in the flat region of a cyclic voltammogram, where no faradaic processes occur besides. In Fig. 17, where adsorbed chloride hinders the surface reactions, it is very pronounced in the middle of the voltammogram. Fig. 22d1) shows the voltammogram of the high quality reference sample. The thinnest and flattest part of this voltammogram (Fig. 22d1), red rectangle) is located between surface redox peak A and the restructuring region R (details will be discussed). Next to the presented method of extracting the capacitance from an impedance spectrum taken at this polarization point (Fig. 22d1), black star), the capacitance can be cross checked by scan rate-dependent CV in this region (Fig. 22d2)).

The principle in this instance is simple as the equivalent circuit of the cell reduces to an RC series circuit without a parallel resistor, because no other electrochemical processes happen. After some time $\tau = R_s C_{DL}$ has passed, a steady state charging current will establish:

$$Q = CU \tag{57}$$

$$I = \dot{Q} = C\dot{U} = C\nu \tag{58}$$

Q is the charge of the capacitor with capacitance C at voltage U. The time derivative of the voltage can be expressed by the scan rate ν. The capacitance can now simply be extracted by measuring the charging current for several scan rates and fitting a line. This is shown in Fig. 22d3). The CV scan parameters have been optimized with the aid of an extensive manual by Morales *et al.*[100].

The potentiostat's control cycle tends to oscillate at higher scan rates which limits the precision of this method. (Fig. 22d2)) The current for each scan rate is determined near $0.5\,V_{RHE}$ by averaging the current in a 50 mV potential window around the readout point. The standard deviation of the noise within this range aids as estimation of the precision of each point. According to Eq. 58 the DLC is determined by a linear fit as shown in Fig. 22d3). Anodic and cathodic values from the positive and negative scan are then averaged.

DLCs determined by EIS consistently showed $C_{DL}^{EIS}/C_{DL}^{CV} = (92.5 \pm 1.5)\,\%$ of the CV capacitance as checked with 26 measurements of 13 different samples. Therefore, the mean of both capacitances is used to determine the reference value of C_s. Its accuracy is estimated by the difference of both results. The mean value of both selected samples' capacitances $C_{s1} = (34 \pm 1)\,\mu F\,cm^{-2}$ and $C_{s2} = (37 \pm 2)\,\mu F\,cm^{-2}$ yields the final result:

$$C_s = (34.6 \pm 0.9)\,\mu F\,cm^{-2}.$$

Coincidentally, this matches the literature value of McCrory *et al.*[103]: $C_s = (35 \pm 14)\,\mu F\,cm^{-2}$. But as discussed earlier, this just confirms the right order of magnitude of this value.

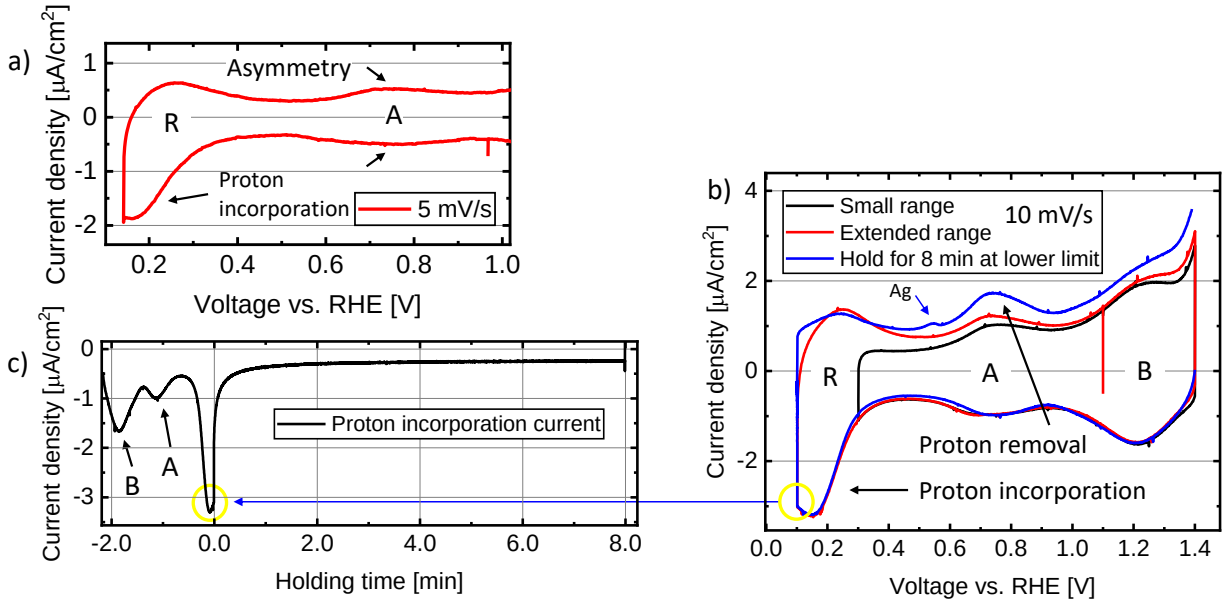

Fig. 23: a) Cyclic voltammetry at 5 mV s^{-1} exhibits a proton incorporation feature below R and an asymmetric redox feature A. The asymmetry is attributed to the proton removal feature, which is shown in b). b) Cyclic voltammetry at 10 mV s^{-1} in a small range (black) compared to a larger range, which extended to lower potentials (red), shows the additional proton removal current in the positive sweep. Holding the current at the lower limit (0.1 V_{RHE} for 8 min increases the additional current above feature A. A blue arrow indicates a possible Ag stripping peak (subsection 3.5.3). c) The current decays initially and seems to approach a non-zero proton implantation current during the rest of the period.

4.4 Cathodic proton incorporation

Before discussing the actual process behind the main surface redox transitions A, B and C in detail, the considerably different reconstruction feature R will be examined. We will show that it is related to a comparably slow proton incorporation process into the bulk crystal structure in this section – that also a faster surface adsorption process is superimposed, will be shown in a later section (subsection 4.5.2). Fig. 23a) shows a comparably slow scan rate voltammogram (5 mV s^{-1}), which exhibits two pronounced features both correlated to the reconstruction process. The first one is the negative rise of the current at the lower potential limit, which is not caused by the HER as this reaction sets in at least 150 mV more negative. The second observation is a clear asymmetry of redox peak pair A between the forward and backward sweep. The fact that this incorporation feature (Fig. 23a), below R) is more dominant (relative amplitude compared to A and the rest of the voltammogram) at slower scan rates points towards a slow electrochemical process relative to the surface redox reactions. This can already be seen when comparing the proton incorporation feature of the 5 mV s^{-1} experiment in Fig. 23a) to the 10 mV s^{-1} voltammogram in Fig. 23b). Further evidence will be presented when discussing the scan rate dependence of the whole voltammogram later (Fig. 24d)).

Two cases were found in the literature that describe a similar behavior at the lower potential limit; one performed at RuO_2(110) thin films[48] grown by CVT, the other one at nanoparticulate[105] RuO_2. Both explain their observations by proton intercalation into the bulk electrode material. There is also a theoretical study that describes proton diffusion into bulk RuO_2 and proposes a most stable structure for the $HRuO_2$ composite.[17]

The experiment shown in Fig. 23b) offers a strong intuition that perfectly fits a sluggish proton incorporation process, which becomes favorable below a certain voltage threshold. The black small range (lower limit: $0.3\,V_{RHE}$) voltammogram (Fig. 23b)) serves as a reference. Extending the range down to $0.1\,V_{RHE}$ (red curve) results in additional current in the positive sweep. This is a result of the incorporated protons, which are removed again. All curves are recorded at $10\,mV\,s^{-1}$. The amount of intercalated protons depends on the potential as well as the time spent below the threshold. This is demonstrated by the blue voltammogram, which is recorded with the same settings but with an additional 8 min waiting period at the lower reverse potential. Plotting the current versus time in Fig. 23c) reveals a decaying current at this potential ($0.1\,V_{RHE}$). The area underneath this curve corresponds to the charge of inserted protons and the current seems to approach a steady-state non-zero insertion current. Proceeding the sweep back to more positive potentials clearly shows that the additional current increased even more in the blue scan.

This is consistent with the assumption of an invertible proton insertion. It is intentionally not called 'reversible' as this term is mostly connected to 'readily reversible', fast processes in the general literature. Using the typical nomenclature this would be an 'irreversible' process due to its sluggish kinetics, i.e., relatively slow chemical rate constant. The seemingly asymmetric behavior at higher potentials to B is caused by the OER onset. In addition, there is a small pre-peak at $0.55\,V_{RHE}$ indicated by a blue arrow in Fig. 23b). The position would be in line with the silver ion stripping peak that has been described in subsection 3.5.3. A very low concentration present in the solution would be indicated, as eight minutes were required to deposit the observed amount.

The discussed experiment of Fig. 23b) is similar to one performed by Lister *et al.*[48] (CVT crystals), which inspired this experiment. The aim was to reproduce their findings at one of the investigated samples – this was successful. As observed, the proton removal current increases in accordance with the amount of time spent at the lower limit. (Fig. 23b))

To conclude, two features could be attributed to proton incorporation into the bulk RuO_2 crystal lattice: the first is below R, i.e. in the negative sweep, and the other is above A, i.e. in the positive sweep. They were identified through the time-dependence of the proton removal feature (above A) on the proton incorporation feature (below R) – both occur on a reasonably long time scale (slower than pure surface redox processes).

4.5 Surface reconstructions probed by cyclic voltammetry

4.5.1 Different growth methods from the literature

This section represents a brief overview of efforts toward CV at RuO_2 reported in the literature. It puts the investigated good-quality samples of this thesis into perspective and illustrates that they compare well to single crystal films from the literature, which have been used for CV experiments.

Before getting to the benchmark single crystalline films, the voltammogram of a nanoparticulate electrode shown in Fig. 24a) will be discussed. This specific sample has been used for rotating disk electrode (RDE) measurements, which will aid the reasoning in the next chapter (subsection 5.1.2). The counterparts of the features B and C (which will also be discussed for single crystals afterward) are labeled in Fig. 24a). The feature

located at lower potentials to the position where peak A would be expected (A), is not strictly reversible. This is concluded from a visible peak-to-peak separation (see dashed line in Fig. 24a)). Features B and C appear quite shallow compared to (110) crystals. The voltammogram of Fig. 24a) matches a CV experiment from the literature of nanoparticulate RuO_2 conducted at the same scan rate in 0.5 M H_2SO_4.[105] Sugimoto *et al.*[105] also investigated the cathodic proton incorporation, which was discussed in the preceding section, at these polycrystalline samples. A general observation, which is also true for other types of RuO_2 electrodes as e.g. hydrous ones, is a much broader featureless voltammogram. Interestingly, there is also a case of single crystalline films that exhibits a broad cyclic voltammogram: the (101) surface. The (101) surface has been reported twice to show a comparably flat CV response.[26,22,23] However, the general CV literature of oriented RuO_2 films is scarce and partly inconsistent.[48,52,104,106,107]

Fig. 24b) shows cyclic voltammograms of four RuO_2(110) crystals grown by the commonly used techniques, namely: PLD (present work), CVT[21], molecular beam epitaxy (MBE)[51] and the oxidation of Ru(0001) single crystals[47]. CV of a PLD-grown sample at MgO substrate was also reported.[26] Unfortunately, the published data are from an alkaline environment. Therefore, a direct comparison is not possible as the voltammogram differs to the acidic one.[50] As the other three techniques allow for a direct comparison with the data in this thesis, their cyclic voltammograms are overlaid in Fig. 24b). While the potential could be reproduced as reported by the literature, the current had to be scaled manually (to mostly match peak B as well as C). This is caused by different current normalizations and reported scan rates.

The best overlap of our high quality sample is reached with the data from the MBE sample and the oxidized single crystal. While the latter technique's voltammogram (oxidized crystal) basically overlaps our data, the MBE sample shows a shoulder below feature B (1.0 V_{RHE}) and no trace of peak A at all. The CVT sample exhibits additional current between the features and different peak ratios.

4.5.2 Scan rate dependence

To learn more about the nature of the surface redox reactions, a range of different scan rates for the CV data is investigated. Fig. 24d) shows a capacitance plot ($C = I/\nu$) of a good quality sample for scan rates ν ranging from 5 mV s^{-1} to 500 mV s^{-1}. The measured currents are divided by their respective scan rate and normalized by means of ECSA according to Eq. 56. As a result, pure capacitive currents are expected to overlap independent of the scan rate as they scale linearly with the scan rate.

While the center region exhibits a reasonable overlap, scan rate dependencies show up at the high and low potential limit. The preceding discussion of the cathodic proton incorporation explained especially the slow scan rate behavior below 100 mV s^{-1}. Above this scan rate of 100 mV s^{-1}, the plot indicates less deviation from a capacitive scaling. This is a possible hint for a second superimposed process that rather has the properties of a surface adsorption. Hepel *et al.*[52] observed a reversible and symmetric peak pair, which they interpreted as H adsorption features, in the relevant potential region. Nevertheless, a symmetric pair of peaks has never been observed throughout this thesis.

Two possible explanations of the surface adsorption part of feature R, which appears stable toward higher scan rates in the capacitance plot (Fig. 24d)), would be in line with

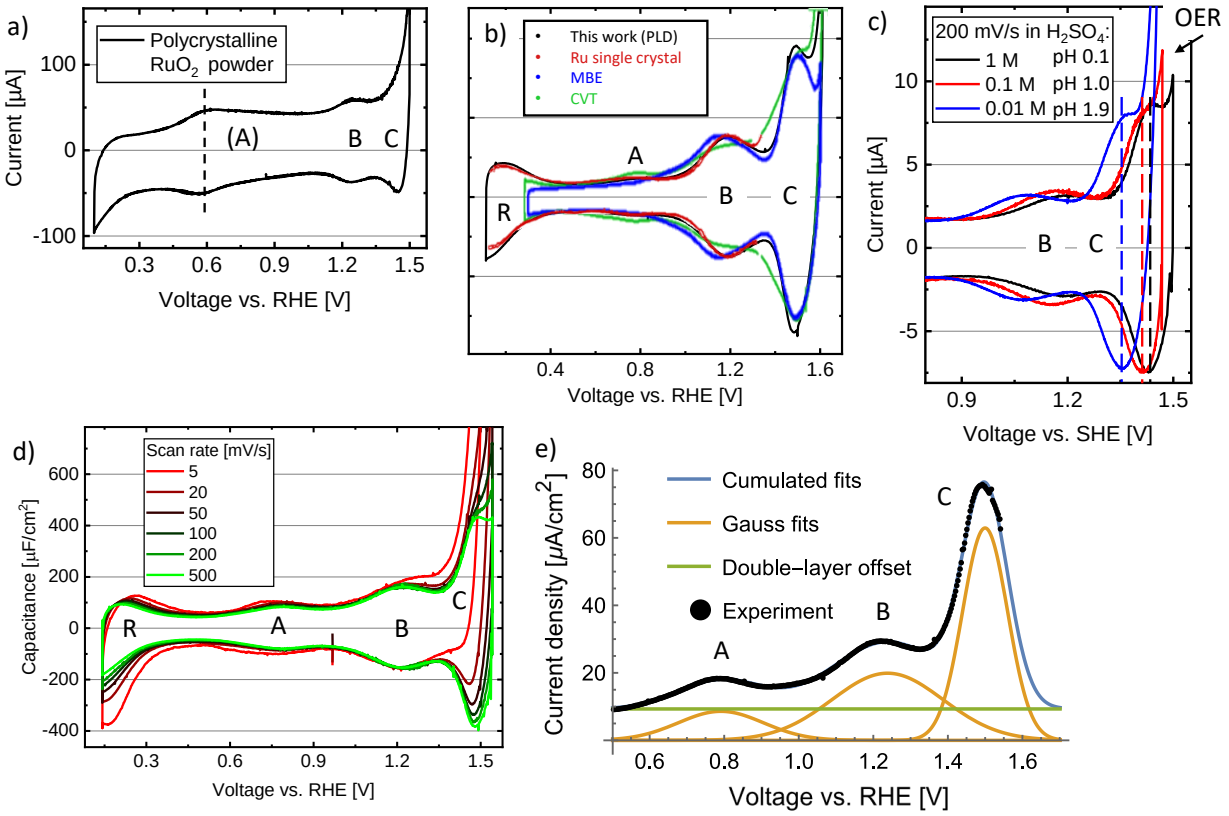

Fig. 24: a) Cyclic voltammogram at 200 mV s^{-1} of a RuO_2 powder electrode demobilized at glassy carbon (GC) by a nafion solution. b) Comparison of a good quality PLD-grown sample of the present work to common methods of the literature: molecular beam expitaxy (MBE)[51], chemical vapor transport (CVT)[21] and oxidizing a Ru(0001) single crystal[47]. c) Test of the pH dependence of the voltammogram by titration of 1 M H_2SO_4 to yield approximate values of pH 0.1 (black), pH 1.0 (red) and pH 1.9 (blue).[54] The redox features shift toward lower potentials on the standard hydrogen (SHE) scale. d) Scan rate dependence of the redox features R, A, B and C investigated by a capacitance ($C = I/\nu$) plot. Non-capacitive features like R and the OER can be identified in the non-overlapping regions of the voltammogram. e) Exemplary fit of a non-capacitive-background corrected voltammogram (negative scan subtracted from the positive scan). The double-layer charging current offset is fixed by a read-out in the double-layer region. Three Gaussians with unconstrained position, amplitude and width are fitted.

the observed chlorine reduction reaction (CRR) rise below 0.5 V_{RHE} (subsection 3.5.2) assuming it proceeds over Ru_{cus}. The first one is the adsorption of hydrogen at exposed Ru_{cus}. This would however require the deoxygenation of Ru_{cus} first, which represents the second possible reaction. Therefore, I propose that this removal of the O_{ot} species is the likeliest mechanism to explain the surface redox contribution. This could further motivate a more feasible proton diffusion into the bulk lattice via the more exposed surface at lower potentials. Nevertheless, this requires the assumption that the energy barrier for proton insertion is lower if O_{ot} is not present. By now, this is no more than an educated guess.

As the OER related current is not expected to scale with the scan rate, feature C gets easily distorted when the capacitive currents only contribute a small fraction to the overall current. This is the case at slower scan rates.

4.5.3 pH dependence

The pH dependence was checked with a sample of the blue (i.e. medium quality) category sample. Fig. 24c) shows voltammograms recorded at 200 mV s^{-1} in 1 M (black), 0.1 M (red), 0.01 M (blue) H_2SO_4. This corresponds to approximate pH values[54] of 0.1, 1.0 and 1.9, respectively. The electrolyte concentrations are clearly reflected in the EIS-determined series resistances of $R_s = \{(91 \pm 1)\,\Omega, (200 \pm 1)\,\Omega, (880 \pm 1)\,\Omega\}$.

Hydrogen related redox processes are expected to shift by 59 $\frac{\text{mV}}{\text{pH}}$. As the RHE scale already accounts for such a shift (Eq. 28), here, the SHE scale is preferred to highlight the pH-dependent shift. Qualitatively, the spectrum behaves as expected. A quantitative comparison is omitted as these early measurements still had an uncontrolled amount of chloride (subsection 3.5.2) present. It is visible that the curve at pH 1.9 (blue, Fig. 24c)) exhibits a disproportional shift compared the red one. This shift would be expected to be about as large as the shift from black to red (59 $\frac{\text{mV}}{\text{pH}}$) in Fig. 24c). This is attributed to the not yet ideal (chloride-containing) experimental conditions.

The second observation is the earlier rise of the OER, which is expected as the overpotential, measured on a pH independent scale, is also lowered by 59 $\frac{\text{mV}}{\text{pH}}$ (Eq. 28). In this (chloride-containing) case, the visible effect is partly accompanied by the CER.

4.5.4 Fitting procedure

Up to this point, most statements could be sufficiently supported by rather qualitative observations. To take a step toward the extraction of reliable quantitative data from a CV experiment, the fitting procedure, which is described now, was developed.

Earlier, Fig. 10 justified the assumption of a Gaussian peak shape for peaks exhibiting a FWHM greater than about 90 mV assuming a one electron transfer process near room temperature. The scan rate dependent capacitance plots just demonstrated that a distortion of feature C can be counteracted by choosing higher scan rates. Unfortunately, there are limitations to the maximum usable scan rate. On the one hand, the potentiostat reaches its stability limits and oscillating currents get more dominant. On the other hand, as the capacitive current is directly proportional to the scan rate, ohmic drop increases accordingly and produces distorted voltammograms again. Live compensation of ohmic drop also stops to be feasible due to the fact that the potentiostat is already prone to control loop oscillations. One example of a voltammogram distorted by insufficient series resistance compensation was shown in Fig. 7d). The maximum scan rate that still seemed to deliver reasonable results is 3 V s^{-1}. Though it was possible to record highly distorted scans up to 400 V s^{-1}.

Thus, to further optimize a scan taken at a reasonable scan rate the positive and negative scans are subtracted (and divided by two). This suppresses the OER current and extracts the capacitive currents associated with the redox features A, B and C. The information about the OER is contained in the averaged scans. This method utilizes the symmetry of a positive and negative peak with respect to the zero current axis. In addition, the OER current is assumed to be equal at the same potentials for the forward and backward sweep (no hysteresis). The next chapter will show that, in fact, a small hysteresis occurs. Fortunately, it is negligible as long as the capacitive currents are predominant. The upper limit is set by this condition.

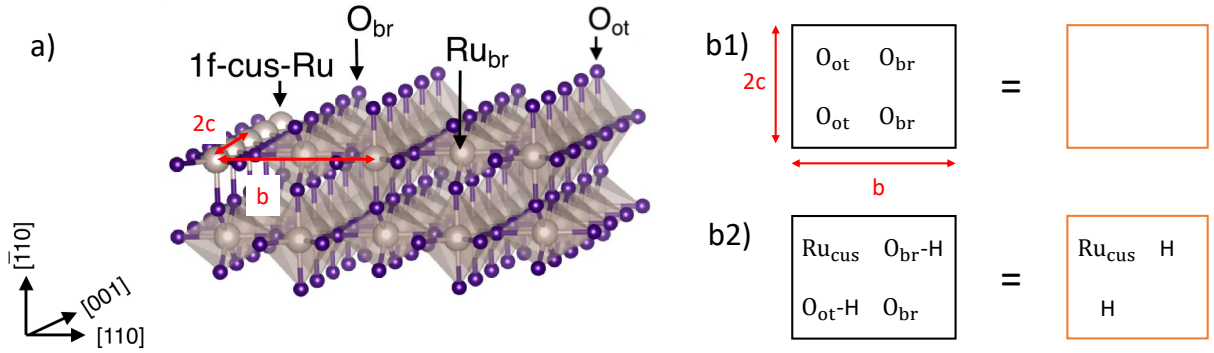

Fig. 25: a) The (110) surface of the rutile RuO_2 crystal structure. The unit cell dimensions are indicated by $b = 6.35$ Å and $c = 3.11$ Å.[108]. (graphics from Jovic *et al.*[19]) The on-top oxygen (O_{ot}) adsorbs to the Ru_{cus}-sites. b) Simplified sketch of two neighboring O_{ot} and O_{br} pairs. A fully oxygen terminated surface is indicated by an empty orange rectangle, b1). Only differences to this state are indicated, b2).

To avoid distortions due to Cl_2 trace contamination induced CRR currents in the backwards sweep, usually, scans utilized for fitting have been recorded below the CER onset – thus, no chlorine gas is introduced. Later, when chloride could be completely excluded, this has not been required anymore.

Finally, the fit can be performed as shown in Fig. 24e). The black points are all included experimental data recorded at a scan rate of 200 mV s^{-1} – the difference of the positive and negative scan divided by two. As described, the higher potential points are excluded as oxygen evolution currents become too dominant and unpredictable to correct for them. The current that is attributed to the double-layer charging at the lower limit is used to fix the offset. Consequently, the double-layer charging is assumed to be potential-independent. In addition to the fixed constant offset, three Gaussians with unconstrained FWHM, amplitude and position are fitted. A set of initial parameters was identified that yielded converging fits for all investigated samples. Whenever peak positions, widths or areas, i.e. charges (subsection 2.4.2), are mentioned in the following, they have been determined this way.

4.5.5 The RuO_2(110) surface

RuO_2 crystallizes in a rutile structure – its (110) surface is depicted in Fig. 25a). Common surface species are labeled. Bridging oxygen (O_{br}) atoms are considered as always present during this thesis. That is because they are more stable, i.e., stronger bound than on-top oxygen (O_{ot}), which is adsorbed at onefold coordinatively unsaturated ruthenium sites (Ru_{cus}).[1] This nomenclature just expresses that they have five instead of six surrounding oxygen atoms; six are expected in the bulk case.

Alternating rows of on-top and bridging oxygen point toward the ⟨001⟩-direction. Rows of the same type have a distance of $b = 6.35$ Å and neighboring ruthenium atoms within a row are $c = 3.11$ Å apart.[108] This results in a rectangular surface unit cell.

To aid the following discussion, a comic of each two neighboring surface unit cells is introduced as depicted in Fig. 25b). This means that each depicted rectangle contains two O_{ot} and two O_{br} sites. A fully oxygenated surface, b1), is chosen as reference point and only differences to this situation will be indicated. The empty orange rectangle represents the fully oxygenated situation of the black rectangle next to it. Fig. 25b2)

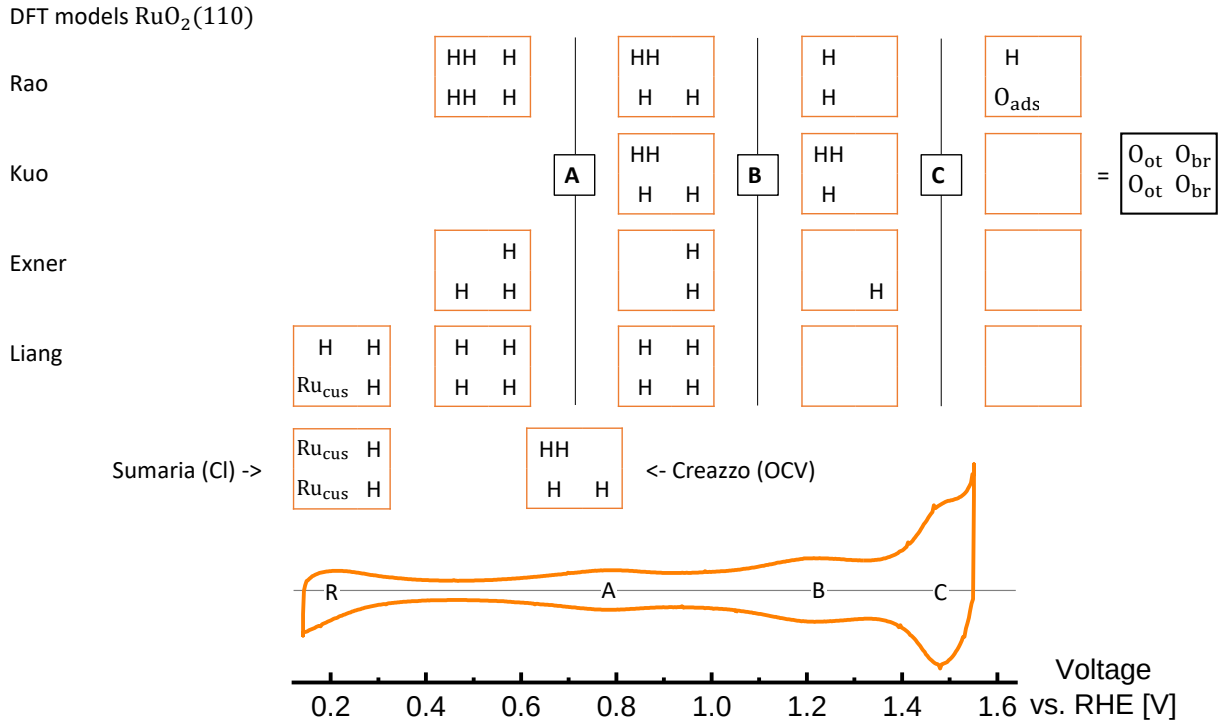

Fig. 26: Proposed theoretical models of stable surface configurations of RuO_2(110). It is always depicted what a certain model proposes within the potential region between two redox transitions as this is where the stable surfaces are expected to appear by the experiment. They stem from the following literature: Rao *et al.*[21], Exner *et al.*[34,109], Kuo *et al.*[49], Sumaria *et al.*[89], Creazzo *et al.*[110] and Liang *et al.*[91].

shows an example with adsorbed hydrogen at O_{br} and O_{ot} while one O_{ot} is removed and reveals a blank Ru_{cus} underneath.

4.5.6 Proposed models from literature

In the very beginning of this thesis, surface Pourbaix diagrams have already been utilized to motivate a change of the OER mechanism, which is induced by a potential dependent transition to a different stable surface configuration. As hinted at the end of the introductory chapter, these redox transitions are also observable by CV. This is because they are accompanied by a defined amount of transferred charge. As described in subsection 2.4.2, a reversible peak pair occurs around the transition potential.

The theoretical description of the RuO_2(110) surface utilizing Pourbaix diagrams started in 2010.[111,90] This time it was mainly focused on the CER driven by its industrial relevance. While DFT calculations have already been around to describe the OER reaction intermediates[32,112], Pourbaix diagrams were still restricted to bulk RuO_2[8], in contrast to surface adsorbates (explicitly excluding chloride). From the year 2017 onward several groups approached stable surfaces and surface transitions under OER conditions by means of DFT calculations.[21,34,49,89,110,91]

The findings that have been reported in the literature up to now are summarized in Fig. 26. The recently introduced sketch of the two minimal unit cells, where the O_{ot} (at Ru_{cus}) is on the left and the bridging oxygen O_{br} is on the right, is used to make all models comparable. As all calculations are reported a bit differently – sometimes including more transitions and surfaces – always the structure that fits best within the potential

range in between two transitions is shown. Since the aim is to find the most reasonable explanation of the actually observed experimental voltammogram, non-observable transitions are not considered. The stable surface configurations are always located in between two peaks – peaks are transitions from one surface to another.

Even a quick look at Fig. 26 reveals the largest problem of all approaches: the results depend strongly on the assumptions. Some examples of typical assumptions are mentioned here. The earliest study[111] (not shown) did not include solvent effects and basically assumed a gas phase environment. It was found by Exner *et al.*[90] that this makes a difference to the potentials attributed to certain configurations – and the determined configurations in general. Comparing two studies of IrO_2(110) reveals a further impact; taking the step from 'just accounting for solvent effects' to actual ab initio molecular dynamics (AIMD) again changes the proposed surfaces.[113,114] The most recent example[91], probably quite relevant for RuO_2, accounts for magnetic interactions (non-magnetic and antiferromagnetic cases) via DFT+U. This demonstrates that the theory is still far from reaching a consensus.

The first two rows, Rao *et al.*[21] and Kuo *et al.*[49], combine experimental and theoretical efforts. The latter study offers theoretical possibilities for transition B and C, by identifying the energetically most favorable sequence of configurations and attributes them to the CV transitions.

Rao *et al.*[21] uses *in situ* surface X-ray scattering while having the sample biased within a 0.1 M $HClO_4$ electrolyte. At four potentials in the voltammogram, they fit crystal truncation rod data and claim to determine the bond lengths (surface normal distances) of Ru_{cus}-O_{ot} and Ru_{br}-O_{br} separately. By identifying possible surface configurations theoretically and then selecting the ones which fit their experimental bond lengths best, they propose the depicted model. The specialty of their model is that they predict an adsorbed oxygen (O_{ads}) species that is stabilized by a neighboring adsorbed hydrogen via a hydrogen bond at high potentials (above peak C in Fig. 26). In spite of the fact that their DFT calculations also proposed the fully oxygen covered surface at higher potentials to peak C, they preferred the hydrogen bond-stabilized structure as it is the only one consistent with their experimental data. Although this is the most sophisticated approach to combine theory and experiment so far, this study is criticized by Over[9], who raises the point that the data may be overanalyzed. The main difference to Exner's[34] model is that in both preceding cases (Rao *et al.*[21] and Kuo *et al.*[49]) the bridging oxygen sites are expected to lose a proton first, in Exner's case O_{ot} is first deprotonated.

Liang's study[91] introduces larger unit cells that consequently indicate more intermediate (fractional) coverages near the expected transitions. Nevertheless, full coverages have been predicted within the regions of interest. Next to Sumaria *et al.*[89] they are the only ones which predict surfaces for the lower potential region, where a surface redox transition has been proposed to happen in parallel to the cathodic proton incorporation (section 4.4). Sumaria conducted their calculations in the context of the CER including chloride, however, it seems reasonable to assume that this surface does not exclusively rely on the presence of chlorine (as it includes no Cl_{ads} species).

DFT-molecular dynamics (DFT-MD) has been used in the study of Creazzo *et al.*[110]. As they utilized MD simulations of a slab of water molecules above a (444) supercell of $\langle 110 \rangle$ oriented RuO_2, without considering bias or pH, their result is placed near a typical open circuit voltage (OCV).

4.5.7 Surface redox transitions B and C

The rest of this chapter aims to combine all evidence gathered by the morphological surface characterization (section 4.1) and CV to propose a model that fits these observations best. The considered possible surface configurations are inspired by the presented literature.

All samples exhibited a decaying current at OER-relevant potentials (above 1.6 V_{RHE}), which will become a main topic in the beginning of the following chapter (subsection 5.1.2). Here, the decay will be utilized to investigate the surface redox transitions associated with peaks B and C. A representative flat sample (green category of the SEM characterization in subsection 4.1.1) is analyzed under continuous cycling at 500 mV s^{-1} scan rate.

Fig. 27a) shows every fifth cycle of the total of 400 cycles. This experiment is conducted between 1.1 V_{RHE} and 1.7 V_{RHE}. The amplitudes of the peaks (B and C), along with that of the OER current, are extracted for every cycle by averaging a small potential window (about 20 mV) around peak B and C and at the upper potential limit, respectively. Offsets are excluded by subtracting the negative from the positive peaks (same procedure as in subsection 4.5.4) and correcting by the double-layer charging current (Fig. 27a), green shaded area), which has been measured beforehand. Averaging directly before and after the high potential limit of the voltammogram effectively excludes the capacitive current in the OER region. The resulting amplitudes relative to their initial values (extracted from the first recorded cycle in the fresh state) are plotted versus the logarithm of the cycle number in the inset. Further background could possibly arise from the right tail of peak B; as it can be judged by the fitted voltammogram shown in Fig. 24e) this contribution is minor.

We already know that the peak area – and therefore the amplitude at constant width – is directly proportional to the charge transferred in the surface transition. (subsection 2.4.2) The easiest explanation for the decaying amplitude would be the shadowing of surface area by evolving bubbles during the OER. This can be excluded as it would scale the whole voltammetric current by the same proportion. Fig. 27b), which shows the ratio of peak B and C, indicates that this is clearly not the case.

For the following interpretation of the observed behavior we presume that the active sites of the OER are the Ru_{cus} surface atoms, which is consistently confirmed by the literature.[1,21] In addition, we make a key assumption – that the observed OER current decay is correlated to a loss of these OER-active Ru_{cus} sites. Evidence that supports this assumption will be presented in the following chapter (subsection 5.1.2): As a consequence of a supposed deactivation process, the OER current decreases in line with the loss or blocking of available Ru_{cus} sites. Since the O_{ot} adsorbes to the Ru_{cus} site, a loss of Ru_{cus} is always correlated to a loss of O_{ot}. This already excludes the Exner[34,109] model as he proposes that solely O_{br} participate in B and C (Fig. 26), which should not be affected by a loss of O_{ot}. Similar accounts for the model of Kuo *et al.*[49] as they propose solely O_{br} to participate in B. Furthermore, they propose solely O_{ot} to participate in C, whose validity will be checked in the next paragraph.

Therefore, what fractions of Ru_{cus} (where O_{ot} adsorbs) or O_{br} relate to the peaks B and C? To probe this question, the next simplest assumption is: 100 % of the sites participating in C are O_{ot}. In this case C should be directly proportional to the number of O_{ot}. Furthermore, a fraction of B should be contributed by unaffected bridge sites. This

would be in line with the qualitative observation that transition B suffers less decrease than transition C, as well absolute as relative.

Rao[21] and Liang[91] propose a model where the sites participating in B are half on-top and half bridge. (Fig. 26) Therefore, these models can be checked as this would relate peak B and C in the following way:

$$\frac{B}{B_0} = \frac{1}{2} + \frac{C}{C_0} \cdot \frac{1}{2}, \tag{59}$$

where the ~~the~~ fractions represent the relative peak amplitudes measured against their initial values (B_0, C_0). The formula expresses the stated models, as half of the sites ($O_{ot} \propto \frac{C}{C_0}$) are affected by the decay while the other half, O_{br}, is unaffected. Testing this model yields insufficient results (about 7 % deviation). The test was performed by the application of Eq. 59 to the experimental data of $\frac{C}{C_0}$ and comparing the result to the experimental data of $\frac{B}{B_0}$.

Consequently, the strategy pursued now is to extract the best guess model, which is hidden in the proportional scaling of peak B, C and the OER decay. We still presume that the active OER site is the Ru_{cus}[1,21], where O_{ot} adsorbs.[1,21] In addition, we weaken the prior assumption that 100 % of the sites participating in C are O_{ot}. Now following assumption is taken: All available O_{ot} sites contribute to the OER and to transition C, but this does not necessarily imply that no different type of species (the O_{br}) can additionally participate in C.

In Fig. 27c) the relative peak amplitudes $\frac{C}{C_0}$ and $\frac{C}{C_0}$ are plotted versus the relative OER current $\frac{OER}{OER_0}$. The relative currents are also normalized by their initial values. The anticipated quantities are extracted from Fig. 27c) by linear fits. They are the fractions of unaffected O_{br}-sites, which remain after extrapolating to the fully deactivated state (at 0 % O_{ot}), contributing to peak B and peak C. So the initial state of all quantities is one, which corresponds to the first recorded cycle. Each consecutive cycle yields another data point.

The linear relationship is expected if peak C is proportional to the OER-active sites. The linear scaling region of peak C allows for an interpretation of the extrapolated linear fit. In line with the assumption that all active O_{ot} sites are included within C, extrapolating to the indicated 100 % in Fig. 27c) yields the expected OER current for full O_{ot} availability in case of a purely linear scaling relationship (as expected in the high active site density regime when excluding the interactions). The linear region can also be extrapolated to the point where all sites are expected to be deactivated – this is indicated by a yellow circle in Fig. 27c) at 0 % O_{ot}. Interestingly this value is not zero, which furthermore explains why the facile previously tested model according to Eq. 59 yielded deviations. This facile model assumed that 100 % of C are affected O_{ot} sites, which would lead to a full deactivation when extrapolating to 0 % O_{ot}. In contrast, even if all O_{ot} are deactivated, peak C is expected to have 25 % of its amplitude, i.e. contributing sites, left after the extrapolation. This can be explained by a O_{br} contribution to peak C of 25 %, while the part affected by the deactivation makes up 75 % O_{ot}.

After an initial non-linear region during the first cycles, peak C scales linearly with the OER current. The initial rise could possibly be related to interactions between reaction intermediates enabled by the high densities of still active sites, which are expected within this region. These interactions would in turn boost the OER activity by lowering

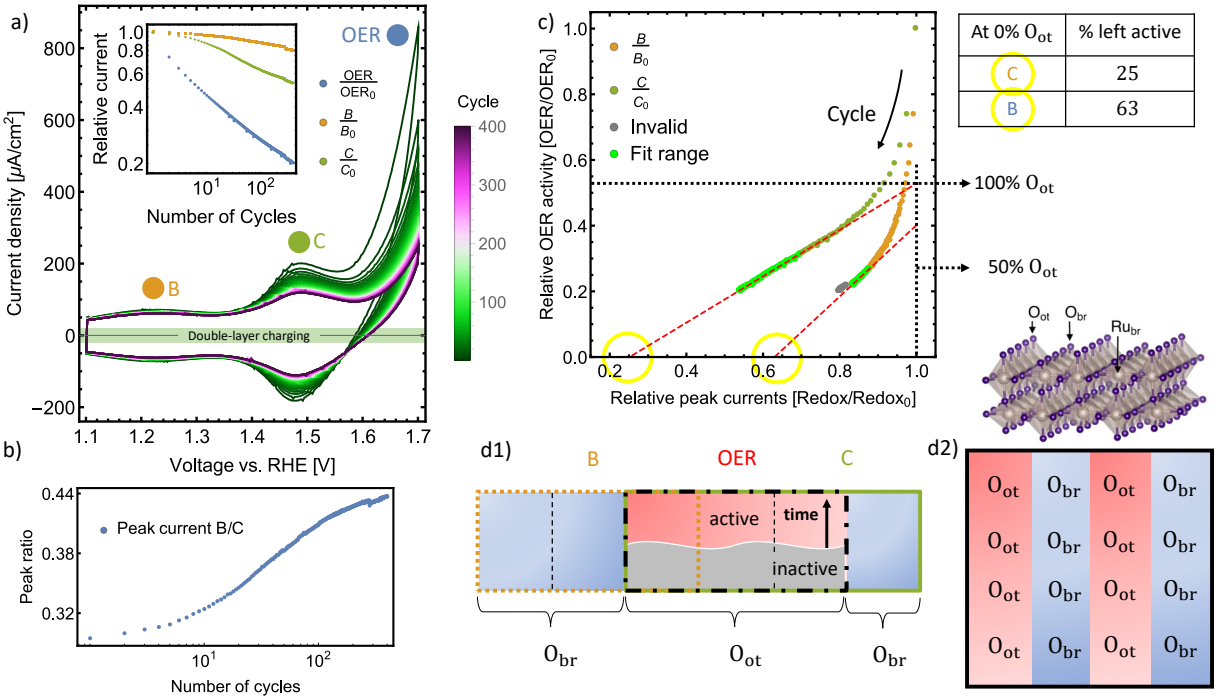

Fig. 27: a) 400 consecutive cyclic voltammograms recorded at 500 mV s^{-1}: The redox B (orange) and C (green) decay in line with the oxygen evolution reaction (OER) current (blue). The double layer charging current is indicated by a green shaded area. Only every fifth recorded cycle is depicted. The inset shows a double-logarithmic plot of the peak amplitudes normalized to their initial (first cycle) value. b) The ratio of peak current B divided by C changes during cycling. This excludes bubble-induced surface shadowing as this would leave the ratio constant. c) Correlation between the normalized OER current and the normalized peak currents of B and C: The linear scaling region can be explained by the OER current being directly proportional to the available O_{ot}-sites. Extrapolating to 0 % O_{ot} yields the fraction of the unaffected O_{br}-sites, which are left after all O_{ot} have been deactivated. The respective fractions of O_{br} are shown on the right. The disproportional scaling region could be caused by an interaction-induced increased OER activity (at high active site densities). d2) Sketch of the ideal (110) surface indicating O_{br} in blue and O_{ot} in red. d1) Proposed model based on the observed linear scaling behavior. The gray shaded area increases with time and indicates deactivated O_{ot}-sites. Redox feature C (green box) consists of 3/4 O_{ot}-sites and redox feature B (orange box) consists of 1/3 O_{ot}-sites. The extrapolated values of c) (yellow circle) indicate that 1/4 and 2/3 of the site (O_{br}), participating in B and C respectively, are left at full deactivation (gray area filled up to the top).

a crucial transition state energy. There are examples that propose the stabilization of OER intermediates via neighboring sites[21]. This stabilization of next neighbors is induced via a hydrogen bond between two adsorbed species: $O_{ot}O_{ads}$ and $O_{ot}H$, where the intra-solid H-bond connects the hydrogen adsorbed to O_{ot} to the O_{ads} surface atom. In addition, the literature proposes that the OER proceeds via a water dissociation step that is aided by a neighboring site[34,115]. On top of that, an exponential coverage-current relationship has been proposed for IrO_2.[114]

The extrapolated contribution of 25 % O_{br} to peak C can be visualized in the sketch shown in Fig. 27d1). The colored boxes have areas proportional to the number of sites participating in the related transitions. A sketch of the unit cell, which indicates the colors of O_{ot} and O_{br} used in d1), is presented in Fig. 27d2). In d1), the OER is represented by a black box and and covers all red O_{ot} sites. Within this box, the deactivation process is illustrated by the gray area which fills up over time. The linear plot in Fig. 27c) is extrapolated to infinite time: By this time, all (red) O_{ot} would be deactivated. As a

result, 3/4 of peak C (green box) are inactive and 1/4 stays active in the form of bridge site related transitions (blue area).

Back to the extrapolation in Fig. 27c): The relative amplitude of peak B exhibits a shorter linear region than peak A. In addition, a jump that is also visible in the cyclic voltammograms occurs (data afterward marked gray and excluded from the fit). Remembering how much less peak B is affected relative to C (20 % instead of 50 % relative decay), the linear region still seems reasonable. In this case, about 2/3 of peak B are expected to be left after the extrapolation. This information completes the sketch in Fig. 27d1) and adds the orange box, which represents feature B.

Now let us think of possible surface redox transitions within the surface unit cell, which cause the charge we observe in the discussed peaks. All O_{ot} sites already contributed one electron transfer (i.e. surface redox process) to feature C, which is indicated by the green box including all O_{ot} sites (the red area). Now it was found out that the transition of feature B (green box) also includes 1/3 of O_{ot} sites; the only possibility to fit this in the sketch is to include a part of the red area that already contributed to C. Consequently, a fraction of the O_{ot} sites is deprotonated twice subsequently – once during B and once again during C. The proportions of the sketch depending on the percentage of active sites do now reflect the experimentally observed situation, which can be summarized by the relations:

$$\begin{aligned} \frac{B}{B_0} &= \frac{2}{3} \cdot f_{O_{br}} + \frac{1}{3} \cdot f_{O_{ot}} \\ \frac{C}{C_0} &= \frac{1}{4} \cdot f_{O_{br}} + \frac{3}{4} \cdot f_{O_{ot}} \\ f_{O_{ot}} &\propto \frac{OER}{OER_0}, \text{ in the linear regime, and } f_{O_{br}} = 1. \end{aligned} \tag{60}$$

f indicates the fractions of active surface species and the bridge sites are assumed to be unaffected $f_{O_{br}} = 1$. O_{br} is unaffected, since the literature confirms that the Ru_{cus}[1,21] (and therefore, the O_{ot}) is the OER-active site (as presumed earlier).

The determined extrapolated values are rounded to the nearest, low denominator fraction. As only whole numbers of electrons can be transferred, the resulting few unit cell model becomes less realistic the larger it needs to be to match the determined fractions. If the representative few unit cell model becomes too large, a longer range interaction would have to be justified, which does not seem realistic in the present case of hydrogen bond-induced interactions. It is stressed that the uncertainties of the extrapolated value, given in the table in Fig. 27c), only represent the accuracy of the extrapolation. It is determined by starting both extrapolations 30 cycles, i.e. data points, earlier or later and estimating the maximum speak of the extrapolation of this. The error reflects the higher linearity of C compared to B.

The initial peak ratio of the sample, which had been used for the deactivation study, was determined by CV experiments twice at two different scan rates before the discussed experiment. This yields an experimental charge ratio of transition B relative to C of (77 ± 2) %. Within the uncertainty, this matches the sketched best guess model (Fig. 27d) of transition B having 3/4 of peak C's area.

A further hint is given by Kuo *et al*[49], as they observe a damping of feature C in

phosphate containing electrolytes. They propose that feature B stays unaffected, because phosphate adsorbs in line with hydrogen and, therefore, stabilizes both $O_{ad}H$ species.[49] Since these adsorbates are now stabilized by the adsorbed phosphate, feature C is effectively suppressed.[49] Extending their claim, a further possible interpretation of this behavior would be preferential adsorption of $H_2PO_4^-$ (dominant in their pH 2.8 solution) at $O_{ot}H$ sites. In their case feature C has also about 1/4 of its former amplitude left, which is in line with the proposed model of one of four participating sites (O_{br}) still being active.

Lister *et al.*[48] did a similar experiment in basic phosphate-containing solutions. In their case the damping of the peak is stronger at lower pH. The peak has the smallest amplitude at pH 11.4, where $H_2PO_4^{2-}$ is dominant. Unfortunately, as the transitions generally differ (at least in their voltammetric response) under acidic and alkaline conditions, a quantitative comparison of the peak amplitude is not possible.

Both the FWHM of B and C exceed the about 90 mV expected for an non-interacting one electron process (subsection 2.4.2). Relative to C the FWHM of B is about twice as large. Kuo *et al.*[49] supposes that the flexibility of H_2O_{ot} to transfer a proton to a neighboring bridge site (similar DFT surface energy) during transition B causes its increased width through the increased number of competing microstates. The same group did a follow up study of the temperature dependent adsorption behavior probed by CV.[116] They claim to have disentangled entropic and enthalpic adsorbate interactions and stress the participation of the surface solvating water layer (IHP). As their results are valid for the basic environment (0.1 M KOH) similar studies in acid could be promising.

Nevertheless, an interpretation of the peak widths of B and C based on Laviron's Frumkin isotherm interaction model (subsection 2.4.2) will be provided – based on the proposed model, which is illustrated in Fig. 29. Comparing transition B and C, their relative peak widths would suggest that peak B rather favors a mixture of its initial and final surfaces as the transition state is extended over a large potential range. ($FWHM_B = (280 \pm 20)$ mV, from Tab. 1 in subsection 5.4.3) Laviron's model (subsection 2.4.2) compares the interaction, which causes energetic gain or loss of certain surface configurations, of the separate initial and final state compared to a state where both initial and final species of the redox transition are present at the same time. The mostly H covered surfaces during transition B would be reasonable candidates for such a behavior as they are basically both composed of adsorbed hydrogen. Transition C on the other hand is restricted to a smaller potential window. ($FWHM_C = (110 \pm 10)$ mV, subsection 5.4.3) This means that either the initial or the final surface is preferred. The low H coverage phase in between seems to be avoided, which supports some kind of stabilization mechanism among neighboring H atoms[21] – maybe further assisted or mediated by the surface solvating water monolayer (in the IHP).

In summary, I propose that 2/3 O_{br} and 1/3 O_{ot} contribute to transition B and 1/4 O_{br} and 3/4 O_{ot} contribute to transition C. This is based on the observed OER-current decay presented in Fig. 27 and on the fact that the Ru_{cus} surface atom is consistently proposed to be the OER-active site.[1,21]

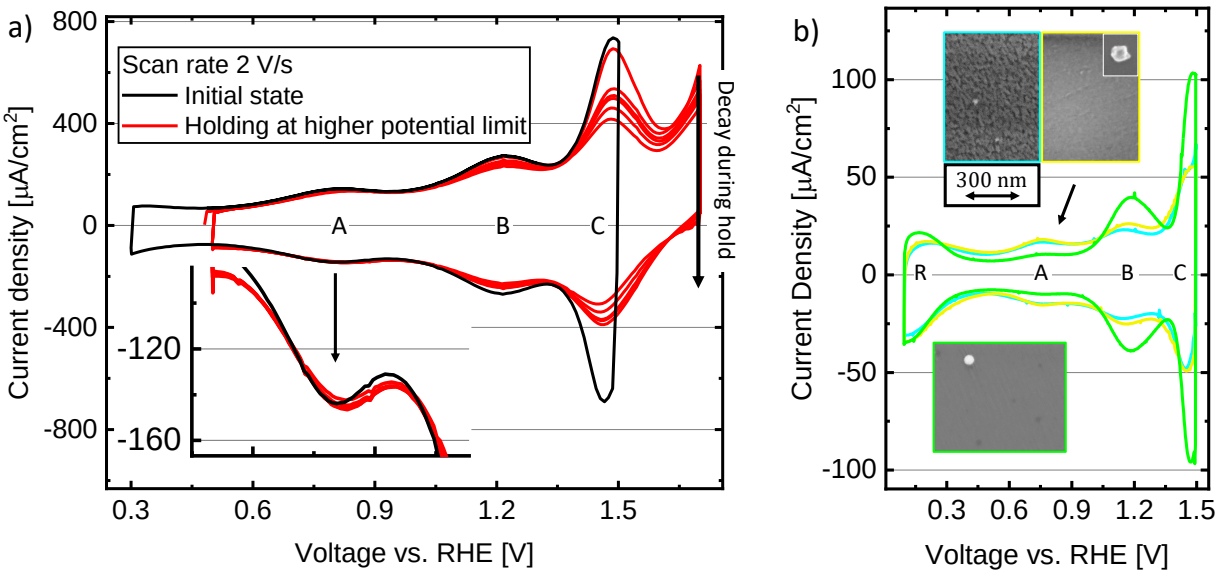

Fig. 28: a) Cyclic voltammograms at $2\,V\,s^{-1}$: The black curve serves as a reference of the fully active surface. The red curve shows consecutive cycles with increasing waiting periods of 1, 3, 10 min at the higher limit ($1.7\,V_{RHE}$) within the OER region. While the surface redox transitions including OER-active O_{ot} sites are affected by the decay, feature A is does not loose amplitude. b) Cyclic voltammetry ($200\,mV\,s^{-1}$) at less quality (light blue and yellow) samples is compared to a flat good quality sample (green). (Fig. 20) All features depend on the surface quality. Feature A is more dominant at the less quality samples.

4.5.8 Surface redox transition A

Rao *et al.*[21,22] interpret feature A as related to a deprotonation of adsorbed water (H_2O_{ot} at Ru_{cus}), while an earlier study attributed feature A to the surface defects and, therefore, to the sample quality.[48] They compared voltammograms of films exhibiting different roughness (checked by STM).

First of all, Rao's[21] model (Fig. 26) proposes that the deprotonation of H_2O_{ot} makes up half of the transition's transferred charge, consequently, the peak is expected to be diminished by this fraction ($1/2$) of contributing O_{ot} species. Fig. 28a) shows the experiment of the preceding section carried to the extremes. This is reached by maximizing the peak signal by means of a scan rate of $2\,V\,s^{-1}$ and waiting for $\{1, 3, 10\}$ min at the high potential limit ($1.7\,V_{RHE}$) in consecutive cycles to also maximize the deactivated fraction of O_{ot} sites. With increasing hold time the deactivation proceeds: While feature B and C are affected in line with the observations in Fig. 27, no significant decrease is visible at feature A. This is a strong hint against Rao's interpretation of transition A including adsorption at O_{ot} sites. A (conceivable) reactivation of the deactivated sites during the negative sweep (after the holding period at $1.7\,V_{RHE}$), which is in fact described in the next chapter (Fig. 31b2)), can be excluded because the positive going sweep still shows (the main fraction) of the induced decay at transition C. Thus, the time spent at lower potentials is not sufficient to reactive the sites during a single sweep. However, as O_{br} is not affected by the deactivation, a transition including solely O_{br} could still be a possible explanation. Nevertheless, none of the theoretical models predicts such a transition near A. (autoreffig:ModelsLiterature)

In addition to literature evidence that contradicts a reaction including sites O_{br} and O_{ot} sites of the ideal surface model (Fig. 25), the CV experiments performed at $200\,mV\,s^{-1}$ shown in Fig. 28b) support Lister's interpretation[48] regarding surface defects, which

are not included in the ideal surface model. Representative voltammograms of one flat good quality (green) and two intrinsically rough (light blue and yellow) samples are shown. They stem from the green, the yellow and the blue category (Fig. 20) respectively, as identified by SEM in subsection 4.1.1 earlier. The charge attributed to the ideal surface model transitions B and C (including O_{br} and O_{ot}) is less compared to the good quality samples. However, more charge contributes to transition A; this would be expected for a higher fraction of defect sites.

One could also raise the question how growing good quality RuO_2(110) films, which do not exhibit feature A, could even be possible if its an intrinsically expected transition for an ideal surface. One of the best investigated samples of this study (regarding minimal feature A) is shown in Fig. 28b) (green) and it only exhibits a very faint peak A. The MBE-grown films[51] shown at the beginning of this section (Fig. 24b)) even seem to exhibit no transition A at all. These observations are supported by the most recent DFT model of Liang *et al.*[91] (which accounts for magnetic ordering), since it predicts no transition within the potential region of peak A at all.

A possible implication could be: either defect sites are not affected because they do not contribute to the OER, or they contribute but are not deactivated as it is the case for O_{ot}. As contributions of defect-like sites are proposed by theory[117] (steps and kinks), but lack experimental evidence[20], this would be an interesting implication. Unfortunately, no conclusion can be drawn at this point. Experiments that search for correlations between the number of defect sites and the decaying OER current could possibly provide further evidence.

Lister *et al.*[48] observed a damped feature A in phosphoric acid (H_3PO_4) compared to sulphuric acid (B unaffected). This hints the adsorption of $H_2PO_4^-$ at defect sites and possibly suggests that reactions A and B do not share the same sites.

Chlorine reduction feature C2 developed with increasing sample history (Fig. 18), which can be attributed to corrosion (evidence in Fig. 38a) and Fig. 36), which would in turn identify the CRR as effective method to probe transition A and imply that defect sites take part in this reaction.

4.5.9 Proposed model based on the presented evidence

Finally, we can draw a conclusion and propose a model that is in line with all observations of this chapter. The final sequence of redox reactions utilizing a three unit cell model of O_{ot} and O_{br} pairs is depicted in Fig. 29. Three unit cells are the minimum needed to match the fractions identified in subsection 4.5.7 and shown in Eq. 60. The model will be described starting from the OER at the higher potential limit. Transferring the attributed site contributions sketched in Fig. 27d1) and described by Eq. 60 to the model, three of four hydrogen adsorption reactions of transition C occur at O_{ot} (left column), while one occurs at O_{br} (right column). Transition B has $^2/_3$ O_{br} and $^1/_3$ O_{ot} contribution. As it has been assumed that all O_{ot} contributed at least once (Fig. 27d1)), overlap within the O_{ot} area) so far, likely an adsorbed water (H_2O_{ot}) is formed. The reversible process accompanying the slower proton incorporation in the reconstruction region R is expected to be the desorption of adsorbed water, exposing a blank Ru_{cus}. An adsorbed water molecule seems to be a reasonable precursor state for this reaction. Furthermore, it would be reasonable that the transformation from HO_{ot} into H_2O_{ot} continues. Feature A is interpreted as simple hydrogen adsorption at a certain type of predominant defect

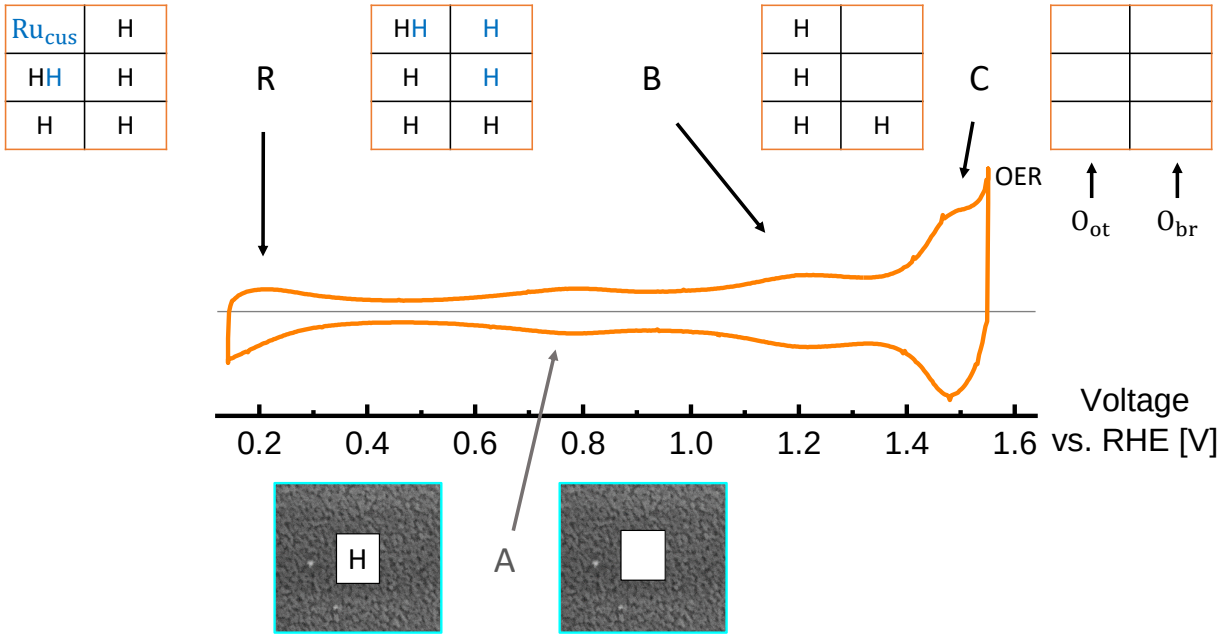

Fig. 29: Proposed model of the surface adsorption reactions R, A, B and C, which are experimentally observed at $RuO_2(110)$. It is based on the experimental observation of the oxygen evolution reaction (OER) current decay, which is in line with the decrease of feature B and C (Fig. 27) as all three processes rely on the O_{ot} species. As feature A depends on the sample quality it is attributed to a defect-site related transition. The general conceived surface structures are based on the literature (Fig. 26). The transition of R is proposed[89,91] and in line with the observation of chlorine reduction feature C3 (Fig. 18).

site (step, kink, vacancy etc.) that seems to commonly appear at rougher (110) surfaces. It seems to behave independent of the ideal unit cell reactions.

The intuitive interpretation from the literature[21] that C provides active sites for the OER, which in consequence starts to rise during this transition, is in line with this model and fits the observed current density. The transition during R to a surface containing blank Ru_{cus} would be consistent with the models of Sumaria[89] and Liang[91] shown in Fig. 26. Moreover, this is in line with the interpretation of the chlorine reduction feature C3 proceeding over a Ru_{cus} site as discussed in subsection 3.5.2.

Overall, the preceding sections allowed to exclude several theoretical models proposed in the literature: Exner *et al.*[34] as they propose solely bridge transitions during B and C, Kuo *et al.*[49] as they propose bridge only and on-top only. Rao *et al.*[21] and Liang *et al.*[91] propose half bridge, half on-top, at B, which yielded an insufficient fit (Eq. 59) but approximates the observed situation – still, both models predict C wrong. But, utilizing the knowledge from the literature about the variety of surface transitions that would be in principle possible, a own model could be proposed based on a novel application of CV that enabled this study (Fig. 27). The important conclusions are the confirmation of Lister's[48] claim that A is related to defect sites and the identification of the specific fractions of O_{ot} and O_{br} contributing to B and C. This type of study, which utilizes the deactivation of O_{ot} during the OER to draw conclusions about the surface redox transitions, is ready to be applied to freshly grown thin films to investigate their surface reactions.

5 Characterization by Standard Protocol

The following chapter aims to identify trends in the electrocatalytic properties among the available samples by means of a standardized characterization protocol. The protocol is utilized to probe the peak charges and widths associated with the surface redox transitions, which were identified in the preceding chapter. The OER activity is determined by the Tafel parameters from a logarithmic current-voltage characteristic as discussed in section 1.2. To enable a reliable Tafel analysis, the observed deactivation of OER-active sites (Fig. 27) is investigated and modeled first. The Tafel parameters are found to depend on the sample's corrosion history. Furthermore, it is possible to distinguish the flat samples from the less quality samples in line with the prior SEM categorization from Fig. 20.

5.1 Validity of linear sweep voltammetry for Tafel analysis

5.1.1 Observation of hysteresis in the oxygen evolution polarization curve

As discussed at the very beginning of section 1.2, the key figure of merit to investigate the OER mechanism is the Tafel slope of a logarithmic (linearized) current-overpotential plot. The second parameter of interest is the intersect of the Tafel line with the current axis at the water splitting standard potential ($E^\circ = 1.23\,\mathrm{V_{RHE}}$[8]): This yields the exchange current density, which contains the free energy of the transition state of the current rate-determining step (RDS) (section 1.2). This is common practice in the electrocatalysis community. In addition, Tafel plots are used to determine the *overpotential* (at a fixed current density) to judge the sample's activity. While this method may be quite pragmatic to judge the actual catalytic current a sample can provide, and even be quite useful from an applied point of view, it washes out all information about the reaction mechanism. When Tafel plots in general (including activity and slopes) are of interest, the usual recommendation found in the literature is to perform linear potential sweeps as slow as possible; sometimes with the additional note to increase the potential step size (i.e. staircase voltammetry).[103,118,119] While this may yield sufficient results in most cases, there are strong hints that the usual procedure is not applicable to RuO_2, which will be presented in the following section.

If one looks closely at the CV data of RuO_2, it becomes evident that a more sophisticated approach to determining Tafel parameters is required: Fig. 30a) shows representative measurements in contamination- and chloride-free 1 M H_2SO_4 electrolyte. Qualitatively equivalent observations have been made for all of the investigated thin films, therefore, the following discussion of the observed activity decay claims to be a general feature of RuO_2(110) thin films. Fig. 30a) shows a CV experiment at a comparably slow

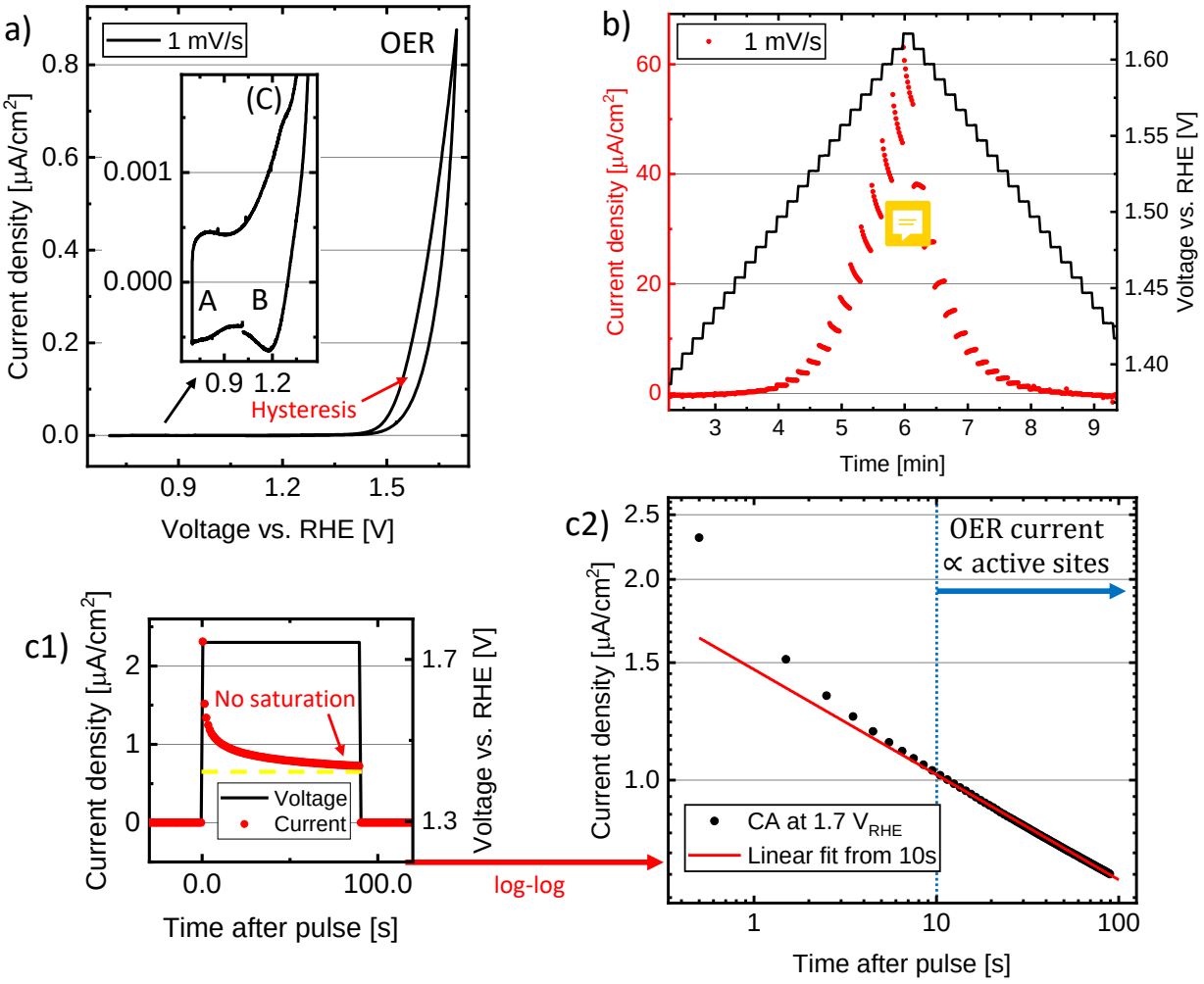

Fig. 30: a) Cyclic voltammogram recorded at $1\,\mathrm{mV\,s^{-1}}$, which exhibits a considerable hysteresis in the oxygen evolution reaction (OER) region. The surface redox transitions appear suppressed due to the slow scan rate. b) Staircase voltammetry (SV) performed at $1\,\mathrm{mV\,s^{-1}}$ with a step size of 10 mV. After each voltage step the current decays by different amounts until the end of a step. A trend reversal is observable in the reverse scan. The decaying current is interpreted as a loss of OER-active sites. c1) A chronoamperometric pulse of 90 s at $1.74\,\mathrm{V_{RHE}}$ is applied after holding at a rest potential of $1.30\,\mathrm{V_{RHE}}$. c2) The same current as in c1) is plotted double logarithmically. A linear region pointing towards a polynomial decay law can be observed from 10 s onward.

scan rate of $1\,\mathrm{mV\,s^{-1}}$ within the potential range of the OER (and below). The magnified inset shows the surface redox features A and B; since their peak current scales linearly with the scan rate, the associated currents are accordingly small. As the onset of peak C overlaps with the OER onset, this feature only exhibits a shoulder at the rising current. This is a continuation of the trend that has already been observed in Fig. 24d) while discussing the scan rate dependence of the RuO_2 cyclic voltammogram.

The striking observation is a considerable hysteresis in the anticipated steady-state sweep. While the small hysteresis in the lower potential region is caused by a combination of surface redox transitions and double-layer charging, the OER region does not follow the expected exponential behavior according to the generalized Butler-Volmer equation (Eq. 7). Consequently, the system knows about its history and the observed behavior has to be implemented into the model (and understood) to allow for a sensible

interpretation within the transition state theory (TST) framework. The preceding chapter showed that a time-dependent deactivation of O_{ot} sites, which catalyze the OER, is in line with the expected decay of peak C. Since this is, by far, not the only conceivable mechanism that could cause such a decaying current, the next section will discuss in detail what leads to this conclusion. But firstly, the experimental observations are presented.

As mentioned earlier (Fig. 9a)), a linear sweep is approximated by a digital staircase of the potentiostat. In Fig. 30a) the current is averaged over the intrinsic step size of 100 µV. Subsequently, ten current steps are averaged to yield an apparent 1 mV resolution. To visualize the intrinsic current decay, which happens after each step, the step size is increased to 10 mV and the whole time dependent current is plotted in Fig. 30b) starting from the OER onset ($\approx 1.35\,V_{RHE}$) up to $1.64\,V_{RHE}$. Each step is held for a period of 10 s. Firstly, the absolute and the relative current decay after each step varies during the positive going sweep. Secondly, on the reverse sweep, this trend reverses until even a small rise of current upon decrease of the voltage becomes visible back at lower potentials. The described decaying behavior of Fig. 30b) shows the same hysteresis as observed in Fig. 30a). Furthermore, a current-potential plot would strongly depend on the way the current associated with a certain potential step is chosen, i.e. after which time the current is read or which range is averaged. This outlines an important problem for the Tafel analysis: The current overpotential plot depends on the chosen readout time and the scan rate. These observations imply that the *speed* of the decay mechanism (more precisely quantified in subsection 5.1.3 as a polynomial decay constant) increases with increasing applied potential on the one hand, and decreases with the absolute time spent at elevated potentials on the other, since it decays when the potential is held constant during a step. The dependence of the decay constant to the applied potential explains the increasing current slopes in the forward scan.

As a result, Tafel plots obtained by linear sweeps strongly depend on the chosen scan rate since each point includes the historic response of the preceding points. Furthermore, the amount of expected decay depends on the time spent at each specific potential, because it does not follow the same behavior over the whole range. To enable for a less qualitative description of the observed deactivation process, the complexity of the experiment has to be reduced. Therefore, Fig. 30c) shows the current response to a voltage step from a rest potential ($1.29\,V_{RHE}$), up to $1.73\,V_{RHE}$ where a reasonable OER related current establishes. At the rest potential of $1.29\,V_{RHE}$, less electrochemical processes are expected as it is located to lower potentials of the OER and in between redox transitions B and C.

Observing currents at constant potentials is commonly called chronoamperometry (CA). At first glance, it seems as the current would approach a steady state value. This has been extensively tested by extending the time period of a single staircase voltammetry (SV) voltage step up to an hour, which lead to experiments lasting 60 h. In addition, a single step has been held for up to 6 h; and the current never exhibited a saturating behavior. This behavior is in line with a polynomial decay, which is confirmed by the double logarithmic current-time plot shown in Fig. 30c). Within the first 10 s, the current does not decay according to a simple relationship. This perfectly fits the observation from the preceding chapter regarding the proportionality of redox feature C to the (decaying) OER current, which is shown Fig. 27c). The conclusion was that a high active site coverage boosts the OER activity via nearest neighbor interactions. After this initial

phase, the OER current is expected to be proportional to the contributing active sites. This depletion proceeds in a polynomial manner; and therefore, enables us to correct for the observed current decay. The full quantitative description over the whole potential range is based on this observation and will be presented in subsection 5.1.3.

5.1.2 Reversible deactivation of active sites: Possible mechanisms and experimental evidence

On our path to deriving the Tafel parameters, we will try to understand what mechanism causes the loss of OER activity and how it can be controlled. This will eventually lead to an empirically motivated quantitative description of the decaying OER current.

Fig. 31a) shows the current response to 19 consecutive potential steps from a neutral rest potential of 1.35 V_{RHE} (below the OER) to 1.70 V_{RHE} (in the OER region); the lower rest potential as well as the OER pulse are each applied for 5 s. The initial state of the first hold at the lower potential of 1.35 V_{RHE} is a partly inactive surface, which is reached by a preconditioning at the higher OER potential of 1.70 V_{RHE} for 180 s. The overlapping data set of a) is taken from the first set of measurements in Fig. 31c) (dark green). The 19 shown curves nearly overlap, which proves that even on the time scale of 5 s at the lower recovery potential and 5 s in the OER region, the mechanism is reproducible and readily reversible. The formation and spontaneous dissolution of large (observable) bubbles that would be capable of blocking about half of the surface to cause the activity decay from above 400 $\mu A\,cm^{-2}$ to below 200 $\mu A\,cm^{-2}$ would take a longer period of time and are incompatible with the observation. Bubbles of this size were observed to stay adsorbed over days and not noticeably dissolve into the electrolyte.

An intuition that can be checked is the following: If the process can be reversed at a recovery potential near the OER onset (1.35 V_{RHE}), the restoring of active sites could be even more efficient for lower recovery potentials. The experiment shown in Fig. 31b) is similar to the one discussed in the last chapter, where feature C was used to estimate the fraction of sites left active while observing the simultaneous OER current decay. This time, the scan is performed at 100 $mV\,s^{-1}$ and the potential window is set so that a sufficient amount of peak C is included to enable an estimation of its peak current. Initially, the surface is deactivated by prolonged CV between 1.70 V_{RHE} and a lower potential near peak B at 1.1 V_{RHE}; the last cycle of this series is depicted. The current decay during potential cycling was already utilized in the preceding chapter in Fig. 27. After reaching the deactivated state through cycling in the OER region, most of the OER region is excluded (from peak C) to avoid triggering the activation process again. We remember that the peak current of C is correlated to the OER active sites. Therefore, it can be utilized to probe the deactivation. Then, the restore potential is lowered stepwise every 3 consecutive cycles to $\{1.10, 0.90, 0.70, 0.50, 0.30\}$ V_{RHE}. The dominant parameter that instantly shows a clear regain of active sites is the chosen recovery potential, which represents the lower limit of the voltammogram. This is highlighted by the increase of peak C in the magnified view of Fig. 31b2).

Fig. 31c) further investigates the influence of the restore potential under more controlled, less dynamic, conditions. Cyclic step chronoamperometry (CSCA) is utilized by periodically switching from a high OER potential (1.70 V_{RHE}) to different restore potentials ($\{1.35, 0.90, 0.50, 0.20, 0.50, 0.90, 1.35\}$ V_{RHE}) every 5 s. Consequently, 5 s are spent at the higher and 5 s are spent at the lower potential alternatingly. The initial state is

reached after holding 180 s at the high OER potential (1.70 V_{RHE}) and each set of lower potentials is repeated 19 times – the lowest one 37 times. The depicted experiment illustrates two points: At first, it further confirms the conclusion about the reproducibility from Fig. 31a) as for all tested recovery potentials the current seems to quickly approach a defined steady state decay curve. More precisely, after some initial 5+5 s periods the overlap of the consecutive 5 s OER pulses would increase when plotted versus the time after the pulse as illustrated in Fig. 31a). Secondly, the readily recovered fractions of the surface become larger the lower the restore potential is. This can be judged by the first (and highest) point in the OER pulse after a recovery phase (Fig. 31b)). This confirms the observation of the CV experiment in Fig. 31b), which also suggests more reactivated surface at lower recovery potentials. Here, the fraction of the active surface is assumed to be positively correlated with the OER current. This assumption is justified by the preceding chapter (Fig. 27c)).

Reversing the sequence of recovery potentials by choosing more positive lower potentials inverts the trend. This time, it becomes evident that the decay at high potentials is happening more slowly relative to the decay seen before reversing the sequence of recovery potentials – i.e. the inverted experiment shows that the decay seems to reach its steady state value more slowly. Furthermore, the last decay series (highest lower potential, 1.35 V_{RHE}) does not decay down to the same current that was reached by the first sequence (at the same recovery potential).

A further similar experiment (not shown) revealed that changing the CSCA duty cycle also affected the amount of the restored current as well as the time to reach the steady state. Spending 5 s on the high potential and 10 s at the lower potential (instead of 5 s as in the earlier experiment) results in overlapping chronoamperograms, basically from the first cycle onward after an initially decayed state. The amount of restored current also slightly increased with a smaller duty cycle (meaning longer recovery periods), but, probably less than lowering the restore potential by about 0.2 V would yield. Even when choosing the recovery period as low as 0.1 s before applying an OER pulse of 5 s is sufficient to yield qualitatively the same behavior – yet the amount of restored current decreases.

Up to this point, we have discovered the deactivation process of OER-active sites to be reversible. The fraction of recovered surface depends on the time spent at a lower recovery potential that can be located anywhere below the OER region (about 1.5 V_{RHE}). Furthermore, the recovery of the surface seem to be more efficient, i.e. more sites are restored, for lower recovery potentials.

An objection at this point would be that the largest potential step includes more capacitive charging of the double layer as well as all three (or four, including the reconstruction feature R) redox transitions. An estimation of the upper limit of the decay constant accompanied with these processes is possible by assuming an RC series circuit. The series resistance was determined to be $(59 \pm 1)\,\Omega$ (EIS) and the overall capacitance of all transitions plus the double-layer capacitance (DLC) amounts to $(12 \pm 1)\,\mu F$ (CV and EIS averaged; calculated by $C = Q/U$ with the whole transferred charge Q divided by the potential width U covering redox features A, B and C; DLC added). The resulting time constant of $\tau = RC = (0.72 \pm 0.06)$ ms implicates that the charging currents should not play a significant role anymore from the second data point – at an acquisition rate of 100 ms. Therefore, the observed high currents at the lowest recovery potential are interpreted as actual increased OER activity.

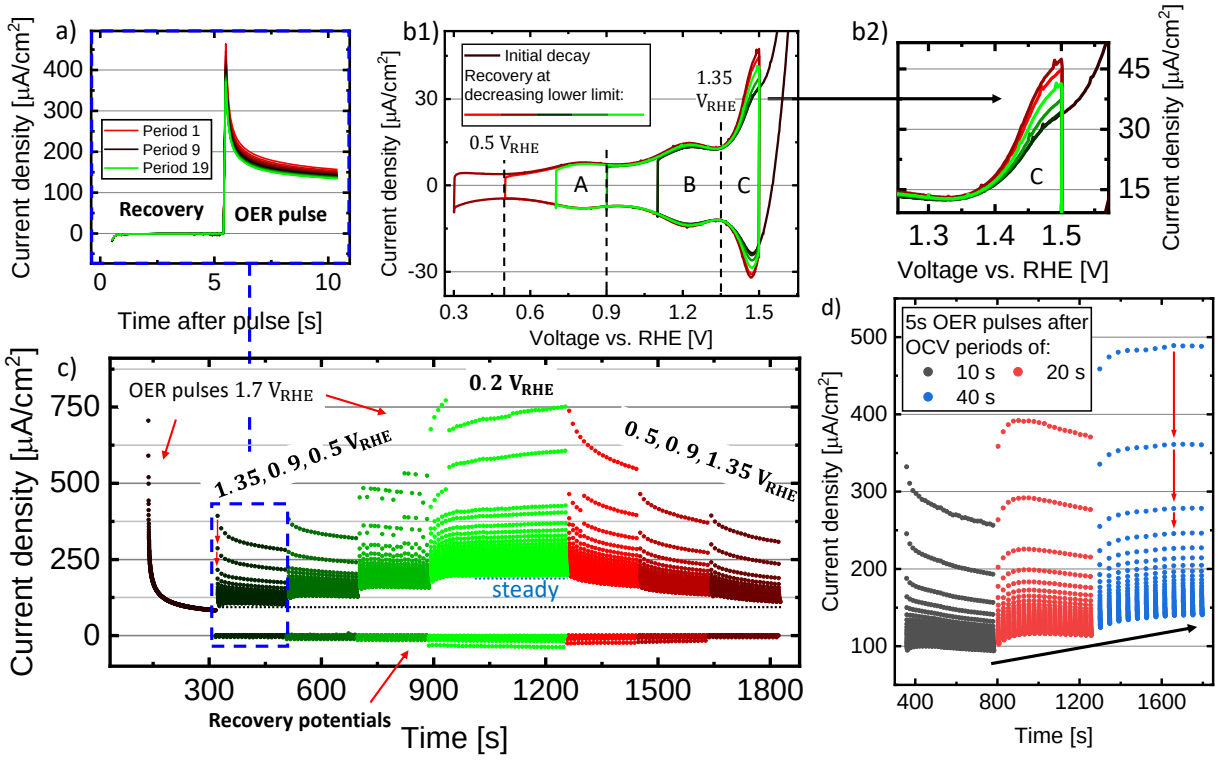

Fig. 31: a) Consecutive 5 s chronoamperometric holds at a recovery potential of 1.35 V_{RHE} and an 5 s OER pulse at 1.70 V_{RHE}. The decay curves overlap well. b1) Recovery from initially decayed state (black) probed by cyclic voltammetry at 100 mV s^{-1}. The magnified view in b2) highlights that lower potential limits result in more regained active sites as judged by the increase of peak C. c) Cyclic step chronoamperometry (CSCA) after 180 s of preconditioning at the OER potential of 1.70 V_{RHE}. The colored points show 5 s OER pulses at 1.70 V_{RHE} with 5 s holds in between at different recovery potentials ($\{1.35, 0.90, 0.50, 0.20, 0.50, 0.90, 1.35\}$ V_{RHE}). The amplitude of the decay current depends on the recovery potential. The downward step carries historic response compared to the upward step at the beginning. d) The same measurement as in c), but instead of holding at a recovery potential the circuit is opened for $\{10, 20, 40\}$ s and the open-circuit voltage (OCV) is measured (not shown). The longer the circuit is opened the more OER activity is regained.

Fig. 31d) also investigates different active-restore duty cycles ($^5/_{10}$ s, $^5/_{20}$ s, $^5/_{40}$ s), but in this case the high potential is interrupted by opening the circuit and measuring the OCV. The remarkable observation here is that the recovery of the surface also proceeds spontaneously during the OCV drop, as well as the consecutive chronoamperograms, and is very reproducible. The OCV of this sample always approached 0.8 V_{RHE} directly after immersion or after waiting for a steady state following experiments (in cases where no chloride is involved). This is a possible hint that the surface that is stable around this potential will spontaneously recover, since it would be expected to be energetically most favorable in an acidic environment of 1 M H_2SO_4. A possible candidate would be the hydrogen saturated surface with a fractional coverage of adsorbed water as shown in Fig. 29 between transition R and B. This implies that whatever deactivates the active Ru_{cus} would also be reversed. Therefore, applying an additional (negative) bias to speed up the spontaneous recovery process is sensible.

By now, the most important experimental observations of the OER current decay that generate an intuition are outlined and we can proceed to exclude conceivable mechanisms based on this evidence. The first thing that is checked relates to the discussion of

the current response to a potential step from subsection 2.4.1. As exponential capacitive currents have already been excluded, the inverse square root decay (over time) from the Cottrell equation (Eq. 38) seems promising. This decay is expected for a diffusion limited solution species process at semi-infinite planar boundary conditions. Therefore, the depletion of available reactant in the vicinity of the electrode limits the kinetic current. Since this limiting current I_{lim} only impacts the overall current I in case the kinetic current I_{k} exceeds it, there will be a transition between a kinetically and diffusion controlled regime depending on the applied potential. This is described by the Koutecky-Levich equation[120]:

$$\frac{1}{I(\eta)} = \frac{1}{I_{\mathrm{k}}(\eta)} + \frac{1}{I_{\mathrm{lim}}}, \tag{61}$$

where η is the applied overpotential of a Butler-Volmer like process. The equation is analogous to the connection of two conductances in series – because the conductance is the quantity that is proportional to the currents predetermined by the chemical processes. Assuming $I_{\mathrm{lim}} \propto 1/\sqrt{t}$ enables to plot $1/I(\eta,t)$ against $\sqrt{t}$ for each η and check for this behavior. The intercept at $\sqrt{t} = 0$ would directly yield $1/I_{\mathrm{k}}(\eta)$ for each overpotential, which would in turn lead to the desired Tafel plot. This procedure was tested on all of the characterized samples. Assuming the predicted $t^{-1/2}$ clearly does not linearize the data, we attempted to optimize the exponent for best linearity (around $t^{-1/4}$), but still, it was not possible to fit the whole potential range and the resulting Tafel plots appeared to depend strongly on the assumed exponent. Consequently, the Koutecky-Levich like behavior in general can be excluded.

To get more confidence in excluding a mass transport limited current, a rotating disk electrode (RDE) experiment was designed in cooperation with the Institute of Geological and Nuclear Science (Wellington, New Zealand). The availability of this setup in New Zealand allowed to cross-check the observed decaying current at polycrystalline RuO_2 samples. In brief, the WE is rotated to induce an electrolyte flow toward the electrode. This counts among the commonly called forced convection techniques. The limiting current is influenced by adding a further convective component to the formerly diffusion controlled mass transport. It is common practice to investigate diffusion limited solution species processes at various rotation rates ω and extract the kinetic current by plotting Eq. 61 against $I_{\mathrm{lim}} \propto \sqrt{\omega}$.[120]

Here, we compare a normal pulse voltammetry (NPV) experiment recorded in a quiescent 1 M H_2SO_4 electrolyte to another one recorded at a rotation rate of 1600 rpm. The WE material is a polycrystalline RuO_2 powder, which is demobilized at a glassy carbon (GC) disc by a 5 wt % Nafion solution (which offers protonic conductivity and acts as an inert glue) – essentially the material of the proton-exchange membrane of the PEM fuel cell discussed in chapter 1. The plots presented in Fig. 32a) are taken from the typical characterization protocol (discussed in 5.2). Since these samples are more prone to corrosion than the single crystalline films (judged by changes of the CV response and OER activity before and after the protocol), the rotated and quiescent data are taken from two consecutive runs of equally prepared electrodes. Fig. 32b) shows the initial CV response of both utilized electrodes at 200 mV s^{-1}. The electrode material is the same nanoparticulate RuO_2 that was already shown in Fig. 24a). The voltammograms of both investigated samples nearly overlap without normalizing, which indicates a similar ECSA and also proves their chemical comparability.

NPV will become the most important technique that aids in investigating the OER kinetics by means of a Tafel plot. Its main advantage compared to SV (or linear sweeps in general) is that *it eliminates all historic responses, which are introduced via the decay process*, by switching to a recovery potential before each potential step into the OER region. The scan parameters of this and all NPV experiments discussed in the following are 10 mV step size, a pulse time of 90 s, an active/restore-duty cycle of 1/2 and a current acquisition rate of 1 Hz. By plotting the experiment against the time the activity and the decay can be judged simultaneously.

The two experiments in Fig. 32a) show very similar activity and decay behavior independent of the rotation rate. While this firstly hints at the observed deactivation to be not restricted to the single crystalline thin films, it moreover excludes all diffusion related processes – as the rotation drastically varies the mass transport conditions.

This is, as expected, in line with the oxygen evolution process as it basically involves water as reactant – which is omnipresent. A diffusion limit would be therefore hardly imaginable. In addition, there is a RDE study at polycrystalline Pt, which shows that there is no mass transport induced current limitation within the OER region in acidic electrolyte.[121] This study[121] furthermore investigates the diffusional current limitation of the HER, where H^+(aq) ions serve as reactants. This was only possible within a highly diluted electrolyte (pH 2.55) as they did not observe a current limitation at pH 1. As a result, increased local acidity due to an insufficient proton removal, which would also cause the OER current to decrease, is not expected. Since the RDE experiment at RuO_2 should also influence a possibly limited H^+(aq) removal, the expectation is confirmed.

Following the exclusion principle, the next candidate for the observed current decay in line would be the produced oxygen. A study by Garcia *et al.*[122] at polycrystalline platinum confirmed that under rotated conditions (1600 rpm) there is no difference in the OER activity comparing O_2-free and O_2-saturated acidic or alkaline electrolyte. Nevertheless, they observed a difference without rotation, which they attributed to the insufficient removal of adsorbed oxygen bubbles in this case. This leads from dissolved oxygen to oxygen bubbles as a possible candidate to explain the current decay.

While the final conclusion is approached, it is important to note that there is a recent scientific dispute about the mechanism behind a similar behavior, which is observed in IrO_x. The two contradictory mechanism are: deactivation of active sites and blocking of the active surface by oxygen bubbles. The discussed material system is also referred to as hydrous iridium oxide as it contains a certain amount of hydrogen. One way to obtain these materials is to electrochemically oxidize Ir nanoparticles or discs at positive anodic potentials. Nevertheless, the observations made at these materials closely resemble the described situation of RuO_2. Even a polynomial decay ($t^{-1/4}$) has been reported once by Tang-Kong *et al.*[123]. The CSCA measurements performed in this thesis Fig. 31 are inspired by this publication[123] and can qualitatively confirm all trends which were previously reported for IrO_x. Tang-Kong *et al.*[123,124] and another group[125] both claim to observe a progressive loss of active sites, which is reversible in a comparable manner as in the case of RuO_2. They basically propose a transformation of hydrous IrO_x toward less active dry IrO_2 (meaning less hydroxide species), which is accompanied by a change of the active Ir-site's oxidation state. That this effect is in fact still observed at the presumably least active RuO_2 phase, provides evidence that demands for a slightly different mechanistic plausibility check.

Later, Hartig-Weiss *et al.*[126] directly addressed both mentioned interpretations[123,125]

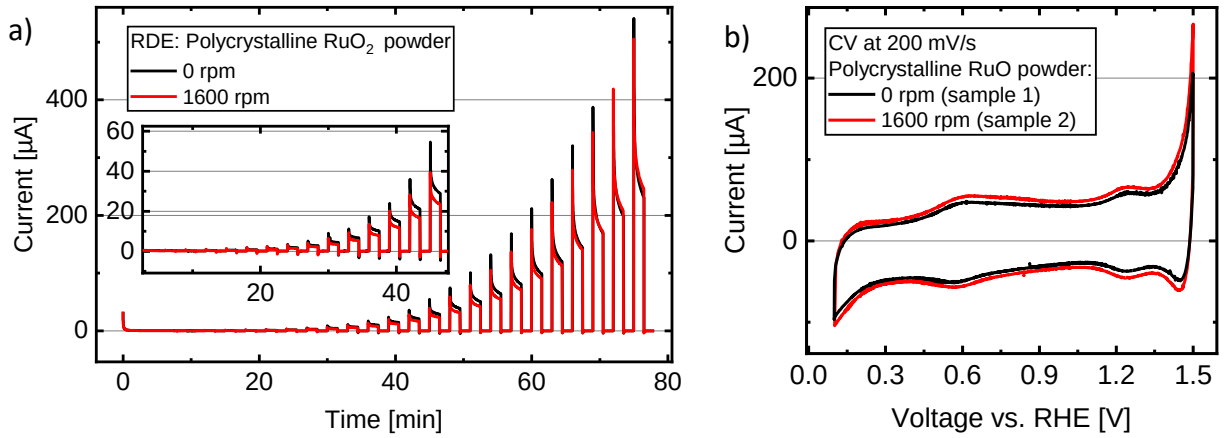

Fig. 32: a) Normal pulse voltammetry experiment ranging from 1.36 V_{RHE} to 1.71 V_{RHE} in 10 mV steps with 5 s OER pulses and 5 s at a recovery potential of 1.36 V_{RHE}. Both polycrystalline RuO_2 electrodes were prepared equally and their comparability is proven by cyclic voltammetry (CV) at 200 mV s^{-1} in b). The experiment is performed utilizing a rotating disc electrode (RDE) at quiescent conditions as well as at a rotation rate of 1600 rpm. The decaying current behaves similar in both situations and is not affected by the varied mass transport conditions.

and claimed to have provided solid evidence for the predominant decay mechanism being adsorbed microbubbles. In fact, their experiment utilizing an oxidized polycrystalline Ir RDE is quite convincing. They observe the decaying current even at rotations rates of 2500 rpm, where all larger bubbles should usually be cleaned of by the induced convection. As a result, microbubbles are proposed, but not defined in greater detail. Therefore, they introduce an ultrasonication horn to their experiment, which is able to eliminate the decay (and introduces additional noise in the measured current). This is attributed to the ability of ultrasonication to destabilize even the bubbles that can not be removed solely by rotation. As traces of microscopic bubbles (many below 1 µm of diameter) are even observed via SEM in the present case (see Fig. 37b)).

While this mechanism could explain the qualitative behavior up to a certain degree it does not yet deliver a reasonable explanation for the reported[123] and observed potential dependence of the surface reactivation. On the one hand, bubbles would be in line with the observation of an OCV period being able to restore the activity (Fig. 31d)). On the other hand, more complex processes would be needed to explain the influence of the restoring potential. ORR driven bubble removal can be excluded as this would not occur spontaneously, and even does not proceed at a reasonable current through an applied overpotential at RuO_2.[14] A further guess would be a surface termination induced change in the hydrophilicity, which would in turn utilize the bubble-surrounding water to clean them off through the increased attraction.

The preceding discussion underlined that microbubbles as well as surface deactivation are both mechanisms which could reasonably be used to explain the observed current decay. The possibly final pieces of evidence against a surface shadowing effect induced by any size bubbles are presented in Fig. 27a,b) and Fig. 28a). These experiments, which probed both the OER activity decay and the surface redox features including the underlying double-layer charging current, clearly showed that the cyclic voltammogram is affected disproportionally. Blocking a certain fraction of the surface by a bubble would rescale the current by the same fraction equally for each potential (this point was also brought up in section 4.5 in relation to Fig. 27a,b) and Fig. 28a))

As we have shown in the preceding discussing, it has been possible to exclude a variety of alternative explanations for the current decay, namely: charging currents by an estimation of their time constant, a Cottrell-like mass transport limit by RDE measurements, checking for the Koutecky-Levich equation and evidence from the literature, local acidity (a proton diffusion mass transport limit) is consequently also excluded, oxygen saturation by the literature, large adsorbed bubbles by RDE and microscopic (referring to Hartig-Weiss*et al.*[126]) bubbles by an experiment that showed a disproportional current decrease within the voltammogram. The final conclusion is that the transformation of OER-active Ru_{cus}-sites into OER- and surface redox- inactive sites causes the observed reversible current decay.

Only guesses about the actual nature of these deactivated sites can be made. A recent theoretical study[127] proposed an interplay of the OER and RuO_2(110) surface corrosion. They identified the corrosion process to proceed via an adsorbed (and temporarily stable) RuO_2OHO_{br} species by an ab initio molecular dynamics (AIMD)-based approach. This species originates from a formerly active Ru_{cus}-site and exposes a fresh Ru_{br}-site underneath. As this study assumes an ideal RuO_2(110) surface care has to be taken while interpreting these results. Nevertheless, it motivates that at least a process of this type could exist and could probably also be generalized to explain the observations at the polycrystalline RuO_2 electrode. Since the timescale of the activity decay is clearly longer than the typical timescale of a potential dependent surface restructuring by a PCET or adsorption of an $O_{ot}OH_{ads}$-species (as proposed by Exner *et al.*[34] at elevated potentials; also see Fig. 26), a more complex process including a surface corrosion intermediate seems to be most reasonable. Restoring the surface could either happen by desorbing the intermediates and exposing fresh surface or reincorporation into the crystal lattice.

5.1.3 Empirically motivated quantitative description

By now, all observations can be rationally explained in a qualitative manner: The current decay is present in the OER region, the surface can be recovered more effectively at lower potentials and the deactivation process is reversed spontaneous at the OCV. The mechanism that causes the OER current decay is likely correlated to a loss of active O_{ot} sites (subsection 4.5.7). Utilizing NPV experiments it seems also possible to (at least partly) disentangle the deactivation process and the actual oxygen evolution reaction (OER), the latter of which is important to isolate for the desired Tafel analysis.

A quantitative description is based on the observed linear decay behavior within the double logarithmic current-time plot at a fixed overpotential shown in Fig. 30c). As previously described, the OER current starts to become proportional to the fraction of sites left active after an initial phase of about 10 s. The disproportional decay before 10 s seems to be a reproducible, yet unpredictable, process that follows no simple exponential or polynomial behavior. Since the aim of this comparative study is to find a robust metric, which can be applied to a variety of slightly different thin films, the linear region will be utilized for this purpose; as it is observed for all samples and behaves in an identical polynomial manner. This additionally allows for choosing a readout time with the decay – the decay exponent d of the current decay depends on the potential. to each potential – has happened for a defined period of time. Otherwise, during the fast initial decay, which seems to follow no general law, the choice of a readout time would

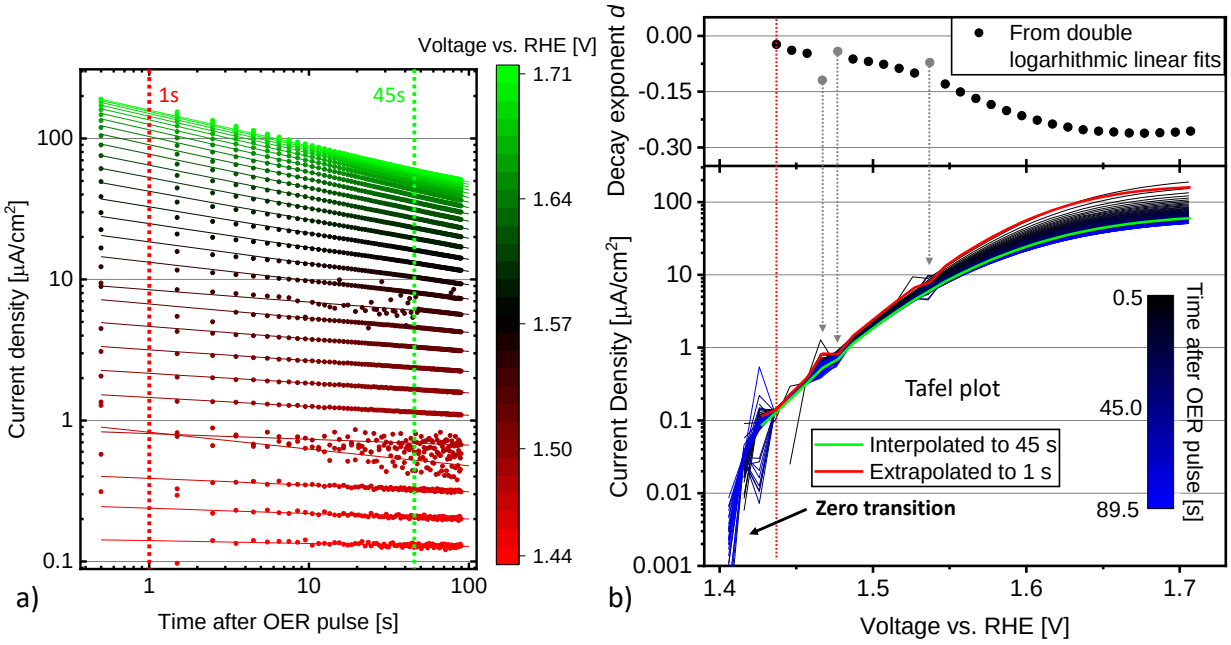

Fig. 33: a) Current decay curves extracted from a normal pulse voltammetry (NPV) experiment. The log-log plot reveals a polynomial law with potential-dependent decay exponents according to Eq. 63. Lines are fitted to extract slope and the intercept 1 s after the OER pulse. b) The resulting parameters from a) for the decay exponent d and the Tafel plot created from the current intercepts of the linear fits after 1 s(red) as well as 45 s(green) are plotted versus the potential. All raw data of the NPV experiment are shown colored after the time after which they were read from black to blue. Decay exponents resulting from unstable measurements are indicated gray – this also influences the resulting Tafel plot. The strong rise of the current near 1.4 V_{RHE} is caused by a preceding zero transition of the current.

be rather arbitrary taking into account that there is no evidence that all samples behave equally. In contrast, the linear region of the double logarithmic plot always contains the key parameters of the deactivation process within its slope and the key parameters of the activity within its offset. This is demonstrated now.

Based on the observations, the overall current density j can be approximated by an activity factor A, which is diminished proportional to the current fraction of active sites $\Gamma(t)$ at time t. I propose the following model:

$$\begin{aligned} j(\eta, t) &= \Gamma(t) \cdot A(\eta) \\ &= \left(\frac{t}{t_0}\right)^{d(\eta)} \cdot j_0^{\mathrm{RDS}} \exp\left[\frac{\beta_{\mathrm{RDS}} e\eta}{kT}\right]. \end{aligned} \tag{62}$$

The activity factor A is expected to behave according to the Tafel equation (Eq. 8) at sufficiently high overpotentials, with exchange current density j_0, electron transfer coefficient β, electron charge e, Boltzmann's constant k, temperature T, which depends on the overpotential η measured relative to the reversible water splitting standard potential $\eta = E_{\mathrm{RHE}}^{\mathrm{measured}} - E_{\mathrm{OER}}^{\circ} = E_{\mathrm{RHE}}^{\mathrm{measured}} - 1.23\,\mathrm{V}$. The 'RDS' label indicates properties of the rate determining step at the investigated overpotential. The decay $\Gamma(t)$ is modeled by a polynomial overpotential-dependent decay exponent $d < 0$ and the divergence at zero time is removed by introducing a relative time scale via t_0.

The whole NPV experiment consists of a series of 90 s voltage pulses ranging from 1.366 V_{RHE} to 1.706 V_{RHE} applied in steps of 10 mV. Before each OER-pulse the potential

is held at a recovery potential (1.366 V_{RHE}) for 90 s. One representative experiment of a fresh (first electrochemical measurement run), good quality (green category SEM of subsection 4.1.1, which is consistent with prior RHEED categorization[27]) RuO_2(110) thin film in 1 M H_2SO_4 is shown in Fig. 33. The double logarithmic representation of Eq. 62 yields:

$$\log\left[j(\eta,t)\right] = d(\eta)\cdot\log\left[\frac{t}{t_0}\right] + \frac{\beta_{RDS}e}{kT}\eta + \log\left[j_0^{RDS}\right] \tag{63}$$

The experimental data can be fit by lines of slope $d(\eta)$ from about 10 s onward as shown in Fig. 33a). Before relevant OER currents establish, the current-voltage characteristic usually shows a zero transition before it clearly rises – only the positive currents are shown in the logarithmic current plot in Fig. 33b)) This causes a divergence of the logarithmic current and sets limits to the range of valid data points. The Tafel equation predicts an exponentially rising current at sufficient overpotentials. In addition, since there is always a small background current before the onset, data points are invalid (for Tafel analysis) before the OER current gets predominant either way. A further problem of the measurement are spontaneous instabilities of the potentiostatic control cycle, which can be identified as widely spread points in Fig. 33a). These are not caused by the ohmic drop compensation or the automatic current range setting. No sources of external noise could be identified. Decay curves showing control cycle instabilities are excluded from the Tafel analysis. Eq. 63 illustrates that the applied overpotential offsets the lines, which all exhibit a slope of the decay constant d. The discussed trend toward higher (than linear extrapolated) initial currents within the first 10 s develops with increasing potential. It can be observed near the early points (<10 s) of Fig. 33a) as they lie below their fit lines in the lower potential region.

The offsets, which contain the kinetic information of the OER, resulting from the depicted linear fits are presented as a logarithmic current-voltage characteristic in Fig. 33b). We will refer to this type of graph as Tafel plot from now on. The top part of Fig. 33b) shows the potential dependence of the decay exponent $d(\eta)$. The decay seems to become more dominant with increasing potentials as the absolute value of d increases. The points determined from oscillatory curves are indicated in gray. The induced noise is also visible in the Tafel plot underneath. It is possible to create a Tafel plot by reading the current always at the same time after the anodic pulse is applied. These lines are shown for each point in time from Fig. 33a) and are colored from black to blue in Fig. 33b). This gives a good estimate of how much the final Tafel plot depends on the chosen readout time. As this is an intrinsic feature of the data is is not able to completely circumvent making a choice here.

Remembering the aim to compare several different samples, the most important advantage is the consistency of the polynomial behavior after an initial period. A readout time of 1 s (red) is chosen for all investigated samples, which is analogous to setting $t_0 = 1$ in Eq. 63. The resulting Tafel plot arising from this choice is compared to another arbitrary choice of 45 s (green) in Fig. 33b). The lower value is preferred as is closer to the (anticipated) original, non-deactivated, case excluding all unpredictable effects happen in the first 10 s. Although a completely unbiased choice is not possible, it is a pragmatic choice in the given situation and certainly more reliable than the actual data points before the linear region.

5.2 Development of a standard characterization protocol

We will now describe the standard protocol developed for systematic electrochemical studies – this protocol enabled a comparative study among all available RuO_2(110) thin films. The protocol was optimized at a few test samples of different growth qualities beforehand. By the time the presented version of the protocol was designed, the decaying current behavior had already been identified as the main bottleneck of a reproducible, as well as reliable Tafel analysis. The possible improvements to the current protocol, which will be outlined at the end of this section, are mainly determined by the knowledge gained in the preceding section.

The most important parameters and techniques of the protocol are summarized in the top half of Fig. 34. The lower half shows (a selection of) the most important plots that were generated for every sample by means of an automatized and optimized data evaluation script. The typical work flow during the batch characterization included a preparation phase, the actual experiment and a cleaning procedure before the next run. At the beginning, the sulphuric acid electrolyte was pre-bubbled in a clean beaker by nitrogen gas supplied by a corrosion resistant poly(ethene-co-tetrafluoroethene) (ETFE) tube. This was usually done during the sample mounting process. Sometimes air bubbles got trapped on top of the sample when filling the electrolyte into the cell. If this was the case, they were removed with a pipette. During the experiment, the electrolyte that was already pre-conditioned with inert gas was continuously blanketed with N_2. Actually bubbling gas results in increased noise in the current response; thus, we used laminar flow over the surface. Then, the measurement protocol can be started and a whole run takes about 9 h. After the protocol finished, the cell is opened and usually some oxygen bubbles adsorbed to the sample were created. A photograph is taken each time. Clean experiments were possible by rinsing all cell parts thoroughly with deionized water. There were no hints that would indicate a need for more advanced cleaning procedures. Finally, all cell parts where blown dry by pressurized air and the cycle could start from the beginning.

The measurement protocol itself can be categorized into three blocks as shown in Fig. 34. The protocol starts and ends with a set of techniques that probe mainly the surface redox transitions. The center piece is the kinetic measurements in the OER regime, since the original main goal of this project was a characterization by means of the Tafel slope. Before and after the kinetic measurements the electrochemically active surface area (ECSA) is determined by CV and EIS as described in section 4.3 and section 4.2.

The live ohmic drop compensation, which was described in , was always active at 85 % and the series resistance was remeasured at the beginning of each block, by means of a four consecutive averaged high frequency EIS measurements at $f = 100\,\mathrm{kHz}$, to account for changes during the characterization. The OCV is checked in between most of the techniques while there is also a longer 5 min period at the beginning of each green initial and final state block. Next, six sets of CV experiments are conducted – each three at $200\,\mathrm{mV\,s^{-1}}$ and at $3000\,\mathrm{mV\,s^{-1}}$. For each scan rate three different upper limits are chosen: $1.4, 1.5, 1.6\,V_{RHE}$. The symmetrized spectra taken in an intermediate range ($1.5\,V_{RHE}$) are shown in Fig. 34a1) and a2) (subsection 4.5.4). Fig. 34b1) shows one set of three voltammograms taken at stepwise increasing range (as utilized to discuss the chloride-induced CER). In this case, the largest range nearly overlaps with the smallest at the end of the protocol. In the magnified view (b1)), the difference between smaller

(blue, orange) and largest (green) range becomes visible and indicates a tiny chloride leakage after the 9 h protocol, which was still left after counteracting this problem (subsection 3.5.2). When the $HgSO_4$ RE eventually arrived, this problem could be eliminated completely, resulting in CV data which perfectly overlapped. Each set of voltammograms consists of up to 15 consecutive cycles, which usually approach a steady-state (overlapping consecutive scans) response. Always the stable last cycle is presented.

The remaining two techniques performed within the protocol are shown in Fig. 34a3) and Fig. 34a4). The fast square-wave voltammetry (SWV) in a4) serves as backup to double check trends observed in the SPEIS and CV measurements. Short 10 ms voltage pulses of 50 mV step height are applied alternately in positive and negative direction. To each step, a small offset of 0.5 mV is added each period like a staircase. This is done across the whole scanned potential range and the current measured during the negative pulse is subtracted from the positive one, therefore, enhancing the signal of the redox features. This relies on the same principle as for the fitting procedure, which also subtracts the cathodic from the anodic sweep beforehand. As this is a reasonably fast method there is no real time benefit from omitting it. However, it lacks of qualitative interpretability due to the highly dynamic conditions. Consequently, this method turned out to yield no additional insights. The last technique of the green block is staircase potentiostatic EIS or SPEIS, which was described in section 4.2. Here, an EIS spectrum is taken each 50 mV over the whole relevant potential range. Each point is pre-polarized for 10 s. By fitting an equivalent circuit model, as previously described (section 4.2), to each spectrum the potential dependent cell series resistance, charge-transfer resistance and cell capacitance can be extracted. In this case, the potential dependent capacitance, which is depicted in Fig. 34a3), is of interest as it clearly shows the capacitance caused by the surface redox features. While the other techniques are cut before the underlying OER disturbs the CV too much, the DLC can also be probed deeply into the OER region without (at least visual) obstruction.

The ECSA determination by means of increasing scan rate voltammograms in the double-layer region of the blue part was described is section 4.3 and is depicted in Fig. 34b3). Before the measurement is performed, the sample is pre-polarized for 10 min at the center potential to allow occurring background currents to the decay. The obtained capacitance value is backed up by two EIS measurements at the center potential both before and after the CV.

The Tafel measurements are performed by three different techniques. Since a Tafel plot is expected to include generally no historical responses, all techniques should yield similar results under steady state conditions. The preceding chapter and the sections within the present chapter clearly proved that this is not true, therefore, these different techniques mainly aided in building an intuition about the current decay and enables us to review different trends in the Tafel plot from different perspectives. The current responses to the slow SWV, NPV and SV scans are plotted over the time of the current orange characterization block in Fig. 34c) respectively. The magnified view shows a typical part of the current response to the applied voltage signals underneath. In this case, the SWV is intended to trigger an accelerated decay in the first larger upwards voltage step (20 mV) to possibly reach a more steady state when stepping back down 10 mV. This partly works out, but still the current decays a bit faster at elevated potentials in the backwards step than in the lower potential region. The NPV experiment is the most promising technique, as outlined earlier. SV resembles a slow CV experiment

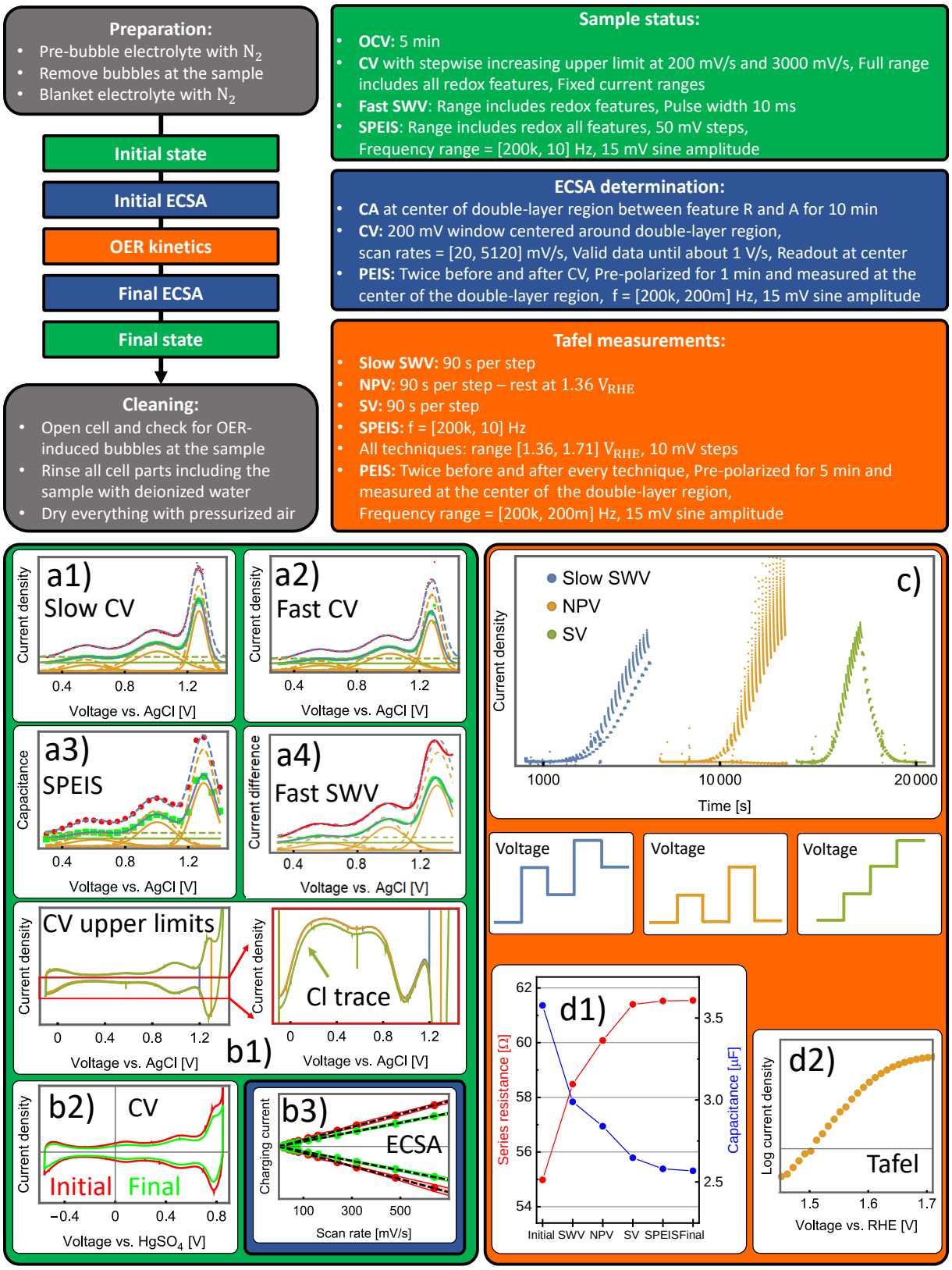

Fig. 34: The standard measurement protocol divided into three subgroups: The sample status judged by the surface redox transitions, determination of the electrochemically active surface area (ECSA) and Tafel measurements of the OER kinetics. a) The main redox features are probed by cyclic voltammetry (CV) at 200 mV s^{-1} (a1)) and 3 V s^{-1} (a2)), staircase potentiostatic electrochemical impedance spectroscopy (SPEIS, a3)) and square-wave voltammetry (SWV, a4)) The initial (red) and final (green) state is shown including the respective Gaussian fits (dashed and solid). b1) Increasing the upper limit of the cyclic voltammogram stepwise reveals a chloride trace contamination through the chlorine reduction (CRR) current, which establishes after surpassing the kinetic barrier for chlorine evolution (CER). b2) Comparing the initial and final state voltammogram shows a proportional decrease of the current that can be attributed to adsorbed bubbles. This is confirmed by the decrease of the double-layer capacitance (DLC) determined by scan rate-dependent CV in the double layer region in b3). c) Measurements of the OER current by three different techniques (voltage profile sketched underneath): Each potential step of 10 mV is held for 90 s. d1) Evolution of the series resistance and capacitance during the protocol measured by EIS. The trend is caused by evolving oxygen bubbles, which block parts of the surface, d2) Tafel plot extracted from the NPV experiment as described in subsection 5.1.3.

with larger voltage steps. As 10 mV are scanned every 90 s, this scan is performed at about $\nu = 0.11\,\mathrm{mV\,s^{-1}}$. Fig. 34d2) shows the final Tafel plot, which is extracted from the NPV experiment as described.

The original aim of the blue surface area characterization blocks was to observe possible sample corrosion by surface roughening, and, therefore increased DLC. It turned out that the main effect that determines the DLC is the adsorption of larger bubbles, which develop slowly during the protocol and decrease the DLC. This explains the difference usually observed in the initial and final ECSA measurement (Fig. 34b3)). This is also in line with the decreased (non-normalized) current after the protocol observable in Fig. 34a) and b2). Normalizing the current by the measured DLC allows us to correct for all bubble-induced surface shadowing effects. Measurements of the series resistance and the DLC determined by EIS before, after and in between the kinetic measurements are shown in Fig. 34d1). As just stated, the DLC decreases in a stepwise manner. These DLCs are used to normalize the kinetic currents measured in the subsequent experiments to correct for adsorbed bubbles. Again, as outlined before, the formation of bubbles is not able to explain the decaying OER current as it happens on a totally different time scale (about 2 h per OER technique). The series resistance increases, which makes sense as the volume of electrolyte above the sample decreases – therefore, less conductor (electrolyte) per area remains available to carry the current. Within a future setup, bubbles could be counteracted by impinging a jet of electrolyte onto the surface, which is pressurized by a peristaltic pump.

To conclude, the general structure of the protocol worked out very well up to now. In an optimized protocol, the fast SWV can be omitted as it lacks quantitative use. The SPEIS, which was actually intended as a fourth kinetic experiment, turned out to have too much cross-talk between the charge-transfer resistance (which should contain the information about the kinetic current) and the capacitance of the redox feature – this disqualifies it for a Tafel analysis.

The main focus of a further optimized future protocol should be directed at the NPV technique. The protocol yielded evidence that the current decay can be consistently fitted from about 10 s onward in an NPV experiment. Going forward, this would reasonably allow us to shorten the pulse period from 90 s to about 20 s. If the linear region is expected to start after 10 s, measuring at least another 10 s of the valid data points could be a reasonable lower bound. This would in turn allow for several repetitions of the NPV experiment within the same amount of time. Repetitions lead to the next point: direct reproducibility. As some dependence on the sample history is observed between one and a following protocol run, there should be more focus on tracking these changes to get a better estimate of their nature and actual influence. Lastly, the observed dependence of the surface recovery on the restore potential opens up a whole new parameter space to optimize this experiment and thus to check how it influences the Tafel plot. Overall, it turned out that there is no standard procedure to perform Tafel analysis at RuO_2(110) thin films, however, it seem that this is possible through further optimization of the experiment.

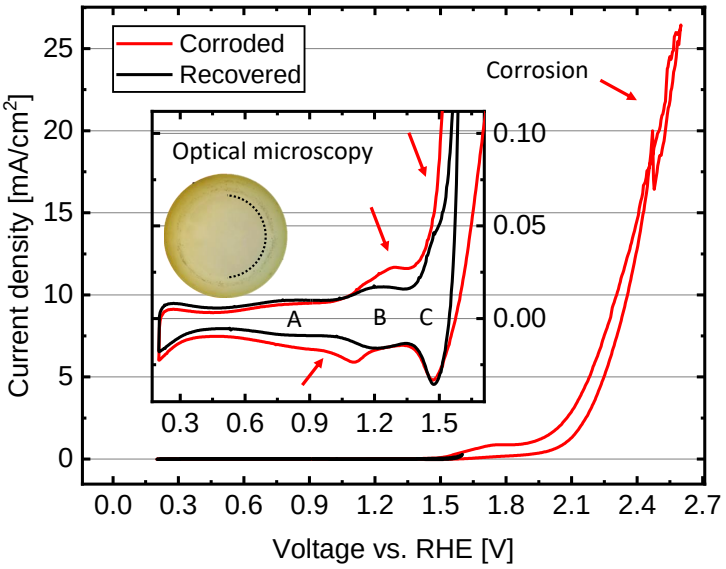

Fig. 35: Cyclic voltammetry (CV) at 100 mV s^{-1} up to high anodic potentials of 2.6 V_{RHE} where the sample corrodes. The inset shows the typical surface redox features in the recovered state; additional features develop during the high anodic potentials. The recovered state is reached by decreasing the upper potential limit. After prolonged high potentials the film dissolved into the electrolyte. The transparent substrate becomes visible with the optical microscope.

5.3 Sample changes induced by the electrocatalytical characterization

During electrochemical characterization, the samples are exposed to a harsh low pH environment. Especially during the OER studies at elevated anodic potentials the single crystal samples are expected to suffer corrosion.[20,128,129,101] From the Pourbaix diagram of RuO_2, a transition to RuO_4 can be identified as possible corrosion mechanism:

$$RuO_{4(aq)} + 4\,H^+_{(aq)} + 4\,e^- \longrightarrow RuO_{2(s)} + 2\,H_2O_{(l)}, \qquad E^\circ_{RuO_4} = 1.39\,V_{SHE}.^{8} \tag{64}$$

This is a claim usually found in the literature[20,101], where it is commonly supported by studies that identified RuO_4(aq) as the corrosion product of Ru metal under OER conditions in acidic electrolyte[130,131]. Although Ru electrodes are oxidized prior to corrosion, these oxides consist of hydrous ruthenium oxides (RuO_xH_y) and are therefore barely comparable to RuO_2 crystals.[132] A more recent study calculated a Pourbaix diagram that suggests a transition from RuO_2(s) to H_2RuO_5(aq) at the relevant potentials during OER. Furthermore, just below the experimental pH 0.1 conditions, a $H_2RuO_2^{2+}$(aq) species is predicted to be stable at potentials below the transition potential to H_2RuO_5(aq).[133] This illustrates that the actual corrosion mechanism of crystalline RuO_2 is still unknown and demands for further experimental studies.

The following discussion will focus on the extent of corrosion rather than the actual mechanism. It is stressed here that the findings regarding the surface deactivation (subsection 5.1.2) were also ascribed to a corrosion intermediate, which could be a hint toward a related mechanism. Further experiments are needed to confirm the supposed correlation of OER current decay and surface corrosion.

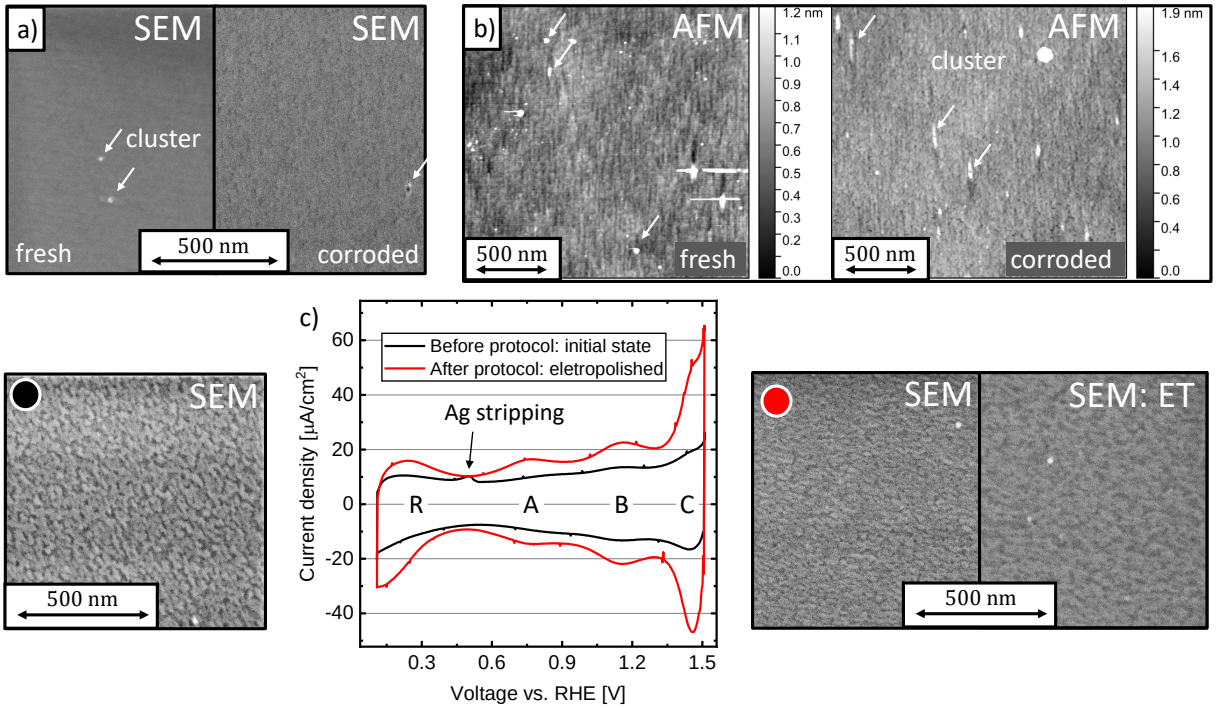

Fig. 36: a) In-lens scanning electron microscopy (SEM) image before and after prolonged oxygen evolution: Increased surface roughness is observed afterward. b) Atomic force microscopy (AFM) at the sample in the corroded state: A measurement outside of the catalytic area represents the fresh state. The measurement within the catalytic area (corroded) shows similar increased roughness as hinted by SEM in a) on the right. c) CV at a blue category (Fig. 20), less quality film before and after running the characterization protocol (Fig. 34. The behavior is identified as removal of contaminations by electropolishing. The SEM images are taken before and after the CV experiments and show no major structural mutation.

One flat, good quality sample was subjected to several hours of high anodic potentials during NPV, SWV and SV experiments with extreme periods of 1 h per step. To give an estimation of the severeness of these studies: From an overall experiment duration of 171 h, the time spent between 1.50 V_{RHE} and 1.64 V_{RHE} (OER occurs) amounted about 57 h. The time spent at elevated potentials was roughly equally distributed among the potentials in the given range. The resulting corrosion can be identified by SEM and AFM in Fig. 36a,b). Fig. 36a) shows in-lens (IL) SEM micrographs of the same magnification before the first electrochemical experiment (*left*) and after the described prolonged oxygen evolution (*right*). A transition from a slightly (horizontally) striped to a rough surface is observable. This was observed at several spots in both cases. Most likely the contrast of the SEM image on the right is caused by the edge effect around protruding features. The corrosion looks homogeneous, and is in contrast to pitting corrosion which produces distinct holes. Pitting corrosion occurs when the corroded parts of a surface are less stable than the unaffected parts of the surface.

Since SEM images offer no real height contrast, the findings are backed up by AFM in Fig. 36b). The AFM image taken at the sample's corner (Fig. 36b), left) is assumed to represent the initial state and is compared to the corroded state on the right. Some of the already known Ru clusters, which are surrounded by rectangular plateaus, can be identified in both images. Since a roughening of the predominant flat part is of interest, these are excluded from the following average surface roughness estimation. The flat parts are of interest as SEM suggests a homogeneous corrosion (Fig. 36a), after) rather

than larger pits. All excluded areas above a certain height threshold are colored white. Besides, the images are corrected for scars and the horizontal rows are vertically aligned by a median subtraction of each row. The RMS roughness of the presented AFM measurements (excluding clusters) is (130 ± 20) pm initially and increases to (160 ± 10) pm after the corrosion study within the catalytic area. As the definition of where the bulk film ends and where a cluster always comes with a subjective choice, the error of the surface roughness is estimated as follows: A patch of (already filtered) data mostly including grains is utilized to estimate the upper error margin and an area with no clusters (and of similar size) determines the lower bound of the RMS surface roughness. This study proves that the investigated samples are reasonably stable under the measurement conditions and far from being dissolved. Goryachev *et al.* reported SEM pictures that show signs of corrosion at RuO_2(110) thin film electrodes. Distinct holes on the length scale of about 0.5 µm show up after just one hour of anodic polarization at 1.50 V_{RHE}. This indicates a drastic stability difference, which can be ascribed to the different growth method. The thin films of Goryachev *et al.* originate from oxidized Ru(0001) single crystals, which seem to be less stable than the PLD-grown samples of the present work.

To test the stability limit of the thin films another sample has been subjected to a stress test, which was able to eventually dissolve the oxide layer. This became visible by eye as the reflectivity clearly decreased and the transparent TiO_2 substrate became visible underneath. An optical microscopy image is shown in Fig. 35, which exhibits a (circular) bright area where the sample suffered corrosion. This could only be achieved through prolonged polarization up to a maximum tested potential of 2.7 V_{RHE}. Before the sample was dissolved, the surface redox region had been observed by cyclic voltammetry through scanning over a large potential range, which includes the high anodic potentials as well as the lower potential region as shown in Fig. 35. Additional features near peak B and above C appeared (Fig. 35, red arrows) during the large range cycles, starting from an upper limit of 1.8 V_{RHE} and getting more prominent the higher the scan is extended. These features disappeared again, when the upper potential limit was decreased back to 1.6 V_{RHE}. A voltammogram recorded at 100 mV s^{-1} exhibiting the features (red) and one in the recovered state (black) is shown in Fig. 35. The strong current rise above 1.8 V_{RHE} is likely caused by the actual corrosion of the sample and accompanied with visible bubble evolution – the current gets instable at its peak. The simultaneously observed features in the surface redox region could be a possible route toward the identification of corrosion products or byproducts.

Besides corrosion there is a process called electropolishing. This can, e.g., be utilized to clean a contaminated Pt CE before an experiment. It relies on the anodic dissolution of contaminations and the upper layers of the platinum surface, which in turn leaves behind a clean, yet rough, surface. In this regard, this type of electropolishing is identified in Fig. 36c). It shows CV at a bad quality sample (light blue SEM category, subsection 4.1.1) at the beginning and at the end of the first run of the characterization protocol (section 5.2). All surface redox features appear much sharper after the sample was exposed to OER potentials. One could suppose that the observed transition within the cyclic voltammograms is accompanied with an observable structural transition. SEM images taken directly before and after the presented voltammograms show that the same rough structure is still present. (left and right to Fig. 36c)) The IL image of

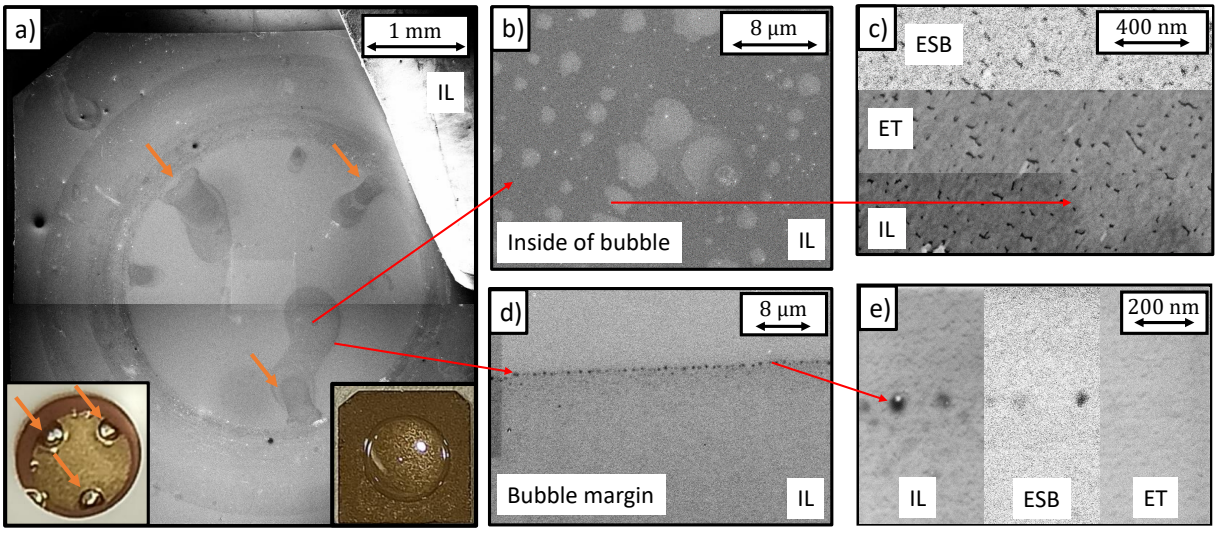

Fig. 37: a) Identification of features related to adsorbed oxygen bubbles at the surface by SEM (in-lens). The insets show the bubbles as well as the adsorption behavior of water after experiment. Magnified view of the margin of bubble, d), and within the bubble b). c,e) Features from b) and d) magnified and recorded with three different detectors. Feature b) solely shows contrast in the in-lens (IL) image, while e) is also visible with compositional contrast (ESB).

the final state on the right of Fig. 36c) is backed up by the ET secondary electron detector. The structures appear a bit wider as it offers less lateral resolution. The difference in the contrast before and after electropolishing could indicate slight corrosion induced surface smoothing or could just be related to the slightly different measurement parameters (electron beam acceleration voltage of 3 kV instead of 2 kV). Similar experiments at flat samples (green SEM category, subsection 4.1.1) showed no visible sign of corrosion after a single run of the protocol, yet they exhibited an analogous behavior in the initial and final CV scans. This leads to the conclusion that actual surface contaminations are cleaned off by this process, rather than severe structural mutations like during a corrosion process.

The last interesting feature that is induced by the electrochemical measurements is IL SEM contrast on the exposed surface, which can be attributed to adsorbed oxygen bubbles. All of the following observations were confirmed at several samples from all different categories. Fig. 37a) shows a low magnification IL image of the whole sample and a photo of the sample taken just before within the electrochemical cell in the bottom left inset. The cell is already filled up with electrolyte and three large and some smaller oxygen bubbles, which were produced during the characterization are visible. Since the photo is taken in the same orientation as the SEM image the features can be directly correlated to each other. The inset on the right shows another frequent observation: After taking the sample out of deionized water (cleaning step) after the measurement, a water droplet got trapped in the exact center of the surface. This water droplet had to be cleaned of with pressurized air as it would not just fall off by shaking. Two conclusions are possible: Either parts of the sealing FPM o-ring stick to the sample and create a hydrophobic ring around the catalytic area, or a surface termination with increased hydrophilicity, originating from the electrochemical tests, is still present after rinsing the sample.

The large areas of darker contrast, which were attributed to oxygen bubbles, consist

of several smaller bright circular spots on top of a dark background. These are illustrated in a magnified view in Fig. 37b), which also shows IL contrast. Further magnifying a boundary of one of the smaller circles reveals an interesting property. The whole area shown in Fig. 37c) is taken at the same spot, where the boundary is observable. Comparing the IL image to the ET and material contrast ESB detector signal shows that the contrast vanishes. This leads to the conclusion that the observed features are neither related to a different material nor they are connected to morphological effects, which the ET detector should also be able to detect. As the IL detector is in principle also sensitive to slight variations of the sample work function, it maybe indicates a different oxidation state at the termination of the surface. At the boundaries of the large bubble-induced features observed in Fig. 37a), chains of dark points can be observed with the IL detector as shown magnified in Fig. 37d). Like before, a magnified view showing three detection modes is presented in Fig. 37e). In this case, only the ET detector shows no contrast. The ESB detector reveals also a dark contrast at the position of the dots. This indicates that there is actually some material of lower atomic number than the surrounding deposited material. The IL image on the left also shows a bright spot within a dark point which could indicate a larger conglomerate (this is the only spot, which also shows ET contrast).

All of these observations have to be taken into account when trying to interpret the CV and kinetic data, as it is not obvious why these features appear that locally. If this indicates an unequal current distribution during the kinetic measurements it would have severe implications for normalizing the current. Nevertheless, the working hypothesis is that the whole area is utilized and only regions where bubbles actually stay adsorbed exhibit the presented features.

5.4 Results of the protocol

5.4.1 Sample categorization by cyclic voltammetry and Tafel plot

All samples can be divided into three subgroups depending on their response to the standard protocol. These groups can be further correlated to the prior SEM characterization (subsection 4.1.1). Distinct behavior is observed for fresh flat good quality films (green category), aged, and therefore likely corroded good quality films and intrinsically rougher films from the light blue and yellow category (subsection 4.1.1). The two key figures of merit are presented in Fig. 38, namely CV and the Tafel plot.

For each of the three mentioned groups of samples, Fig. 38a) shows two representative voltammograms recorded at a scan rate of $200\,\mathrm{mV\,s^{-1}}$ in $1\,\mathrm{M}$ H_2SO_4. All voltammograms are taken after the first run of the protocol, and therefore show the electropolished state. Furthermore, the voltammograms are normalized to the ECSA as described in section 4.3. This comparison provides further evidence for the interpretation of A as a feature originating from surface defects. Interestingly, former good quality samples, which suffered corrosion after prolonged OER potentials, seem to approach the state of the intrinsically rough and defect rich surfaces. Nevertheless, feature B and C still show different amplitudes. Further studies, which focus on the CV responses during a more controlled sample aging could shed some more light on the electrochemically induced structural transitions.

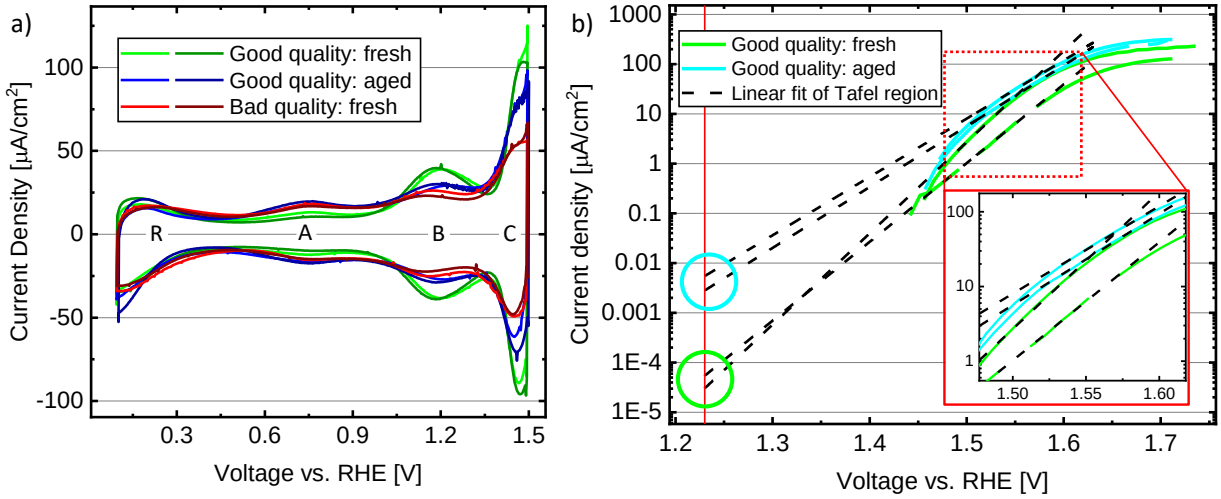

Fig. 38: The groups identified by the surface redox features, a), and Tafel analysis, b), match the SEM categorization (Fig. 20). a) Cyclic voltammetry (CV) is performed at 200 mV s^{-1}. The green flat samples show the smallest current at feature A and the most pronounced features B and C. b) In the Tafel plot, aged and fresh good quality separate into two subgroups by their slope and intersect with the water-splitting standard potential.

For the actual Tafel analysis, the method described in subsection 5.1.3 is applied. Only the flat good quality samples showed a reasonably linear region in the Tafel plot. All of the other growth modes showed an initial plateau (or peak) in the first kinetic SWV experiment (Fig. 39a,b), blue). Moreover, this trend continues to various extents during the following NPV (orange) and SV (green) experiments. It can likely be attributed to an electrochemical side reaction, which is connected to the identified electropolishing behavior. The resulting Tafel plots exhibited a round non-linear behavior, which sometimes included plateaus. The difference to real electropolishing at flat samples (stripping mainly surface contaminations) is ascribed to less sample stability in the rough case, which would result in actual structural (corrosion-like) changes. As shown in Fig. 36c), at least with the lateral resolution of the SEM, no significant morphological differences were observed before and after running the characterization protocol. In general, the non-simple Tafel plots and observed plateaus indicate that the OER is probably not the only occurring process during the first protocol run at the less quality samples. Consequently, only samples that exhibit a clear Tafel region will be discussed by means of a Tafel analysis.

Fig. 38b) shows two representative Tafel lines (fresh and aged) for the two remaining subgroups of flat samples. These exhibit a different Tafel slope depending on their corrosion history. Also, the extrapolated intercepts with the water splitting standard potential separate into two subgroups. The regions exhibiting approximate linear behavior are not located within the same potential windows and were identified manually. It was tried to automatize the identification of the linear potential window to make it more objective, but the Tafel lines (of all tested samples) appeared to be too variable to yield consistent results without introducing too much constraints. This is a clear weak point, which needs further attention in future efforts.

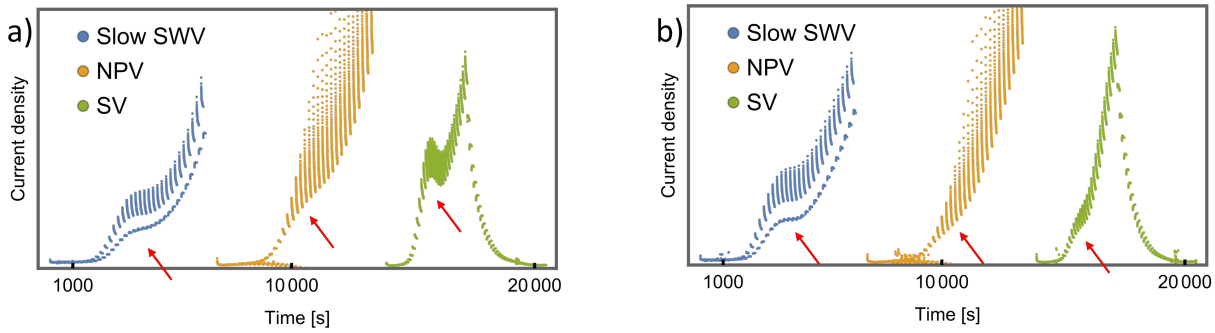

Fig. 39: a,b) Qualitative comparison of two bad quality (Fig. 20) samples by all three techniques applied for the determination of the Tafel plot. A peak or plateau shows up in different extends in all three techniques. This points towards an electrochemical process occurring besides the OER making – this prevents a reliable determination of the Tafel slopes.

5.4.2 Tafel analysis

The average Tafel slope of the fresh good quality samples yields $b = (59 \pm 4)\ \frac{\mathrm{mV}}{\mathrm{dec}}$. Extrapolating the Tafel lines to the water splitting standard potential ($E^\circ = 1.23\,\mathrm{V_{RHE}}$[8]) yields the exchange current density j_0 according to TST as motivated in section 1.2. The average exchange current densities are directly converted to transition state free energies $G^\#$, according to Eq. 7, assuming a density of active sites of $\Gamma = 5\,\mathrm{nm}^{-2}$ (ideal (110) surface unit cell) and a total number of $z = 4$ electrons for the OER. This yields $G^\# = (0.97 \pm 0.02)\,\mathrm{eV}$ The uncertainties are roughly approximated by the maximum spread of the small sample of data, where no statistical methods are applicable. The samples, which already suffered corrosion exhibit a slope of $b = (83 \pm 4)\ \frac{\mathrm{mV}}{\mathrm{dec}}$ and transition state free energy of $G^\# = (0.86 \pm 0.02)\,\mathrm{eV}$. This stresses the dependence of the Tafel plot on the sample history as significant differences are observed. Assuming actual Tafelian behavior would lead to the interpretation that corrosion causes a lowered transition free state energy, which in turn would explain the overall higher activity among this group. Effects of increased surface area by corrosion-induced roughening are already corrected via normalization to the ECSA (determined by the DLC). If this correction, contrarily to the common assumption, does not account sufficiently for all increased area effects, this could also increase the apparent activity. The corrosion induced increase of surface roughness determined by AFM (section 5.3) also can not justify the trend.

The transition state free energy does not match the reported value of $G^\# = 1.06\,\mathrm{eV}$ (in the lower Tafel region) from Exner *et al.*[34]. The literature about OER Tafel slopes of RuO_2(110) single crystals or thin films in acidic electrolyte is scarce. Rao *et al.*[23] report a value 'around 60 $\frac{\mathrm{mV}}{\mathrm{dec}}$' for (110), (100) as well as (101) oriented films between $1.5\,\mathrm{V_{RHE}}$ and $1.6\,\mathrm{V_{RHE}}$. They used averaged CV experiments at $10\,\mathrm{mV\,s^{-1}}$ and took a few potentiostatic CA measurements. A supplementary figure[23] shows the discussed current decay, which they interpret as a stabilization toward a stable value. It is stressed that their current also seems to never actually stabilize. Apart from that, their (only approximately reported) Tafel slope is confirmed. Kuo *et al.*[49] report around 80 $\frac{\mathrm{mV}}{\mathrm{dec}}$ at pH 1.0 for their MBE-grown thin films on TiO_2 substrate. Even though, this value matches the corroded group of samples it is unlikely that this is the reason in their case as none of their published voltammograms exhibits a redox feature A (Fig. 24b)), which is attributed to

corrosion (subsection 4.5.9).

The theoretical work of Exner *et al.*[34], which motivated the Tafel analysis, relies on a publication from 1986 of Castelli *et al.*[134]. They report 59 $\frac{\mathrm{mV}}{\mathrm{dec}}$ in the lower and 118 $\frac{\mathrm{mV}}{\mathrm{dec}}$ in the higher Tafel region. Their CV experiments show additional features, which are commonly not reported for RuO_2(110) in more recent literature. Furthermore, judging from the published voltammograms, their films suffered significant corrosion during the Tafel experiment. The reported higher potential Tafel region is a key element of Exner's[34] supposed OER mechanism, since he identifies it as transition to another stable starting surface of the OER cycle – which then proceeds over four consecutive PCETs. Castelli *et al.*[134] is the only group that has reported a higher Tafel region so far. The other mentioned studies[49,23] at most seem to observe a saturating behavior in the higher Tafel region, which would in turn indicate a higher Tafel slope than $\approx 60\ \frac{\mathrm{mV}}{\mathrm{dec}}$. None of the investigated samples of the present work exhibited a clear signature of a second Tafel region at higher potentials. In contrast a saturating (local slopes clearly $> 118\ \frac{\mathrm{mV}}{\mathrm{dec}}$) behavior is observed. In spite of the fact that the logarithmic current increases 'only' with $> 118\ \frac{\mathrm{mV}}{\mathrm{dec}}$, which appears relatively flat in a logarithmic plot, the current still rises with increasing potential and does not approach a fixed saturated value.

The confirmation of the $\approx 60\ \frac{\mathrm{mV}}{\mathrm{dec}}$ slope alone does not allow for a definite conclusion, which would add to the current literature. The observed hints that there may be no higher Tafel region again stresses that further efforts are needed to elucidate the reaction mechanism based on the Tafel analysis. Current trends toward in situ-electrochemical experiments seem to be a promising method. Still, the original hope of this project to compare various samples by means of their Tafel slopes is still up to date. After modeling the deactivation of active sites and developing a procedure (subsection 5.1.3) to consistently perform the Tafel analysis, the focus of future experiments should shift toward optimizing the measurement parameters of the NPV experiment especially for the described procedure. Furthermore, decreasing the overall experiment time would allow for numerous iterations at the same sample to confirm the reproducibility of the experiment and track the sample history induced variations.

5.4.3 Analysis of peak width and charge

It has already been shown in Fig. 38a) that the prior SEM categorization by the sample morphology reflects in the cyclic voltammogram. By means of the described fitting procedure (subsection 4.5.4) the observed qualitative trends in CV can also be quantified. Next to the general difference between flat and rough samples shown in Fig. 40b), the previously described electropolishing behavior exhibits a clear trend as illustrated in Fig. 40a). Fig. 40a) correlates the charges attributed to a surface redox transition (determined by the CV peak area and normalized to ECSA) to the FWHM of the three main redox features A, B and C, which can be interpreted as a figure of merit of adsorbate interactions. The green, red, and black points represent feature A, B and C respectively. Electropolishing, as already shown for a rough sample in Fig. 36c), results in clearly increased charge, i.e. peak area, participating in the surface reactions while at the same time the FWHM stays comparably stable. In Fig. 40a) the initial state of the rough samples is depicted in light colors, while the points originating from the end of the protocol are plotted in darker colors. A clear overall shift toward higher peak charges per area is visible between the light and dark points. The black points also hint at a decrease

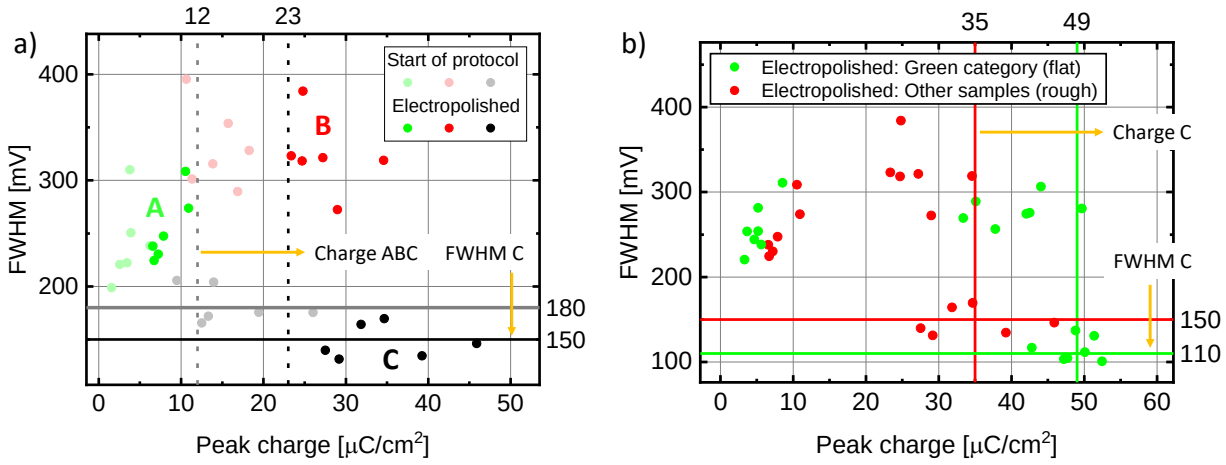

Fig. 40: Trends observed by fitting cyclic voltammograms of various samples as described in subsection 4.5.4. The FWHM and peak charge accompanied with the surface redox transitions A, B and C serve as a figure of merit. Average values of subgroups of samples are depicted by lines and highlight the trends. a) Comparison of the initial state (light colors) at the beginning of the characterization protocol (Fig. 34) to the electropolished state (normal colors) after the protocol. The data points separate into three clusters which represent the values of a certain transition. The main difference is that the average charge of all peaks increases after electropolishing. Furthermore, the FWHM of feature C sharpens. b) Comparison of the electropolished states of good quality to worse quality samples. The good quality samples show a general trend toward less charge of feature A and more charge attributed to B and C.

of the FWHM, which results in a downward shift. It appears that all features can be distinguished by their FWHM as well as their charge.

Average values of peak charge and FWHM among certain groups are presented in Tab. 1, which quantifies all trends observable in Fig. 40. The uncertainties are estimated by the sample standard deviation. Fig. 40b) only shows the electropolished state of the rough as well as the flat samples. The flat sample exhibit a sharper peak width, more charge attributed to B and C and less charge attributed to A. Peak A also behaves distinctly with regard to the FWHM of feature A as it is similar for both sample qualities. Both trends are in line with the interpretation of a defect related feature, which could reasonably behave the same way on different samples.

Tab. 1: Normalized charge and FWHM of the surface redox transitions A, B and C averaged among samples of a similar group, determined by the fitting of cyclic voltammograms at 200 mV s^{-1} as described in subsection 4.5.4.

Charge [$\frac{\mu C}{cm^2}$]	A	B	C
Rough: initial state	(4 ± 2)	(14 ± 3)	(16 ± 6)
Rough: electropolished	(8 ± 2)	(27 ± 4)	(35 ± 7)
Flat: electropolished	(5 ± 2)	(41 ± 6)	(49 ± 3)
FWHM [mV]	A	B	C
Rough: initial state	(240 ± 40)	(330 ± 40)	(180 ± 20)
Rough: electropolished	(250 ± 30)	(320 ± 40)	(150 ± 20)
Flat: electropolished	(260 ± 30)	(280 ± 20)	(110 ± 10)

The transferred charges per area of the good quality samples can be utilized to estimate a the number of sites participating in these transitions. An active site density of $5\,\mathrm{nm}^{-2}$ can be assumed for an ideal surface as it can be readily determined from the (110) surface unit cell (subsection 4.5.5). It is further assumed that $4/3$ electron are transferred per $\mathrm{Ru_{cus}}$ during transition C. This was proposed in subsection 4.5.9 and implies one of three $\mathrm{Ru_{br}}$ sites additionally participating in the transition. This yields an average participation to peak C of $(46 \pm 3)\,\%$ of all expected sites. The relative participation of feature B assuming one electron transferred per $\mathrm{Ru_{cus}}$ yields $(51 \pm 7)\,\%$. The matching values of the participation already implicitly included the last consistency check. The relative fractions of electrons involved in the transitions B and C were estimated from the decay in subsection 4.5.7. This yielded that peak B is expected to exhibit about $3/4$ of the charge transferred in C. The experimental value can be determined from Tab. 1 to be $(80 \pm 10)\,\%$. This matches the expectation from subsection 4.5.7, even though the mentioned study was conducted at a single sample and is compared to an average of all other samples. This could imply that the determined peak ratio of B and C could be a general property of good quality samples.

5.5 Improvements for a future protocol

A simple exponential Tafel behavior was proposed and expected for $\mathrm{RuO_2}$(110) (section 1.2). The actual experiments at thin-film samples instead show a (reversible) deactivation process during the OER, which introduces a historic response to the Tafel plot. A region where the decaying current followed a polynomial law can be utilized to extract the Tafel plot more consistently for various samples and (partly) correct for the decaying nature of the process. At this point, presumably the most important improvements can be made regarding the NPV technique. The future strategy should be to investigate the dependence of the Tafel plot (obtained as proposed in subsection 5.1.3) of the following parameters: up- or downstairs potential steps, recovery potential, duty cycle and pulse period. The evaluation should be possible as soon as the linear region of the double logarithmic decay plot (Fig. 30c) at 10 s) is reasonably entered. One could further think of a quick EIS measurement in the double-layer region during the rest period (if the recovery potential is chosen at this point) to live-track the ECSA before each applied OER pulse. This would allow to track the surface shadowing by adsorbed bubbles and normalize each single decay curve to its respective ECSA. By now, the ECSA is only checked before and after the experiment. One has to assure that the overlaid 15 mV amplitude sine wave during parts of the rest period does not significantly interfere with the experiment. After optimizing the technique, more good quality samples are needed to check the reproducibility in consecutive runs and among samples of known same surface structure. In contrast, in the present study even samples of the same group were originated from different growth conditions, which always left some ambiguity about the origin of observed differences in the Tafel plots.

Such studies will be aided by further decreasing the overall experiment time of the protocol. This offers the advantage to decrease corrosion induced changes. Measuring a sample after an electrochemical structural mutation does not yield information of the initial state anymore. This is still the main goal – to correlate knowledge about the microscopic sample structure (and electronic structure) to electrochemical activity. It is

important to sharpen the distinction between electropolishing (stripping of contaminations) and corrosion (significant structural mutations). Samples fresh from ultra-high vacuum (UHV) could shed some more light on this. Otherwise, pre-experiment cleaning steps, of chemical or electrochemical nature, have to be considered.

Besides the obligation to perform a more targeted study about corrosion induced changes, utilizing the knowledge gained so far, the protocol time can be reduced in the following ways: Dropping the fast and slow SWV, the SPEIS in the OER region, the SV and decreasing the NPV experiment time. Pre-conditioning Chronoamperometry (CA) techniques can also be shortened, as they have mainly been important to reduce background currents induced by trace chlorine gas (in some cases where the AgCl rather than the $HgSO_4$ RE was used).

Finally, the characterization by means of the surface redox transitions (A, B and C) offered a much more robust and feasible way to characterize the samples (subsection 5.4.3). The CV response is sufficiently consistent to allow for batch fitting and the experiment time (and modeling effort) is way the Tafel analysis, which makes it more reliable. Backing up the findings by SPEIS and CVs at different scan rate yields further confidence. As the fast SWV solely qualitatively confirms the trends, it yields no additional insights and can be omitted. Extracting the key parameters charge and width (no clear trends regarding the peak positions were identified within the experimental uncertainty yet), one could think of a fast batch screening of another set of samples grown at different conditions.

6 Conclusion and Outlook

The long-term vision of this project was to provide a causal link between the oxygen evolution reaction (OER) mechanism and the underlying physical phenomena rooted in the surface electronic structure of RuO_2(110) – a material which has historically, yet anomalously, shown some of the highest performance figures for this reaction. However, to probe such phenomena, one has to step back and firstly obtain an understanding of the OER from a strictly surface science perspective – this can be done by gaining control of the fundamental techniques (chapter 2) and understanding how they relate to a real experimental situation, as summarized below. In this thesis, we have demonstrated that it is possible to design a contamination-free (section 3.5) experimental setup (chapter 3), which enables for a comprehensive fundamental electrochemical characterization of atomically-ordered model samples: metallic RuO_2(110) thin films grown on top of insulating TiO_2(110) substrates. These films presented a near ideal platform for the electrochemical characterization of RuO_2(110) in this work, as they were of comparably high quality to films reported in literature to date (section 4.5). In particular, they exhibit superior stability with respect to corrosion, even under harsh OER conditions (section 5.3).

Utilizing the near atomically-flat nature of the samples, a reliable value for the specific capacitance of RuO_2(110) was determined by cyclic voltammetry (CV), electrochemical impedance spectroscopy (EIS) and scanning electron microscopy (SEM) (section 4.3). This is the key parameter that allows for a current normalization by means of the electrochemically active surface area (ECSA) and will be published in a short communication paper. The designed and optimized catlaytic cell, coupled with the electrochemical analysis techniques (chapter 2), could be applied to yield reliable, atomic-site specific insights about the potential-dependent surface terminations of RuO_2(110) in acidic electrolyte (section 4.5). Furthermore, it was possible to distinctly correlate the microscopic sample morphology (characterized by SEM in subsection 4.1.1) to properties of the surface redox transitions (section 5.4). Subsequently, a deactivation mechanism of the OER current was discovered, investigated and mathematically modeled to enable a reliable approach to Tafel analysis of the OER mechanism (section 5.1). The standard batch characterization protocol (section 5.2), which was developed throughout this project and used to obtain the above results, yielded satisfactory data relating to surface redox transitions. Finally, I propose a roadmap towards optimization of this protocol (section 5.5).

Overall, this thesis set up a solid foundation for future efforts. All common electrochemical techniques were applied to, and optimized for, RuO_2(110) thin films. As the experimental pitfalls and benefits are now elucidated, the focus can primarily shift toward further scientific questions. The exact mechanism behind the observed, and modeled, time- and potential- dependent loss of the OER activity is yet to be discovered. A novel method to investigate the surface redox transitions was derived from this effect, which is ready to be applied to a fresh set of samples to further confirm the reported

behavior. The first step towards the goal of establishing a robust link to surface science is therefore taken.

After corrosion of the samples has been investigated and the characterization protocol has been optimized, a variety of future pathways will open up. Firstly, a scanning flow cell setup (SFC) is already designed and ready to be set up. Briefly, such a setup would offer an electrochemical cell that introduces a constant electrolyte flow over the sample surface by means of a peristaltic pump, which aids the reactant and product mass transport; and, more importantly for the OER measurement, cleans off adsorbed bubbles from the sample's surface. Another main advantage is the sample stage, which is controlled by closed-loop linear actuators in x-, y-, and z-direction. This allows to investigate different spots of a sample; and furthermore, to mount several samples at once and automatically switch samples after the optimized characterization protocol ran once. Through thermostatting the sample stage and electrolyte reservoir, temperature-dependent measurements become possible. In addition, a flow cell type setup allows for the introduction of downstream analysis techniques to measure dissolved oxygen or corrosion products by, e.g., inductively coupled plasma optical emission spectrometry or mass spectrometry (ICP-OES or ICP-MS).

Besides the setup-related possibilities, our international collaboration with research and development scientists within the institute of Geological and Nuclear Science (Wellington, NZ) enables us to investigate how doping of the samples – by ion-beam implantation – affects the catalytic activity. Preliminary tests already hinted towards increased OER activity by implantation with (bulk) magnetic Co ions. Yet, up to now it has not been possible to rigorously show to what extend the increased activity is caused by surface roughening effects, which are induced by the implantation technique.

Doping with (bulk) magnetic ions could open a route toward the emerging field of spintro-catalysis[31], which tries to get to the bottom of the role of spin transfer during the OER. This is motivated by the intuition that magnetic triplet oxygen is produced from non-magnetic water molecules, thus, spin conservation has to be fulfilled by the catalytically active surface. As soon as the characterization by the Tafel analysis is proven to be reproducible, OER tests under an externally applied magnetic field could lead to further insights.

List of Acronyms

AC	**A**lternating **c**urrent
AFM	**A**tomic force **m**icroscopy
AIMD	**A**b **i**nitio **m**olecular **d**ynamics
ARPES	**A**ngle-**r**esolved **p**hoto**e**mission **s**pectroscopy
CA	**C**hrono**a**mperometry
CE	**C**ounter **e**lectrode
CER	**C**hlorine **e**volution **r**eaction
CNLS	**C**omplex **n**onlinear **l**east-**s**quares
CPE	**C**onstant **p**hase **e**lement
CRR	**C**hlorine **r**eduction **r**eaction
CSCA	**C**yclic **s**tep **c**hrono**a**mperometry
CV	**C**yclic **v**oltammetry
CVT	**C**hemical **v**apor **t**ransport
DC	**D**irect **c**urrent
DFT	**D**ensity **f**unctional **t**heory
DLC	**D**ouble-**l**ayer **c**apacitance
ECSA	**E**lectro**c**hemically active **s**urface **a**rea
EDX	**E**nergy-**d**ispersive **X**-ray spectroscopy
EIS	**E**lectrochemical **i**mpedance **s**pectroscopy
ESB	**E**nergy-**s**elective **b**ackscattered
ET	**E**verhart-**T**hornley
FWHM	**F**ull **w**idth at **h**alf **m**aximum
HER	**H**ydrogen **e**volution **r**eaction
IHP	**I**nner **H**elmholtz **p**lane
IL	**I**n-**l**ens
LEED	**L**ow-**e**nergy **e**lectron **d**iffraction
LJP	**L**iquid **j**unction **p**otential
MBE	**M**olecular **b**eam **e**pitaxy
NPV	**N**ormal **p**ulse **v**oltammetry
OCV	**O**pen-**c**ircuit **v**oltage
OER	**O**xygen **e**volution **r**eaction
OHP	**O**uter **H**elmholtz **p**lane
ORR	**O**xygen **r**eduction **r**eaction
PCET	**P**roton-**c**oupled **e**lectron **t**ransfer
PDS	**P**otential-**d**etermining **s**tep
PEM	**P**roton-**e**xchange **m**embrane
PLD	**P**ulsed **l**aser **d**eposition
PTFE	**P**oly(**t**etra**f**luoro**e**thylene)
RDE	**R**otating **d**isc **e**lectrode

RDS	**R**ate-**d**etermining **s**tep
RE	**R**eference **e**lectrode
RHE	**R**eversible **h**ydrogen **e**lectrode
RHEED	**R**eflection **h**igh-**e**nergy **e**lectron **d**iffraction
SE	**S**econdary **e**lectron
SEM	**S**canning **e**lectron **m**icroscopy
SHE	**S**tandard **h**ydrogen **e**lectrode
SPEIS	**S**taircase **p**otentiostatic **e**lectrochemical **i**mpedance **s**pectroscopy
STM	**S**canning **t**unneling **m**icroscopy
SV	**S**taircase **v**oltammetry
TEM	**T**ransmission **e**lectron **m**icroscopy
TST	**T**ransition **s**tate **t**heory
UHV	**U**ltra-**h**igh **v**acuum
UPD	**U**nder **p**otential **d**eposition
WE	**W**orking **e**lectrode
XPS	**X**-ray **p**hotoelectron **s**pectroscopy
XRR	**X**-**r**ay **r**eflectometry

Bibliography

(1) H. Over, "Surface chemistry of ruthenium dioxide in heterogeneous catalysis and electrocatalysis: from fundamental to applied research", *Chemical reviews* **112** no. 6, (2012) 3356–3426.

(2) H. Over, "Atomic scale insights into electrochemical versus gas phase oxidation of HCl over RuO2-based catalysts: A comparative review", *Electrochimica Acta* **93** (2013) 314–333.

(3) K. Seki, "Development of RuO2/Rutile-TiO2 Catalyst for Industrial HCl Oxidation Process", *Catalysis Surveys from Asia* **14** no. 3-4, (2010) 168–175.

(4) R. Chen, V. Trieu, B. Schley, H. Natter, J. Kintrup, A. Bulan, R. Weber, and R. Hempelmann, "Anodic Electrocatalytic Coatings for Electrolytic Chlorine Production: A Review", *Zeitschrift für Physikalische Chemie* **227** no. 5, (2013) 651–666.

(5) A. Cowley and M. Ryan, "Pgm Market Report", May 2021, retrieved: 01.03.2022. `http://www.platinum.matthey.com/documents/new-item/pgm-market-reports/pgm-market-report-may-21.pdf`.

(6) M. Carmo, D. L. Fritz, J. Mergel, and D. Stolten, "A comprehensive review on PEM water electrolysis", *International Journal of Hydrogen Energy* **38** no. 12, (2013) 4901–4934.

(7) B. Paul and J. Andrews, "PEM unitised reversible/regenerative hydrogen fuel cell systems: State of the art and technical challenges", *Renewable and Sustainable Energy Reviews* **79** (2017) 585–599.

(8) M. Pourbaix, *Atlas of electrochemical equilibria in aqueous solutions*. National Association of Corrosion Engineers, Houston, Tx., 2nd english ed. ed., 1974.

(9) H. Over, "Fundamental Studies of Planar Single-Crystalline Oxide Model Electrodes (RuO 2 , IrO 2) for Acidic Water Splitting", *ACS Catalysis* **11** no. 14, (2021) 8848–8871.

(10) S. Cherevko, S. Geiger, O. Kasian, N. Kulyk, J.-P. Grote, A. Savan, B. R. Shrestha, S. Merzlikin, B. Breitbach, A. Ludwig, and K. J. Mayrhofer, "Oxygen and hydrogen evolution reactions on Ru, RuO 2 , Ir, and IrO 2 thin film electrodes in acidic and alkaline electrolytes: A comparative study on activity and stability", *Catalysis Today* **262** (2016) 170–180.

(11) E. R. Kötz and S. Stucki, "Ruthenium dioxide as a hydrogen-evolving cathode", *Journal of Applied Electrochemistry* **17** no. 6, (1987) 1190–1197.

(12) C.-J. Chang, Y.-C. Chu, H.-Y. Yan, Y.-F. Liao, and H. M. Chen, "Revealing the structural transformation of rutile RuO2via in situ X-ray absorption spectroscopy during the oxygen evolution reaction", *Dalton transactions (Cambridge, England : 2003)* **48** no. 21, (2019) 7122–7129.

(13) Y. Yang, R. Zeng, H. Paik, D.-Y. Kuo, D. G. Schlom, F. J. DiSalvo, D. A. Muller, J. Suntivich, and H. D. Abruña, "Epitaxial Thin-Film Spinel Oxides as Oxygen Reduction Electrocatalysts in Alkaline Media", *Chemistry of Materials* **33** no. 11, (2021) 4006–4013.

(14) Y. Takasu, N. Yoshinaga, and W. Sugimoto, "Oxygen reduction behavior of RuO2/Ti, IrO2/Ti and IrM (M: Ru, Mo, W, V) Ox/Ti binary oxide electrodes in a sulfuric acid solution", *Electrochemistry Communications* **10** no. 4, (2008) 668–672.

(15) T. Hepel, F. H. Pollak, and W. E. O'Grady, "Chlorine Evolution and Reduction Processes at Oriented Single–Crystal RuO2 Electrodes", *Journal of The Electrochemical Society* **133** no. 1, (1986) 69–75.

(16) J. H. Jang, A. Kato, K. Machida, and K. Naoi, "Supercapacitor Performance of Hydrous Ruthenium Oxide Electrodes Prepared by Electrophoretic Deposition", *Journal of The Electrochemical Society* **153** no. 2, (2006) A321.

(17) Y. Liu, F. Zhou, and V. Ozolins, "Ab Initio Study of the Charge-Storage Mechanisms in RuO 2 -Based Electrochemical Ultracapacitors", *The Journal of Physical Chemistry C* **116** no. 1, (2012) 1450–1457.

(18) V. Jovic, R. J. Koch, S. K. Panda, H. Berger, P. Bugnon, A. Magrez, K. E. Smith, S. Biermann, C. Jozwiak, A. Bostwick, E. Rotenberg, and S. Moser, "Dirac nodal lines and flat-band surface state in the functional oxide RuO2", *Physical Review B* **98** no. 24, (2018) .

(19) V. Jovic, A. Consiglio, K. E. Smith, C. Jozwiak, A. Bostwick, E. Rotenberg, D. Di Sante, and S. Moser, "Momentum for Catalysis: How Surface Reactions Shape the RuO 2 Flat Surface State", *ACS Catalysis* **11** no. 3, (2021) 1749–1757.

(20) C. Roy, R. R. Rao, K. A. Stoerzinger, J. Hwang, J. Rossmeisl, I. Chorkendorff, Y. Shao-Horn, and I. E. L. Stephens, "Trends in Activity and Dissolution on RuO 2 under Oxygen Evolution Conditions: Particles versus Well-Defined Extended Surfaces", *ACS Energy Letters* **3** no. 9, (2018) 2045–2051.

(21) R. R. Rao, M. J. Kolb, N. B. Halck, A. F. Pedersen, A. Mehta, H. You, K. A. Stoerzinger, Z. Feng, H. A. Hansen, H. Zhou, L. Giordano, J. Rossmeisl, T. Vegge, I. Chorkendorff, I. E. L. Stephens, and Y. Shao-Horn, "Towards identifying the active sites on RuO 2 (110) in catalyzing oxygen evolution", *Energy & Environmental Science* **10** no. 12, (2017) 2626–2637.

(22) R. R. Rao, M. J. Kolb, J. Hwang, A. F. Pedersen, A. Mehta, H. You, K. A. Stoerzinger, Z. Feng, H. Zhou, H. Bluhm, L. Giordano, I. E. L. Stephens, and Y. Shao-Horn, "Surface Orientation Dependent Water Dissociation on Rutile Ruthenium Dioxide", *The Journal of Physical Chemistry C* **122** no. 31, (2018) 17802–17811.

(23) R. R. Rao, M. J. Kolb, L. Giordano, A. F. Pedersen, Y. Katayama, J. Hwang, A. Mehta, H. You, J. R. Lunger, H. Zhou, N. B. Halck, T. Vegge, I. Chorkendorff, I. E. L. Stephens, and Y. Shao-Horn, "Operando identification of site-dependent water oxidation activity on ruthenium dioxide single-crystal surfaces", *Nature Catalysis* **3** no. 6, (2020) 516–525.

(24) K. A. Stoerzinger, L. Qiao, M. D. Biegalski, and Y. Shao-Horn, "Orientation-Dependent Oxygen Evolution Activities of Rutile IrO2 and RuO2", *The journal of physical chemistry letters* **5** no. 10, (2014) 1636–1641.

(25) K. A. Stoerzinger, O. Diaz-Morales, M. Kolb, R. R. Rao, R. Frydendal, L. Qiao, X. R. Wang, N. B. Halck, J. Rossmeisl, H. A. Hansen, T. Vegge, I. E. L. Stephens, M. T. M. Koper, and Y. Shao-Horn, "Orientation-Dependent Oxygen Evolution on RuO 2 without Lattice Exchange", *ACS Energy Letters* **2** no. 4, (2017) 876–881.

(26) K. A. Stoerzinger, R. R. Rao, X. R. Wang, W. T. Hong, C. M. Rouleau, and Y. Shao-Horn, "The Role of Ru Redox in pH-Dependent Oxygen Evolution on Rutile Ruthenium Dioxide Surfaces", *Chem* **2** no. 5, (2017) 668–675.

(27) P. Kessler, *Master's thesis: Pulsed laser deposition and spectroscopic characterization of epitaxial RuO2 films*. 2021.

(28) K.-H. Ahn, A. Hariki, K.-W. Lee, and J. Kuneš, "Antiferromagnetism in RuO2 as d -wave Pomeranchuk instability", *Physical Review B* **99** no. 18, (2019) .

(29) Z. H. Zhu, J. Strempfer, R. R. Rao, C. A. Occhialini, J. Pelliciari, Y. Choi, T. Kawaguchi, H. You, J. F. Mitchell, Y. Shao-Horn, and R. Comin, "Anomalous Antiferromagnetism in Metallic RuO_2 Determined by Resonant X-ray Scattering", *Physical review letters* **122** no. 1, (2019) 017202.

(30) T. Berlijn, P. C. Snijders, O. Delaire, H.-D. Zhou, T. A. Maier, H.-B. Cao, S.-X. Chi, M. Matsuda, Y. Wang, M. R. Koehler, P. R. C. Kent, and H. H. Weitering, "Itinerant Antiferromagnetism in RuO_2", *Physical review letters* **118** no. 7, (2017) 077201.

(31) E. Torun, C. M. Fang, G. A. de Wijs, and R. A. de Groot, "Role of Magnetism in Catalysis: RuO 2 (110) Surface", *The Journal of Physical Chemistry C* **117** no. 12, (2013) 6353–6357.

(32) J. Rossmeisl, Z.-W. Qu, H. Zhu, G.-J. Kroes, and J. K. Nørskov, "Electrolysis of water on oxide surfaces", *Journal of Electroanalytical Chemistry* **607** no. 1-2, (2007) 83–89.

(33) A. J. Bard and L. R. Faulkner, *Electrochemical methods: Fundamentals and applications*. Wiley, New York and Weinheim, 2. edition ed., 2001.

(34) K. S. Exner, I. Sohrabnejad-Eskan, and H. Over, "A Universal Approach To Determine the Free Energy Diagram of an Electrocatalytic Reaction", *ACS Catalysis* **8** no. 3, (2018) 1864–1879.

(35) R. G. Compton and C. E. Banks, *Understanding voltammetry*. World Scientific, New Jersey and London and Singapore and Beijing and Shanghai and Hong Kong and Taipei and Chennai and Tokyo, third edition ed., 2018.

(36) J. Goodisman, "Observations on Lemon Cells", *Journal of Chemical Education* **78** no. 4, (2001) 516.

(37) K. Schmidt-Rohr, "How Batteries Store and Release Energy: Explaining Basic Electrochemistry", *Journal of Chemical Education* **95** no. 10, (2018) 1801–1810.

(38) Y. Sugawara, T. Okayasu, A. P. Yadav, A. Nishikata, and T. Tsuru, "Dissolution Mechanism of Platinum in Sulfuric Acid Solution", *Journal of The Electrochemical Society* **159** no. 11, (2012) F779–F786.

(39) P. Wongbua-ngam, W. Veerasai, P. Wilairat, and O.-U. Kheowan, "Model interpretation of electrochemical behavior of Pt/H2SO4 interface over both the hydrogen oxidation and oxide formation regions", *International Journal of Hydrogen Energy* **44** no. 23, (2019) 12108–12117.

(40) N. Danilovic, R. Subbaraman, K.-C. Chang, S. H. Chang, Y. J. Kang, J. Snyder, A. P. Paulikas, D. Strmcnik, Y.-T. Kim, D. Myers, V. R. Stamenkovic, and N. M. Markovic, "Activity-Stability Trends for the Oxygen Evolution Reaction on Monometallic Oxides in Acidic Environments", *The journal of physical chemistry letters* **5** no. 14, (2014) 2474–2478.

(41) A. E. Bolzán and A. J. Arvia, "Changes in the kinetics of the oxygen evolution reaction induced by oxide films at platinum electrodes", *Journal of Electroanalytical Chemistry* **375** no. 1-2, (1994) 157–162.

(42) A. Damjanovic, V. I. Birss, and D. S. Boudreaux, "Electron Transfer Through Thin Anodic Oxide Films during the Oxygen Evolution Reactions at Pt Electrodes: I . Acid Solutions", *Journal of The Electrochemical Society* **138** no. 9, (1991) 2549–2555.

(43) D. Gilroy and B. E. Conway, "Surface oxidation and reduction of platinum electrodes: Coverage, kinetic and hysteresis studies", *Canadian Journal of Chemistry* **46** no. 6, (1968) 875–890.

(44) M. Duca and M. T. Koper, "Fundamental Aspects of Electrocatalysis 1)", in *Surface and Interface Science*, K. Wandelt, ed., pp. 773–890. Wiley, 2020.

(45) V. Climent and J. M. Feliu, "Thirty years of platinum single crystal electrochemistry", *Journal of Solid State Electrochemistry* **15** no. 7-8, (2011) 1297–1315.

(46) D. Chen, Q. Tao, L. W. Liao, S. X. Liu, Y. X. Chen, and S. Ye, "Determining the Active Surface Area for Various Platinum Electrodes", *Electrocatalysis* **2** no. 3, (2011) 207–219.

(47) I. Sohrabnejad-Eskan, A. Goryachev, K. S. Exner, L. A. Kibler, E. J. M. Hensen, J. P. Hofmann, and H. Over, "Temperature-Dependent Kinetic Studies of the Chlorine Evolution Reaction over RuO 2 (110) Model Electrodes", *ACS Catalysis* **7** no. 4, (2017) 2403–2411.

(48) T. Lister, Y. Chu, W. Cullen, H. You, R. Yonco, J. Mitchell, and Z. Nagy, "Electrochemical and X-ray scattering study of well defined RuO2 single crystal surfaces", *Journal of Electroanalytical Chemistry* **524-525** (2002) 201–218.

(49) D.-Y. Kuo, H. Paik, J. Kloppenburg, B. Faeth, K. M. Shen, D. G. Schlom, G. Hautier, and J. Suntivich, "Measurements of Oxygen Electroadsorption Energies and Oxygen Evolution Reaction on RuO2(110): A Discussion of the Sabatier Principle and Its Role in Electrocatalysis", *Journal of the American Chemical Society* **140** no. 50, (2018) 17597–17605.

(50) R. R. Rao, B. Huang, Y. Katayama, J. Hwang, T. Kawaguchi, J. R. Lunger, J. Peng, Y. Zhang, A. Morinaga, H. Zhou, H. You, and Y. Shao-Horn, "pH- and Cation-Dependent Water Oxidation on Rutile RuO 2 (110)", *The Journal of Physical Chemistry C* **125** no. 15, (2021) 8195–8207.

(51) D.-Y. Kuo, H. Paik, J. N. Nelson, K. M. Shen, D. G. Schlom, and J. Suntivich, "Chlorine evolution reaction electrocatalysis on RuO2(110) and IrO2(110) grown using molecular-beam epitaxy", *The Journal of chemical physics* **150** no. 4, (2019) 041726.

(52) T. Hepel, F. H. Pollak, and W. E. O'Grady, "Effect of Crystallographic Orientation of Single–Crystal RuO2 Electrodes on the Hydrogen Adsorption Reactions", *Journal of The Electrochemical Society* **131** no. 9, (1984) 2094–2100.

(53) T. P. Silverstein, "The Aqueous Proton Is Hydrated by More Than One Water Molecule: Is the Hydronium Ion a Useful Conceit?", *Journal of Chemical Education* **91** no. 4, (2014) 608–610.

(54) aquion, "aquion online pH-calculator", 2022, retrieved: 01.03.2022. `http://www.aqion.onl/`.

(55) S. S. Zumdahl and S. A. Zumdahl, *Chemistry*. Brooks/Cole Cengage Learning, Belmont, CA, ninth edition ed., 2014.

(56) G. Jerkiewicz, "Standard and Reversible Hydrogen Electrodes: Theory, Design, Operation, and Applications", *ACS Catalysis* **10** no. 15, (2020) 8409–8417.

(57) E. Rebhan, *Thermodynamik und Statistik*. Theoretische Physik / Eckhard Rebhan. Spektrum Akademischer Verlag, Heidelberg, 2010.

(58) D. T. Sawyer, A. Sobkowiak, and J. L. Roberts, *Electrochemistry for chemists*. Wiley, New York, 2. ed. ed., 1995.

(59) G. Inzelt, ed., *Handbook of Reference Electrodes*. Springer, Berlin and Heidelberg, 2013.

(60) W. Oelßner, F. Berthold, and U. Guth, "The iR drop - well-known but often underestimated in electrochemical polarization measurements and corrosion testing", *Materials and Corrosion* **57** no. 6, (2006) 455–466.

(61) N. Eliaz and E. Gileadi, *Physical electrochemistry: Fundamentals, techniques, and applications*. Wiley-VCH, Weinheim, second edition ed., 2019.

(62) A. J. Bard, "Inner-sphere heterogeneous electrode reactions. Electrocatalysis and photocatalysis: the challenge", *Journal of the American Chemical Society* **132** no. 22, (2010) 7559–7567.

(63) P. Kurzweil, *Angewandte Elektrochemie*. Springer Fachmedien Wiesbaden, Wiesbaden, 2020.

(64) A. A. Karyakin, E. E. Karyakina, and Lo Gorton, "The electrocatalytic activity of Prussian blue in hydrogen peroxide reduction studied using a wall-jet electrode with continuous flow", *Journal of Electroanalytical Chemistry* **456** no. 1-2, (1998) 97–104.

(65) F. G. Cottrell, "Der Reststrom bei galvanischer Polarisation, betrachtet als ein Diffusionsproblem", *Zeitschrift für Physikalische Chemie* **42U** no. 1, (1903) 385–431.

(66) E. Laviron, "General expression of the linear potential sweep voltammogram in the case of diffusionless electrochemical systems", *Journal of Electroanalytical Chemistry and Interfacial Electrochemistry* **101** no. 1, (1979) 19–28.

(67) E. Laviron, "Surface linear potential sweep voltammetry", *Journal of Electroanalytical Chemistry and Interfacial Electrochemistry* **52** no. 3, (1974) 395–402.

(68) E. Laviron, "The use of linear potential sweep voltammetry and of a.c. voltammetry for the study of the surface electrochemical reaction of strongly adsorbed systems and of redox modified electrodes", *Journal of Electroanalytical Chemistry and Interfacial Electrochemistry* **100** no. 1-2, (1979) 263–270.

(69) M. J. Honeychurch and G. A. Rechnitz, "Voltammetry of Adsorbed Molecules. Part 1: Reversible Redox Systems", *Electroanalysis* **10** no. 5, (1998) 285–293.

(70) M. Favaro, "Stochastic Analysis of Electron Transfer and Mass Transport in Confined Solid/Liquid Interfaces", *Surfaces* **3** no. 3, (2020) 392–407.

(71) M. Noel, S. Chandrasekaran, and C. Basha, "Linear sweep voltammetric approach for the study of monolayer formation", *Journal of Electroanalytical Chemistry and Interfacial Electrochemistry* **225** no. 1-2, (1987) 93–109.

(72) M. J. Honeychurch and G. A. Rechnitz, "Voltammetry of Adsorbed Molecules. Part 2: Irreversible Redox Systems", *Electroanalysis* **10** no. 7, (1998) 453–457.

(73) M. Yang and R. G. Compton, "Voltammetry of Adsorbed Species: Nonideal Interactions Leading to Phase Transitions", *The Journal of Physical Chemistry C* **124** no. 33, (2020) 18031–18044.

(74) E. Barsoukov and J. R. Macdonald, *Impedance spectroscopy: Theory, experiment, and applications*. Wiley-Interscience, Hoboken N.J., 2nd ed. ed., 2005.

(75) J. C. Myland and K. B. Oldham, "Uncompensated resistance. 1. The effect of cell geometry", *Analytical Chemistry* **72** no. 17, (2000) 3972–3980.

(76) S. E. Temmel, S. A. Tschupp, and T. J. Schmidt, "A highly flexible electrochemical flow cell designed for the use of model electrode materials on non-conventional substrates", *The Review of scientific instruments* **87** no. 4, (2016) 045115.

(77) S. Geiger, S. Cherevko, and K. J. Mayrhofer, "Dissolution of Platinum in Presence of Chloride Traces", *Electrochimica Acta* **179** (2015) 24–31.

(78) D. Grujicic and B. Pesic, "Electrodeposition of copper: the nucleation mechanisms", *Electrochimica Acta* **47** no. 18, (2002) 2901–2912.

(79) D. Grujicic and B. Pesic, "Reaction and nucleation mechanisms of copper electrodeposition from ammoniacal solutions on vitreous carbon", *Electrochimica Acta* **50** no. 22, (2005) 4426–4443.

(80) S. Machado, A. A. Tanaka, and E. R. Gonzalez, "Underpotential deposition of copper and its influence in the oxygen reduction on platinum", *Electrochimica Acta* **36** no. 8, (1991) 1325–1331.

(81) A. A. Gewirth and M. S. Thorum, "Electroreduction of dioxygen for fuel-cell applications: materials and challenges", *Inorganic chemistry* **49** no. 8, (2010) 3557–3566.

(82) E. Yeager, "Electrocatalysts for O2 reduction", *Electrochimica Acta* **29** no. 11, (1984) 1527–1537.

(83) C.-H. Chen, K. E. Meadows, A. Cuharuc, S. C. S. Lai, and P. R. Unwin, "High resolution mapping of oxygen reduction reaction kinetics at polycrystalline platinum electrodes", *Physical chemistry chemical physics : PCCP* **16** no. 34, (2014) 18545–18552.

(84) P. Zimmermann, A. Weltin, G. A. Urban, and J. Kieninger, "Active Potentiometry for Dissolved Oxygen Monitoring with Platinum Electrodes", *Sensors (Basel, Switzerland)* **18** no. 8, (2018) .

(85) M. W. Breiter, "Voltammetric study of halide ion adsorption on platinum in perchloric acid solutions", *Electrochimica Acta* **8** no. 12, (1963) 925–935.

(86) P. Daubinger, J. Kieninger, T. Unmüssig, and G. A. Urban, "Electrochemical characteristics of nanostructured platinum electrodes–a cyclic voltammetry study", *Physical chemistry chemical physics : PCCP* **16** no. 18, (2014) 8392–8399.

(87) D. M. Novak and B. E. Conway, "Competitive adsorption and state of charge of halide ions in monolayer oxide film growth processes at Pt anodes", *Journal of the Chemical Society, Faraday Transactions 1: Physical Chemistry in Condensed Phases* **77** no. 10, (1981) 2341.

(88) B. E. Conway and D. M. Novak, "Chloride ion adsorption effects in the recombination-controlled kinetics of anodic chlorine evolution at Pt electrodes", *Journal of the Chemical Society, Faraday Transactions 1: Physical Chemistry in Condensed Phases* **75** no. 0, (1979) 2454.

(89) V. Sumaria, D. Krishnamurthy, and V. Viswanathan, "Quantifying Confidence in DFT Predicted Surface Pourbaix Diagrams and Associated Reaction Pathways for Chlorine Evolution", *ACS Catalysis* **8** no. 10, (2018) 9034–9042.

(90) K. S. Exner, J. Anton, T. Jacob, and H. Over, "Chlorine Evolution Reaction on RuO2(110): Ab initio Atomistic Thermodynamics Study - Pourbaix Diagrams", *Electrochimica Acta* **120** (2014) 460–466.

(91) Q. Liang, A. Bieberle-Hütter, and G. Brocks, "Anti-Ferromagnetic RuO 2 : A Stable and Robust OER Catalyst over a Large Range of Surface Terminations", *The Journal of Physical Chemistry C* **126** no. 3, (2022) 1337–1345.

(92) J. G. Vos and M. Koper, "Measurement of competition between oxygen evolution and chlorine evolution using rotating ring-disk electrode voltammetry", *Journal of Electroanalytical Chemistry* **819** (2018) 260–268.

(93) K. Y. Leung and C. C. L. McCrory, "Effect and Prevention of Trace Ag + Contamination from Ag/AgCl Reference Electrodes on CO 2 Reduction Product Distributions at Polycrystalline Copper Electrodes", *ACS Applied Energy Materials* **2** no. 11, (2019) 8283–8293.

(94) T. Hepel, F. H. Pollak, and W. E. O'Grady, "Electrochemistry of sub-monolayer silver deposits on single crystal RuO2 (110), (001) and (111) electrodes", *Journal of Electroanalytical Chemistry and Interfacial Electrochemistry* **236** no. 1-2, (1987) 295–304.

(95) T. Hepel, F. H. Pollak, and W. E. O'Grady, "Pulse–Stimulated Potentiostatic Deposition of Silver on Single Crystal RuO2 (110) Surface", *Journal of The Electrochemical Society* **135** no. 3, (1988) 562–567.

(96) P. Charoen-amornkitt, T. Suzuki, and S. Tsushima, "Effects of Voltage-Dependence of the Constant Phase Element and Ohmic Parameters in the Modeling and Simulation of Cyclic Voltammograms", *Journal of The Electrochemical Society* **167** no. 16, (2020) 166506.

(97) O. Gharbi, M. T. Tran, B. Tribollet, M. Turmine, and V. Vivier, "Revisiting cyclic voltammetry and electrochemical impedance spectroscopy analysis for capacitance measurements", *Electrochimica Acta* **343** (2020) 136109.

(98) S. Trasatti and O. A. Petrii, "Real surface area measurements in electrochemistry", *Pure and Applied Chemistry* **63** no. 5, (1991) 711–734.

(99) C. Wei, S. Sun, D. Mandler, X. Wang, S. Z. Qiao, and Z. J. Xu, "Approaches for measuring the surface areas of metal oxide electrocatalysts for determining their intrinsic electrocatalytic activity", *Chemical Society reviews* **48** no. 9, (2019) 2518–2534.

(100) D. M. Morales and M. Risch, *Seven Steps to Reliable Cyclic Voltammetry Measurements for the Determination of Double Layer Capacitance*. 2021.

(101) A. Goryachev, M. Etzi Coller Pascuzzi, F. Carlà, T. Weber, H. Over, E. J. Hensen, and J. P. Hofmann, "Electrochemical stability of RuO2(110)/Ru(0001) model electrodes in the oxygen and chlorine evolution reactions", *Electrochimica Acta* **336** (2020) 135713.

(102) D. W. Kang, M. Jun, J. Kim, H. Yang, T. Kwon, J. Joo, H. Kim, M. Kang, J. Y. Kim, K. Lee, and C. S. Hong, "Double Hypercrosslinked Porous Organic Polymer-Derived Electrocatalysts for a Water Splitting Device", *ACS Applied Energy Materials* **5** no. 3, (2022) 3269–3274.

(103) C. C. L. McCrory, S. Jung, J. C. Peters, and T. F. Jaramillo, "Benchmarking heterogeneous electrocatalysts for the oxygen evolution reaction", *Journal of the American Chemical Society* **135** no. 45, (2013) 16977–16987.

(104) M. Tomkiewicz, Y. S. Huang, and F. H. Pollak, "The Potential of Zero Charge of Oriented Single–Crystal RuO2 in Aqueous Electrolytes", *Journal of The Electrochemical Society* **130** no. 7, (1983) 1514–1518.

(105) W. Sugimoto, T. Kizaki, K. Yokoshima, Y. Murakami, and Y. Takasu, "Evaluation of the pseudocapacitance in RuO2 with a RuO2/GC thin film electrode", *Electrochimica Acta* **49** no. 2, (2004) 313–320.

(106) G.-h. Jeong and H.-L. Park, "Behavior of RuO2 (100), (110) and (101) Single-Crystal Faces in H2SO4", *Bulletin of the Korean Chemical Society* **3** no. 3, (1982) 89–92.

(107) E. Guerrini, V. Consonni, and S. Trasatti, "Surface and electrocatalytic properties of well-defined and vicinal RuO2 single crystal faces", *Journal of Solid State Electrochemistry* **9** no. 5, (2005) 320–329.

(108) Y. S. Huang and P. C. Liao, "Preparation and characterization of RuO2 thin films", *Solar Energy Materials and Solar Cells* **55** no. 1-2, (1998) 179–197.

(109) I. Sohrabnejad-Eskan, *PhD thesis: Kinetische Untersuchungen der Chlorgasentwicklung über eine einkristalline RuO2(110)-Modellelektrode*. 2017.

(110) F. Creazzo and S. Luber, "Explicit solvent effects on (1 1 0) ruthenium oxide surface wettability: Structural, electronic and mechanical properties of rutile RuO2 by means of spin-polarized DFT-MD", *Applied Surface Science* **570** (2021) 150993.

(111) H. A. Hansen, I. C. Man, F. Studt, F. Abild-Pedersen, T. Bligaard, and J. Rossmeisl, "Electrochemical chlorine evolution at rutile oxide (110) surfaces", *Physical chemistry chemical physics : PCCP* **12** no. 1, (2010) 283–290.

(112) Y.-H. Fang and Z.-P. Liu, "Mechanism and Tafel lines of electro-oxidation of water to oxygen on RuO2(110)", *Journal of the American Chemical Society* **132** no. 51, (2010) 18214–18222.

(113) Y. Ping, R. J. Nielsen, and W. A. Goddard, "The Reaction Mechanism with Free Energy Barriers at Constant Potentials for the Oxygen Evolution Reaction at the IrO(2) (110) Surface", *Journal of the American Chemical Society* **139** no. 1, (2017) 149–155.

(114) H. N. Nong, L. J. Falling, A. Bergmann, M. Klingenhof, H. P. Tran, C. Spöri, R. Mom, J. Timoshenko, G. Zichittella, A. Knop-Gericke, S. Piccinin,

J. Pérez-Ramírez, B. R. Cuenya, R. Schlögl, P. Strasser, D. Teschner, and T. E. Jones, "Key role of chemistry versus bias in electrocatalytic oxygen evolution", *Nature* **587** no. 7834, (2020) 408–413.

(115) F. Creazzo and S. Luber, "Water-Assisted Chemical Route Towards the Oxygen Evolution Reaction at the Hydrated (110) Ruthenium Oxide Surface: Heterogeneous Catalysis via DFT-MD and Metadynamics Simulations", *Chemistry (Weinheim an der Bergstrasse, Germany)* **27** no. 68, (2021) 17024–17037.

(116) B. Hu, D.-Y. Kuo, H. Paik, D. G. Schlom, and J. Suntivich, "Enthalpy and entropy of oxygen electroadsorption on RuO2(110) in alkaline media", *The Journal of chemical physics* **152** no. 9, (2020) 094704.

(117) C. F. Dickens and J. K. Nørskov, "A Theoretical Investigation into the Role of Surface Defects for Oxygen Evolution on RuO 2", *The Journal of Physical Chemistry C* **121** no. 34, (2017) 18516–18524.

(118) E. Fabbri, A. Habereder, K. Waltar, R. Kötz, and T. J. Schmidt, "Developments and perspectives of oxide-based catalysts for the oxygen evolution reaction", *Catal. Sci. Technol.* **4** no. 11, (2014) 3800–3821.

(119) C. Wei, R. R. Rao, J. Peng, B. Huang, I. E. L. Stephens, M. Risch, Z. J. Xu, and Y. Shao-Horn, "Recommended Practices and Benchmark Activity for Hydrogen and Oxygen Electrocatalysis in Water Splitting and Fuel Cells", *Advanced materials (Deerfield Beach, Fla.)* **31** no. 31, (2019) e1806296.

(120) C. O. Soares, O. Rodríguez, G. Buvat, M. Duca, S. Garbarino, D. Guay, G. Denuault, and A. C. Tavares, "Sampled current voltammetry for kinetic studies on materials unsuitable for rotating discs or microelectrodes: Application to the oxygen reduction reaction in acidic medium", *Electrochimica Acta* **362** (2020) 136946.

(121) G. K. H. Wiberg and M. Arenz, "On the influence of hydronium and hydroxide ion diffusion on the hydrogen and oxygen evolution reactions in aqueous media", *Electrochimica Acta* **158** (2015) 13–17.

(122) A. C. Garcia and M. T. M. Koper, "Effect of Saturating the Electrolyte with Oxygen on the Activity for the Oxygen Evolution Reaction", *ACS Catalysis* **8** no. 10, (2018) 9359–9363.

(123) R. Tang-Kong, C. E. D. Chidsey, and P. C. McIntyre, "Reversible Decay of Oxygen Evolution Activity of Iridium Catalysts", *Journal of The Electrochemical Society* **166** no. 14, (2019) H712–H717.

(124) O. L. Hendricks, R. Tang-Kong, A. S. Babadi, P. C. McIntyre, and C. E. D. Chidsey, "Atomic Layer Deposited TiO 2 –IrO x Alloys Enable Corrosion Resistant Water Oxidation on Silicon at High Photovoltage", *Chemistry of Materials* **31** no. 1, (2019) 90–100.

(125) X. Tan, J. Shen, N. Semagina, and M. Secanell, "Decoupling structure-sensitive deactivation mechanisms of Ir/IrOx electrocatalysts toward oxygen evolution reaction", *Journal of Catalysis* **371** (2019) 57–70.

(126) A. Hartig-Weiss, M. F. Tovini, H. A. Gasteiger, and H. A. El-Sayed, "OER Catalyst Durability Tests Using the Rotating Disk Electrode Technique: The Reason Why This Leads to Erroneous Conclusions", *ACS Applied Energy Materials* **3** no. 11, (2020) 10323–10327.

(127) K. Klyukin, A. Zagalskaya, and V. Alexandrov, "Role of Dissolution Intermediates in Promoting Oxygen Evolution Reaction at RuO 2 (110) Surface", *The Journal of Physical Chemistry C* **123** no. 36, (2019) 22151–22157.

(128) T. Weber, J. Pfrommer, M. J. Abb, B. Herd, O. Khalid, M. Rohnke, P. H. Lakner, J. Evertsson, S. Volkov, F. Bertram, R. Znaiguia, F. Carla, V. Vonk, E. Lundgren, A. Stierle, and H. Over, "Potential-Induced Pitting Corrosion of an IrO 2 (110)-RuO 2 (110)/Ru(0001) Model Electrode under Oxygen Evolution Reaction Conditions", *ACS Catalysis* **9** no. 7, (2019) 6530–6539.

(129) T. Weber, T. Ortmann, D. Escalera-López, M. J. S. Abb, B. Mogwitz, S. Cherevko, M. Rohnke, and H. Over, "Visualizing Potential–Induced Pitting Corrosion of Ultrathin Single–Crystalline IrO 2 (110) Films on RuO 2 (110)/Ru(0001) under Electrochemical Water Splitting Conditions", *ChemCatChem* **12** no. 3, (2020) 855–866.

(130) R. Kötz, S. Stucki, D. Scherson, and D. M. Kolb, "In-situ identification of RuO4 as the corrosion product during oxygen evolution on ruthenium in acid media", *Journal of Electroanalytical Chemistry and Interfacial Electrochemistry* **172** no. 1-2, (1984) 211–219.

(131) M. Vuković, "Rotating ring–disc electrode study of the enhanced oxygen evolution on an activated ruthenium electrode", *J. Chem. Soc., Faraday Trans.* **86** no. 22, (1990) 3743–3746.

(132) J. Juodkazytė, R. Vilkauskaitė, B. Šebeka, and K. Juodkazis, "Difference between surface electrochemistry of ruthenium and RuO 2 electrodes", *Transactions of the IMF* **85** no. 4, (2007) 194–201.

(133) Z. Wang, X. Guo, J. Montoya, and J. K. Nørskov, "Predicting aqueous stability of solid with computed Pourbaix diagram using SCAN functional", *npj Computational Materials* **6** no. 1, (2020) .

(134) P. Castelli, S. Trasatti, F. H. Pollak, and W. E. O'Grady, "Single crystals as model electrocatalysts", *Journal of Electroanalytical Chemistry and Interfacial Electrochemistry* **210** no. 1, (1986) 189–194.

Acknowledgements

Zuallererst möchte ich mich bei Prof. Dr. Ralph Claessen bedanken, für die Möglichkeit meine Arbeit an seinem Lehrstuhl durchführen zu können. Bei Prof. Dr. Matthias Bode für die Erstellung des Zweitgutachtens. Bei Dr. Simon Moser, der bei diesem besonderen Projekt sein Vertrauen in mich gesetzt hat und mir stehts mit Rat und Tat zur Seite stand. Bei Dr. Vedran Jovic, für den selbst zu späterer Stunde im zeitverschobenen Neuseeland nie eine Diskussion zu langwierig wurde. Bei Jürgen Ochmann und Rainer Brauer aus der universitären Werkstatt, die in gewohnter Präzision die entworfenen elektrochemischen Messzellen anfertigten. Und bei den restlichen Mitgliedern des Lehrstuhls für Experimentelle Physik IV, für die freundliche und kollegiale Atmosphäre bei der die Arbeit immer eine Freude war – vielen Dank für die schöne Zeit.

Julius-Maximilians-
UNIVERSITÄT
WÜRZBURG

Versicherung zur Leistungserbringung

Titel der Abschlussarbeit:

Development of an electrochemical testing setup to characterize $RuO_2(110)$ thin films

Thema bereitgestellt von (Titel, Vorname, Nachname, Lehrstuhl):

Dr. Simon Moser, Lehrstuhl für Experimentelle Physik IV

Eingereicht durch (Vorname, Nachname, Matrikel):

Christopher Reiser, 2181425

Ich versichere, dass ich die vorstehende Arbeit selbstständig und ohne fremde Hilfe angefertigt und mich keiner anderer als der in den beigefügten Verzeichnissen angegebenen Hilfsmittel bedient habe. Alle Textstellen, die wörtlich oder sinngemäß aus Veröffentlichungen Dritter entnommen wurden, sind als solche kenntlich gemacht. Alle Quellen, die dem World Wide Web entnommen oder in einer digitalen Form verwendet wurden, sind der Arbeit beigefügt.

Weitere Personen waren an der geistigen Leistung der vorliegenden Arbeit nicht beteiligt. Insbesondere habe ich nicht die Hilfe eines Ghostwriters oder einer Ghostwriting-Agentur in Anspruch genommen. Dritte haben von mir weder unmittelbar noch mittelbar Geld oder geldwerte Leistungen für Arbeiten erhalten, die im Zusammenhang mit dem Inhalt der vorgelegten Arbeit stehen.

Der Durchführung einer elektronischen Plagiatsprüfung stimme ich hiermit zu. Die eingereichte elektronische Fassung der Arbeit ist vollständig. Mir ist bewusst, dass nachträgliche Ergänzungen ausgeschlossen sind.

Die Arbeit wurde bisher keiner anderen Prüfungsbehörde vorgelegt und auch nicht veröffentlicht. Ich bin mir bewusst, dass eine unwahre Erklärung zur Versicherung der selbstständigen Leistungserbringung rechtliche Folgen haben kann.

Ort, Datum, Unterschrift